Lifetimes of States in ^{19}Ne Above the ^{15}O + alpha Threshold.

by

Mythili Myths Subramanian

B.Sc., The University of Madras, India,1981
M.Sc., The Indian Institute of Technology, Mumbai, India,1983

A THESIS SUBMITTED IN PARTIAL FULFILMENT OF
THE REQUIREMENTS FOR THE DEGREE OF

Doctor of Philosophy

in

The Faculty of Graduate Studies

(Physics)

The University Of British Columbia

(Vancouver)

April 2008

Abstract

Astrophysical models that address stellar energy generation and nucleosynthesis require a considerable amount of input from nuclear physics and are very sensitive to the detailed structure of nuclei, both stable and unstable. Radioactive nuclei play a dominant role in several stellar environments such as supernovae, X-ray bursts, novae etc. and nuclear data are important in the interpretation of these phenomena.

When carbon, nitrogen and oxygen isotopes are present in substantial quantities in a star of sufficient mass, the fusion of four hydrogen nuclei to form a helium nucleus proceeds via the CNO cycle. Energy release in the CNO cycles is limited by the long lifetimes of ^{14}O and ^{15}O. In neutron stars and white dwarfs where the CNO cycles are operational, the energy release increases dramatically when the CNO cycles are broken. In explosive stellar scenarios such as novae and X-ray bursts, the energy output is very large, suggesting a breakout from the CNO cycle. $^{15}\mathrm{O}(\alpha,\gamma)^{19}\mathrm{Ne}$ is the first reaction that breaks out of the CNO cycle and occurs when ^{15}O resonantly captures an α particle. States in ^{19}Ne above the $^{15}\mathrm{O} + \alpha$ threshold of 3.53 MeV could be populated and provide the path way for the CNO breakout. Nuclear structure information of these high lying states in ^{19}Ne is required to calculate the rate of the $^{15}\mathrm{O}(\alpha,\gamma)^{19}\mathrm{Ne}$ reaction; however, this information is incomplete. This work focusses on the study of states in ^{19}Ne above 3.53 MeV.

The lifetimes of five states in ^{19}Ne above 3.53 MeV were measured in this work. The states in ^{19}Ne were populated via the $^{3}\mathrm{He}(^{20}\mathrm{Ne},\alpha)^{19}\mathrm{Ne}$ reaction at a beam energy of 34 MeV. The lifetimes were measured using the Doppler Shift Attenuation Method (DSAM). The lifetimes of five states were measured and an upper limit was set on the lifetime of a sixth state. Three of the measurements are the most precise thus far. The lifetimes of the other three states agree with the values of the only other measurement of the lifetimes of these states. An upper limit on the rate of the $^{15}\mathrm{O}(\alpha,\gamma)^{19}\mathrm{Ne}$ reaction was calculated at the 90% confidence level using the measured lifetimes. The contributions to the $^{15}\mathrm{O}(\alpha,\gamma)^{19}\mathrm{Ne}$ reaction rate from several states in ^{19}Ne at different stellar temperatures are then discussed.

Table of Contents

Appendices

List of Tables

List of Figures

Acknowledgements

I am very grateful to my supervisor Dr. Barry Davids for his untiring efforts in guiding me through this work. His vast knowledge, unflagging patience, careful approach to any problem, incisive questioning, constant encouragement and meticulous attention to details cajoled me through the thesis work. Besides guiding me through the scientific aspects, his extraordinary editing has improved this manuscript tremendously.

Dr. Paul Hickson, my co-supervisor has helped me out in several ways - guiding me through the academics well as the bureaucracy. I will gratefully remember the ease with which he accommodated my several requests. Dr. Stan Yen gave me a great deal of support when I was new at UBC. His classes in nuclear physics were delightful and he taught me to believe that I could complete the dissertation faster than I thought I was capable of.

I thank Dr. Harvey Richer for teaching me Astrophysics in his amazing style. His suggestions to improve the thesis and his questioning helped me improve the thesis greatly. Dr. Scott Oser taught me concepts on elementary particles and Feynman diagrams and encouraged me to work out a section in this thesis that has direct bearing on the motivation. Finally I must thank Dr. John Ng for coaxing me to think in different dimensions and laid out an approach that was intuitive and intellectually satisfying.

I thank Dr. Cornelius Beausang, Dr. Donald Fleming and Dr. Janis McKenna for reading my thesis and offering excellent suggestions to improve the manuscript.

The expertise of Dr. Gordon Ball during the set up of the experiment and during the analysis period was invaluable. The setting up for the experiment would have been impossible without Mr. Randy Churchman's dexterity and resourcefulness. Dr. Greg Hackman's cheerful demeanor and readiness to help raised my spirits even when things were running behind schedule. Dr. Tom Alexander and Dr. Jim Forster educated me in the various subtleties involved in the measurements and analysis. I approached Dr. Elizabeth Padilla-Rodel, Dr. Matt Pearson and Dr. Gotz Ruprecht several times to resolve stubborn issues and they were always supportive. Thanks for all the help.

I would like to thank Dr. Dave Axen for his enthusiasm and the time he spent teaching me the nuances of GEANT4. I thank the TRIUMF cyclotron staff for the excellent beam and support they offered during the experiment.

My friends in three countries had a lot of faith in me - a lot more than I thought they had reason to. I was ready to buckle under the intense pressure of graduate work on several occasions but they kept my spirits up. Thanks to Kavita Dixit and Zafar Ahmed in India, to Swathi Narayanan and Sabiha Khalfay in Kuwait, to Hassan Saadouni, Sushma Koleswar and Peter Russo in Canada.

I do not have the eloquence to thank the five people who are extremely important to me - my father Ramakrishnan, my mother Ananthalakshmi, my daughter Archana, my son Bala and my husband Mani. Their quiet confidence and unshakeable faith in my capabilities urged me to continue forward on my chosen path. I did not travel to meet my parents during the years at graduate school - they travelled half way across the world to visit me. My children and my husband supported me wordlessly through the long, hard years of research and course work - I believe this support is the primary reason I could complete this thesis. They undoubtedly sacrificed a great deal more than they had imagined while I was working on my Ph.D. Help with school work, play rehearsals, concert recitals, business commitments, family get togethers - everything took a back seat while the thesis work was in the driving seat. My family accepted all my eccentricities and priorities without a murmur of protest. I am deeply humbled by the constant encouragement, extraordinary understanding and unconditional love I receive from these amazing people.

To Mani, Archana and Bala

Chapter 1

Introduction

Nuclear physics provides important input parameters for astrophysical models. It is concerned with the evolution of elements in the Universe and examines the evidence for their current distribution. Explosive phenomena such as supernovae are investigated in order to understand and explain the energy release in stars. The study of energy generation, synthesis of the elements and their nuclear properties yields important data for astrophysical calculations.

Astronomy is essentially an observational science and the parameters affecting the astronomical observables cannot be varied. However, some of the processes that affect astronomical observables can be studied in nuclear physics laboratories [34, 44]. Nuclear physics labs can measure reactions involving nuclei found in stellar environments and study a variety of nuclear phenomena by varying the incident energy and other experimental parameters. The cross section and the rate of reactions involving specific nuclei, the energy released in the reaction, the nuclear masses and structure of the participating nuclei etc. [10, 22, 57] are examples of the nuclear physics measurements that are widely used in astrophysical model calculations. The study of rates of different reactions, coupled with observations from astronomy allow us to model the birth, evolution and death of stars as well as understand nucleosynthesis and energy production in stars.

Astronomical observations reveal extremely violent explosions of stars. The description of such explosive scenarios requires knowledge of the rates of reactions involving radioactive nuclei. Explosive hydrogen burning [56], hot CNO burning [39] and the *rp* process [13] are some examples where the knowledge of reaction rates is very important. To determine the reaction rates, one needs detailed information on the structure of the participating nuclei. However, the structure of many radioactive nuclei is not well known.

This work describes the measurement of the lifetimes of excited states in ^{19}Ne, an important radioactive nucleus in some explosive events. The Doppler Shift Attenuation Method (DSAM) was used to measure the lifetimes of these states, which range from a few femtoseconds to a few tens of femtoseconds. The rest of this chapter will outline the scenarios where

the ^{19}Ne nucleus plays an important role, the relevance of the measurement of the lifetimes of the states in ^{19}Ne in astrophysical environments and an overview of the experiments done in the past to measure these lifetimes. Chapter 2 discusses the theory behind the DSAM. The experimental details are presented in Chapter 3. Chapter 4 deals with the strategy followed to analyze the data and describes the features of the FORTRAN code that was used to fit the data and extract lifetimes. The results are presented in Chapter 5. The implications of the precise measurements of this work are discussed in Chapter 6. A comparative study of the spins of isobaric states of ^{19}F and ^{19}Ne and the rate calculation for the ^{15}O$(\alpha,\gamma)^{19}$Ne reaction also appear in Chapter 6. The work done in this thesis is summarized in Chapter 7.

1.1 Astrophysical Background

New stars, at the beginning of their life cycles are predominantly ^{1}H. Nuclear fusion occurs in stars via quantum tunneling whereby four ^{1}H nuclei fuse to form one nucleus of ^{4}He and release $\sim$ 30 MeV of energy. Once the hydrogen is depleted in the core of the star, the gravitational force overcomes the pressure, leading to the contraction of the star. The contraction results in a rise of temperature and pressure. The rise of temperature and pressure aids the fusion of ^{4}He nuclei into heavier carbon and oxygen nuclei in stars with masses above $\sim$0.7 solar masses. The star now burns helium and releases energy. Once helium is depleted from the core, the star will contract again, raising temperatures and pressures yet again, resulting in carbon and oxygen burning in sufficiently massive stars. The cycle of contraction and burning of more highly charged nuclei to synthesize even higher mass nuclei continues until the reactions are energetically forbidden. All possible charged particle induced fusion reactions beyond Fe are endothermic and hence energetically unfavorable. The isotopic abundances of elements beyond Fe that are seen in the universe are not explained by these reactions.

Explosive stellar scenarios offer an explanation for some observed isotopic abundances and nucleosynthesis of elements beyond Fe. The explosive scenarios are generally described by sites where the temperatures are higher than 0.1 GK and the densities are in excess of 10^3 g/cm^{-3}, occasionally reaching the nuclear density limit of 10^{14} g/cm^{-3}. Several processes are believed to synthesize nuclei in stellar environments - the s process, the r process, the p process, the rp process etc. In the s process neutron capture occurs along the line of stability, synthesizing higher mass stable isotopes

while the r process takes place far from the line of stability and needs a neutron rich environment. The r process is believed to be responsible for nucleosynthesis of the actinides. The p process synthesizes heavy proton rich nuclei via photodisintegration where an energetic photon knocks particles out of the nucleus. The two important nuclear reactions that contribute to the p process are the knockout of either a neutron or an α particle by the energetic photon from a nucleus with 100 or more nucleons. The rp process requires a hydrogen rich environment at high temperature and density and involves proton captures by seed nuclei interspersed with β^+ decays. The rp process synthesizes light nuclei close to the proton drip line. The time scale for the rp process is usually limited by the β^+ decay rates.

The explosive environments are broadly classified as those occuring in stars of large mass or in binary systems. The former leads to a type II supernova. Binary systems exhibit three explosive phenomena - novae, type Ia supernovae and X-ray bursts.

1.1.1 Type II Supernovae

Type II Supernovae occur in stars that have masses greater than ~ 8 times the solar mass and whose core temperatures are very high (~ 4 GK). Eventually the core is mostly Fe. Since ^{56}Fe has the highest binding energy per nucleon, the fusion of Fe with any other nucleus is energetically unfavorable. However photodisintegration of nuclei and electron capture by protons leads to energy loss from the Fe core and decreases the pressure of the degenerate electron gas. The core then contracts, leading to higher temperatures and densities that approach the nuclear density limit. Beyond this the density cannot be increased and the core collapse stops briefly (for a few miliseconds), resulting in the collapsing material bouncing on the core.

The bounce of the collapsing stellar material leads to an outward compression wave. If this shock wave is strong, the stellar material can get enough energy to escape from the star. There is reason to believe that the shock wave is reenergized by the neutrinos from the core. The ejection of the stellar material leads to a supernova. The large neutron fluxes that occur during the explosion may allow the production of nuclei close to the neutron drip line via the r process.

1.1.2 Binary Systems

It is believed that many stars in the galaxy are binaries - a system where two stars orbit their common centre of mass. If the stars are of unequal

masses, their orbital speeds and rates of evolution differ. The difference in the evolution rate could lead to accretion of material from one star to the other. There are three broad classifications under the binary systems that lead to explosive stellar phenomena.

- Novae

  In novae one of the stars is a white dwarf and the second is a nondegenerate star, typically an aging red giant. If the nondegenerate star fills its Roche lobe [1] during its evolution, material can fall onto the white dwarf. This accreting matter leads to a hydrogen rich layer on the white dwarf. The temperature of the bottom of this layer rises to the point where explosive thermonuclear fusion occurs. The degeneracy is lifted when the local temperature reaches the Fermi temperature, causing a rapid expansion of the material and its ejection into space. The analysis of the abundances in the nova ejecta [30] tests the models for nucleosynthesis and the role of the carbon, nitrogen oxygen cycle [41]. Thermonuclear reactions within the carbon rich white dwarf occur via the Carbon Nitrogen Oxygen (CNO) cycles. Novae also have cycles involving the isotopes of Ne, Na, Mg and Al. The energy generation and the thermonuclear runaway reactions in the novae are due to hydrogen burning. The nova temperatures peak below 0.4 GK.

- Type Ia Supernovae

  In this scenario, the two stars of the binary system are a white dwarf and a companion star. Accretion occurs onto the white dwarf from the companion star until its core mass nears the Chandrasekhar mass limit[2]. The carbon and oxygen burning at these temperatures and pressures causes a explosion that originates at the core of the star. Nuclei heavier than Al are synthesized in type Ia supernovae as is evidenced by their ejecta. However this type of supernova expels only elements up to Ni. The observation of heavier neutron rich and proton rich isotopes cannot be described by this process. While the core explodes in a type Ia supernova, the hydrogen burning in the outer shell of the white dwarf results in a nova explosion.

[1] The Roche lobe is the surface of constant effective gravity (sum of the gravitational forces of the 2 stars and the centrifugal force) around a star in a binary system which contains all the material bound to the star.

[2] The Chandrasekhar mass limit is 1.4 solar mass and is the maximum stellar mass that is stable against contraction due to the pressure of the degenerate electron gas.

- X-ray Bursts

  This explosive scenario occurs when the participating binary consists of a neutron star and a hydrogen rich star. Explosive hydrogen burning in X-ray bursts is discussed in Ref. [51]. Since the neutron star has enormous density, the gravitational force felt by a proton falling on the neutron star is large. Rapid hydrogen burning begins under high temperatures and constant pressure releasing energy and yielding helium. The accreting material thus causes the temperature to rise in the neutron star. When there is sufficient helium at the surface, explosive helium burning begins. The helium nuclei fuse almost completely into carbon nuclei releasing large amounts of energy that can be observed as X-rays. After the helium fuel on the surface has been spent, the accretion starts all over again resulting in periodic X-ray bursts. The peak temperatures for X-ray bursts is ~ 2 GK.

1.1.3 CNO Cycles

Stars burning H into He in their cores are said to be on the main sequence. The energy generation in main sequence stars is thus caused by hydrogen burning. It is well known that the fusion of four protons to form an α particle gives an energy of about 30 MeV. As the temperature increases, reactions involving nuclei with higher atomic number can become important if the reaction cross sections are especially large, as in resonant reactions. The resonant reactions occur when the center of mass energy of the captured nucleus coincides with an excited energy level of the compound nucleus. This greatly enhances the formation of the compound nucleus.

In sufficiently massive stars with substantial amounts of carbon, nitrogen and oxygen isotopes, the CNO cycle dominates over the *pp* chains [6]. The CNO cycle results in the fusion of four hydrogen nuclei to form one helium nucleus in hot, hydrogen rich environments with no change in the relative abundance of the carbon, nitrogen and oxygen nuclei. The CNO cycles are further classified as cold CNO [12] and hot CNO (HCNO) cycles [4, 11] on the basis of the temperature. A schematic sketch of the various reactions and nuclei involved in the CNO cycles is shown in Fig. 1.1 where the nuclei are arranged with increasing neutron number on the abscissa and increasing proton numbers on the ordinate. In Fig. 1.1 the boxes are color coded with respect to temperature. The nuclei in the red boxes (with vertical brown lines) participate in the cold CNO cycle that is operational at temperatures below 0.1 GK. The ^{14}O nucleus in the orange box (with diagonal yellow lines) is produced when the ^{13}N captures a proton above a temperature

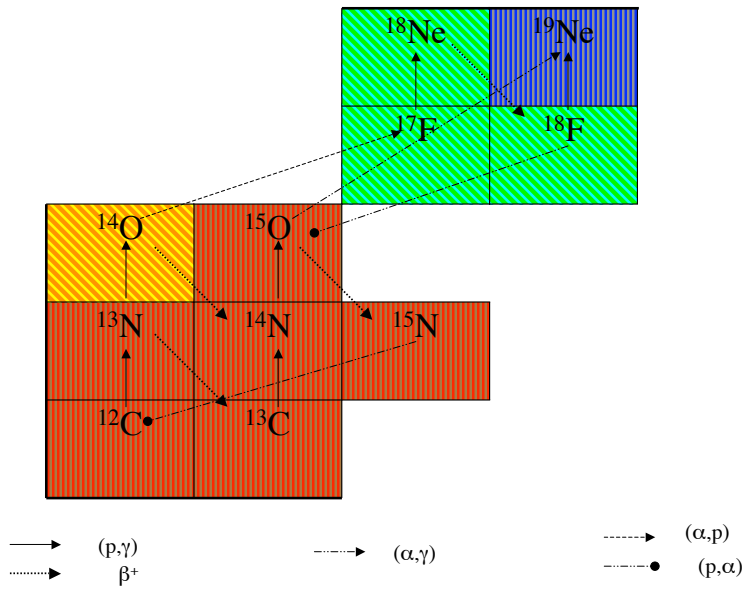

Figure 1.1: The cold and hot CNO cycles. The reactions are differentiated by different arrows. The cold CNO cycle operates in the red boxes, the radiative proton capture by ^{14}O at T $\sim$ 0.2 GK is shown in the orange box and the green and blue boxes operate at T $>$ 0.4 GK.

(T) of 0.1 GK. The nuclei in the green boxes (with diagonal cyan lines) are created at even higher temperatures of $T \sim 0.4$ GK. The ^{19}Ne nucleus in the purple box (with grey vertical lines) is synthesized at temperatures above 0.4 GK. The various reaction mechanisms of (p,γ), (α,γ), (α,p) and β decay are shown by different arrows.

The cold CNO cycles occur for temperatures up to 0.1 GK. The cycle shown in the red boxes in Fig. 1.1 is one of the cold CNO cycles and can be written as

$$^{12}C(p,\gamma)^{13}N(\beta^{+}\nu)^{13}C(p,\gamma)^{14}N(p,\gamma)^{15}O(\beta^{+}\nu)^{15}N(p,\alpha)^{12}C \qquad (1.1)$$

The four hydrogen nuclei fusing to yield one helium nucleus, two positrons and two neutrinos form a complete loop. The mass of the carbon, nitrogen and oxygen nuclei is redistributed to the longest lived isotopes in this cycle,

such that the combined number of carbon, nitrogen and oxygen nuclei is unchanged during the fusion reactions. The rate of energy generation is limited by the slowest process in the cold CNO chain - the β^+ decay rate of ^{15}O.

When the stellar temperature exceeds 0.1 GK, the hot CNO (HCNO) cycles become operational. The stellar thermonuclear explosions occur in systems that have temperature of 0.1 GK and more. At these temperatures, the proton capture by ^{13}N is faster than its β^+ decay. The first hot CNO cycle is

$$^{12}C(p,\gamma)^{13}N(p,\gamma)^{14}O(\beta^+\nu)^{14}N(p,\gamma)^{15}O(\beta^+\nu)^{15}N(p,\alpha)^{12}C \tag{1.2}$$

The two β^+ decays $^{14}O(\beta^+\nu)^{14}$N and $^{15}O(\beta^+\nu)^{15}N$ are the slowest processes in the cycle. In this case, the rates of the two beta decays (^{14}O has a mean lifetime (τ) of 102 s and ^{15}O has a τ of 176 s) determine the energy generation rate of the whole cycle [8]. The β^+ decays of ^{14}O and ^{15}O are temperature independent. However the proton and α capture rates are very sensitive to the temperature at which the reaction occurs. The proton capture reactions by ^{14}O and ^{15}O cannot proceed since ^{15}F and ^{16}F are unbound. At $T < 0.4$ GK, α capture by the oxygen isotopes is highly improbable. Again the cycle is limited by the β decay lifetimes of ^{14}O and ^{15}O.

At temperatures above 0.4 GK, the (α, p) reaction on ^{14}O becomes probable offering the path

$$^{12}C(p,\gamma)^{13}N(p,\gamma)^{14}O(\alpha,p)^{17}F(p,\gamma)^{18}Ne(\beta^+\nu)^{18}F(p,\alpha)^{15}O \tag{1.3}$$

The nuclei highlighted in green (with diagonal cyan lines) in Fig. 1.1 participate in the HCNO chain above 0.4 GK. At these temperatures the ^{14}O$(\alpha,p)^{17}$F reaction occurs at a more rapid rate than the β^+ decay of ^{14}O. The ^{17}F thus formed captures a proton and forms ^{18}Ne at these temperatures. Further proton capture by ^{18}Ne is not possible since ^{19}Na is unbound. The β decay time for the ^{18}Ne nucleus (1.67 s) is long compared to nearly every other reaction in the path. The rate of energy release in this sequence of reactions is limited by the small rate of the ^{17}F$(p,\gamma)^{18}$Ne reaction at these temperatures as well as the half life of the ^{18}Ne nucleus. Moreover the above chain culminates in the ^{15}O nucleus and does not carry the flow out of the HCNO cycle.

The rate of energy release in the HCNO cycles is thus inhibited by the long lifetimes of the isotopes in the HCNO chain - the waiting points[3]. The

[3]The waiting points are the longest lived isotopes in the cycle. In the HCNO case, there are three waiting points - ^{14}O, ^{15}O and ^{18}Ne.

breakout from the HCNO cycle is dependent on the proton or α capture on these long-lived isotopes. One of the following three reactions must occur to either trigger the HCNO breakout or lead to a reaction that will trigger the breakout.

- $^{14}O(\alpha,p)^{17}F$
- $^{15}O(\alpha,\gamma)^{19}Ne$
- $^{18}Ne(\alpha,p)^{21}Na$

These three reactions bridge the proton unbound isotopes ^{15}F, ^{16}F and ^{19}Na.

Once elements heavier than ^{19}Ne are formed, the CNO material cannot be recycled due to Q value constraints. There are three pathways out of the HCNO cycle :

- $^{18}F(p,\gamma)^{19}Ne$
- $^{15}O(\alpha,\gamma)^{19}Ne$
- $^{18}Ne(\alpha,p)^{21}Na$

The first reaction needs ^{18}F which can be produced in two ways

- ^{16}O$(p,\gamma)^{17}$F$(p,\gamma)^{18}$Ne$(\beta^+\nu)^{18}$F
- ^{14}O$(\alpha,p)^{17}$F$(p,\gamma)^{18}$Ne$(\beta^+\nu)^{18}$F

The two reactions listed above are critically dependent on the cross section for the ^{17}F(p,γ) reaction which is smaller than earlier predictions [7, 27–29, 40, 46, 62]. ^{18}Ne formed via the ^{17}F(p,γ) β^+ decays into ^{18}F. Once formed ^{18}F is almost always recycled back into ^{15}O by the ^{18}F(p,α) reaction. It is believed that only the ^{15}O$(\alpha,\gamma)^{19}$Ne or the ^{18}Ne$(\alpha,p)^{21}$Na could carry the flow out of the HCNO cycle. The ^{18}Ne$(\alpha,p)^{21}$Na reaction has the largest Coulomb barrier of the three pathways and is believed to contribute only at higher temperatures and densities [61]. ^{15}O$(\alpha,\gamma)^{19}$Ne, the third reaction is currently believed to be the most probable path through which the HCNO cycle is broken [13]. It contributes to the breakout from the CNO cycle at temperatures lower than those required for the other possible reactions [27, 63]. If the α capture rate of ^{15}O exceeds its β decay rate, ^{19}Ne is formed which captures a proton forming ^{20}Na. The ^{20}Na β^+ decays to ^{20}Ne which is stable, thus breaking out of the HCNO cycle and into the rp process. While the β decay rates of ^{14}O and ^{15}O are temperature independent, the α and p capture rates by the oxygen isotopes are very sensitive

to temperature, rising with temperature. Since ^{15}O is abundant (due to its long lifetime) even a small rate of the ^{15}O$(\alpha,\gamma)^{19}$Ne reaction would release energy causing a rise in temperature [49]. A rise in temperature favors an increase in the rate of the ^{15}O$(\alpha,\gamma)^{19}$Ne reaction, generating more energy and raising the temperature further such that a thermonuclear runaway occurs. The ^{15}O$(\alpha,\gamma)^{19}$Ne reaction thus triggers a breakout from the HCNO cycle into the *rp* process.

At high temperatures, explosive stellar phenomena such as X-ray bursts reveal signatures of break out from the HCNO cycle [61]. The bursts are observed with characteristic time periods and a dramatic increase in the luminosity. The energy generation in the HCNO cycle is limited by the lifetimes of ^{14}O and ^{15}O isotopes; only a breakout from the HCNO cycles offers an explanation for the large energy output observed during the burst. The recurring pattern of the bursts is also explained by examining the reaction mechanisms in exploding binary systems. The dynamics of all reactions that could lead to a breakout from the HCNO cycle have to be studied thoroughly. The reaction rates or the nuclear properties that determine them have to be measured accurately to serve as input parameters for the astrophysical model calculations. The ^{15}O $(\alpha,\gamma)^{19}$Ne reaction is the subject of this work. The lifetimes of the states in ^{19}Ne above the ^{15}O+α threshold have been measured in this work. These lifetimes are needed to calculate the reaction rate.

1.2 Motivation

In normal stellar environments, the stellar gas is nondegenerate and in thermal equilibrium. The ions move nonrelativistically and the velocity distribution of ions is Maxwellian. If the masses of the reacting particles are m_1 and m_2, the reaction rate per particle pair is the product of the reaction cross-section σ and the relative velocity v, averaged over the distribution of velocities [23, 47]

$$< \sigma v >= (\frac{8}{\pi\mu})^{\frac{1}{2}}(k_B T)^{-\frac{3}{2}} \int_0^\infty \sigma(E) E e^{-\frac{E}{k_B T}} dE \tag{1.4}$$

Here μ is the reduced mass of the system and is $\frac{m_1 m_2}{m_1+m_2}$, k_B is the Boltzmann constant, E is the relative kinetic energy and T is the temperature of the environment.

The reaction cross-section generally has nonresonant as well as resonant contributions. However since the resonant cross-section is quite often large,

the contribution from the resonances is generally dominant. For a particular resonance at relative energy E_r with angular momentum J, the cross section is given by the Breit-Wigner form

$$\sigma(E) = \frac{\pi\omega}{k^2}\frac{\Gamma_a\Gamma_b}{(E-E_r)^2+(\frac{\Gamma}{2})^2} \tag{1.5}$$

Here

- k is the wave number and is given by $\sqrt{\frac{2\mu E}{\hbar^2}}$
- ω is the statistical spin factor and is $\frac{2J+1}{(2J_a+1)(2J_b+1)}$
- J_a and J_b are the spins of the reacting particles and
- Γ is the width of the resonance
- Γ_a and Γ_b are the partial widths of the entrance and exit channels a and b.

The cross section due to an (α,γ) resonance is

$$\sigma(E) = \frac{\pi\omega}{k^2}\frac{\Gamma_\alpha\Gamma_\gamma}{(E-E_r)^2+(\frac{\Gamma}{2})^2} \tag{1.6}$$

If the reaction rate is dominated by a single resonance, the integral in Eq. 1.4 can be solved and the reaction rate is

$$< \sigma v >_i = (\frac{2\pi}{\mu kT})^{\frac{3}{2}}\hbar^2\omega_i\frac{\Gamma_a\Gamma_b}{\Gamma}e^{-\frac{E_r}{k_BT}} \tag{1.7}$$

The temperature dependence of the reaction rate is seen in Eqs. 1.4 and 1.7. If several narrow, isolated resonances contribute to the reaction rate, the value of the reaction rate for each resonance can be calculated with Eq. 1.7 and all the individual rates can be added to yield the total reaction rate.

The total width Γ of an excited state is generally the sum of the widths of all possible decay channels.

$$\Gamma = \sum_i \Gamma_i \tag{1.8}$$

where i runs over all possible channels of decay.

In the reaction studied in this work, the emphasis is on the excited states in ^{19}Ne in the 4 - 5 MeV range, just above the ^{15}O+α threshold. The proton and neutron separation energies in ^{19}Ne are 6.4 and 11.6 MeV respectively.

Since the nucleon emission thresholds for the levels in ^{19}Ne are at least a couple of MeV higher than the resonances studied, the resonances typically decay by emitting an α particle or a γ ray. The above equation (Eq. 1.8) then simplifies to

$$\Gamma = \Gamma_\alpha + \Gamma_\gamma \tag{1.9}$$

In several cases, the γ width Γ_γ is several orders of magnitude larger than the α width (i.e.).$\Gamma_\gamma \gg \Gamma_\alpha$. In such cases, the total width $\Gamma \sim \Gamma_\gamma$.

Populating the states and observing their decay by α and γ emission leads to the measurement of the α branching ratio B_α which is defined as

$$B_\alpha = \frac{\Gamma_\alpha}{\Gamma} \tag{1.10}$$

If we define

$$\gamma = \frac{\Gamma_\alpha \Gamma_\gamma}{\Gamma} \tag{1.11}$$

the resonance strength $\omega\gamma$ is then described by the following equation:

$$\omega\gamma = \frac{2J+1}{(2J_{^{15}O}+1)(2J_\alpha+1)} \frac{\Gamma_\alpha \Gamma_\gamma}{\Gamma_\alpha + \Gamma_\gamma} \tag{1.12}$$

where the $J_{\alpha/^{15}O}$ stands for the spins of the α particle or the ^{15}O nucleus and J stands for the spin of the resonance.

To estimate the reaction rate, one needs to know the resonance strength. Besides the spins of the resonances, knowledge of the resonance strength requires an accurate determination of any two of the three quantities mentioned above, i.e., Γ_α, Γ_γ and the α decay branching ratio B_α. This can be seen by rearranging Eq. 1.11.

$$\gamma = \frac{\Gamma_\alpha \Gamma_\gamma}{\Gamma} = \Gamma_\gamma B_\alpha = \Gamma_\alpha(1 - B_\alpha) = B_\alpha(1 - B_\alpha)\Gamma \tag{1.13}$$

A measurement of the total width of the relevant level is therefore important. The total width Γ is related to the lifetime τ of the state via the equation

$$\Gamma = \frac{\hbar}{\tau} \tag{1.14}$$

In cases where $\Gamma_\gamma \gg \Gamma_\alpha$, the radiative width Γ_γ is almost equal to the total width Γ

$$\Gamma_\gamma \sim \Gamma \tag{1.15}$$

Thus a measurement of the lifetime gives information on Γ and in some cases, on Γ_γ.

It is believed that non-resonant α capture by ^{15}O does not contribute significantly to the reaction rate ^{15}O$(\alpha,\gamma)^{19}$Ne at temperatures relevant to accreting neutron stars [13, 36]. Rather resonant α capture by ^{15}O leading to states in ^{19}Ne above the α + ^{15}O threshold of 3.53 MeV dominate the reaction rate. The study of states in ^{19}Ne above the α breakup threshold of 3.53 MeV yields information that is important in the rate calculations of the ^{15}O$(\alpha,\gamma)^{19}$Ne reaction. As discussed in Sec. 1.1.3, this reaction is the dominant pathway for the breakout from the HCNO cycle at low temperatures.

At temperatures below 2 GK, the ^{15}O$(\alpha,\gamma)^{19}$Ne reaction depends strongly on resonances at $E_{cm} \simeq 500$ keV and to a lesser extent on other resonances at $E_{cm} \simeq 850$ keV and 1070 keV [37]. These resonances correspond to the $\frac{3}{2}^+$ state at 4034.5(8) keV in ^{19}Ne, the $\frac{7}{2}^+$ state at 4377.8(6) keV in ^{19}Ne and the $(\frac{5}{2})^+$ state at 4601.8(8) keV in ^{19}Ne respectively [53, 54]. The decay properties of these resonances determine their strengths.

The determination of the resonance strengths requires accurate measurement of the spins, branching ratios B_α and the lifetimes. All three quantities are needed for each resonance. Several groups have measured and established upper limits for B_α [14, 35, 45, 52, 55]. The values of the excitation energy E_x, the spin J^π and B_α for the various states of interest are summarized in Table. 1.1. These values are used later (in Chapter 6) to calculate reaction rates.

The aim of this experiment was to measure the lifetimes of the states in ^{19}Ne above the α threshold. Earlier attempts to measure the lifetimes will be discussed in the next section. While most earlier attempts list only upper or lower limits to the lifetimes, one recent experiment has measured the lifetimes of six states above the α threshold [53] while another experiment measured the lifetime of the 4.035 MeV state [32]. The lifetime of the 4035 keV state measured here agrees with the two earlier measurements for this state but is more precise. The lifetimes of the other five states measured here agree with the only other measurement and are considerably more precise in some cases.

1.3 Previous Attempts

The lifetimes of the levels in ^{19}Ne in the energy range of 4 - 5 MeV have interested several experimental groups for over 3 decades now. These levels in ^{19}Ne are above the ^{15}O $+\alpha$ threshold, as is evident from Fig. 1.2.

The γ decay from the excited states in ^{19}Ne in the 4-5 MeV range was

E_x (MeV)	J^π	B_α
4.035	$3/2^+$	$4.3\times10^{-4\ UL}$
4.378	$7/2^+$	$3.9\times10^{-3\ UL}$
4.548	$(3/2)^-$	0.10±0.02
4.602	$(5/2)^+$	0.30±0.02
4.712	$(5/2)^-$	0.85±0.04
5.092	$5/2^+$	0.90±0.05

Table 1.1: The spins and α decay branching ratios of states in ^{19}Ne above the α threshold [14]. The superscripts ^{UL} on the 4.035 MeV and the 4.378 MeV levels refer to 90% Confidence Level (CL) upper limits on B_α.

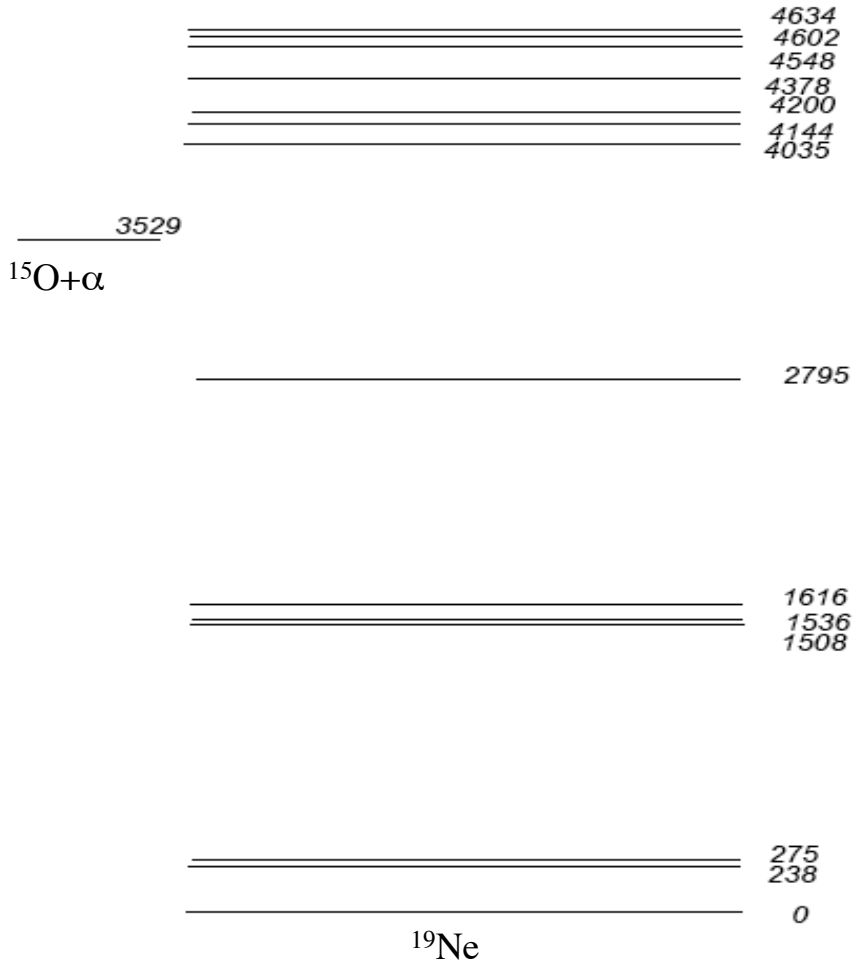

Figure 1.2: The levels in ^{19}Ne are shown on the right of the figure. The ^{15}O $+\alpha$ threshold is also shown for reference. The energies of the levels are expressed in keV.

first studied extensively by Davidson and Roush. These authors used the ^{17}O(^{3}He, nγ)^{19}Ne reaction at the three incident energies of 3, 4 and 5 MeV. They reported several new transitions in the 4-5 MeV range in ^{19}Ne by analyzing the n-γ coincidence spectra. The strongest transitions from the new states were identified. The lifetimes of the states were measured using DSAM. Comparisons were drawn between these new states in ^{19}Ne and the isobaric analog states in ^{19}F [54]. The authors placed upper or lower bounds on the lifetimes of all these states. The lifetimes of six levels from 4.03 MeV to 4.60 MeV had upper bounds on their lifetimes. In particular the 4.03 MeV state had an upper limit of 50 fs and the level at 4.63 MeV had a lower bound of 1 ps. Table 1.2 summarizes the results of their experiment. It must be noted that while the authors observed the weaker branches from the new states, they did not measure the branching ratios of the new states. Table 1.2, thus, reflects the lifetime measurements using the strongest observed transitions from the listed states.

After a suggestion by Wallace and Woosley in 1981 [56] that the first level in ^{19}Ne above the ^{15}O + α breakup threshold dominates the reaction rate for breakout from the hot CNO cycles, the $\frac{3}{2}^{+}$ level at 4.03 MeV in ^{19}Ne was studied with two different techniques: the Doppler Shift Attenuation Method (DSAM) and the Coulomb excitation method, Coulex.

The width of the 4.03 MeV state was studied in 2000 using Coulomb excitation. Inelastically scattered ^{19}Ne ions were measured in coincidence with γ rays. These measurements suggested a lower limit of 1.8 fs for the lifetime of the astrophysically important 4.03 MeV state in ^{19}Ne [26]. Thus one experiment with ^{19}Ne put an upper limit of 50 fs on the lifetime of the 4.03 MeV state while another set a lower limit of 1.8 fs.

There have been two other measurements of the lifetimes of the 4.03 MeV state in ^{19}Ne. Recently, an experiment at Notre Dame University measured the lifetime of the state to be 13^{+16}_{-9} fs [53]. The ^{19}Ne levels were populated via the ^{17}O(^{3}He,nγ)^{19}Ne reaction at an incident energy of 3 MeV. The lifetime was measured with DSAM. Besides the 4.03 MeV state, the energy levels and the lifetimes of several states above the ^{15}O $+\alpha$ threshold were reported. The results of this experiment are shown in Table 1.3.

The states of interest in ^{19}Ne cannot be populated via the reaction ^{15}O$(\alpha,\gamma)^{19}$Ne since ^{15}O is radioactive and cannot be used as a target. If we impinge the ^{15}O beam on an α target, we need intensities for the ^{15}O beam that are currently unavailable in radioactive beam facilities around the world. At TRIUMF-ISAC we populated the states in ^{19}Ne above the α threshold via the reaction ^{3}He(^{20}Ne, α)^{19}Ne. In the preliminary run we populated only the 4.03 MeV state in ^{19}Ne. This preliminary run employed

Transitions (MeV)	Lifetime (ps)
$4.03 \rightarrow 0.00$	< 0.050
$4.14 \rightarrow 1.51$	< 0.30
$4.20 \rightarrow 1.51$	< 0.35
$4.38 \rightarrow 0.24$	< 0.12
$4.55 \rightarrow 0.28$	< 0.08
$4.55 \rightarrow 0.00$	< 0.08
$4.60 \rightarrow 0.24$	< 0.16
$4.63 \rightarrow 2.79$	> 1.0

Table 1.2: The strongest observed transitions from states in ^{19}Ne above 3.53 MeV and their lifetimes, as measured by Davidson and Roush[17].

the scattering chamber fabricated for this purpose and used DSAM. The Doppler shift of the 4.03 MeV level was seen and the lifetime agreed with the earlier measurement. The lifetime was measured to be 11^{+4}_{-3} fs [32]. However no state above 4.03 MeV was seen clearly in the experiment. The experiment was improved to populate the levels in ^{19}Ne above 4.03 MeV. To facilitate this, several modifications were made to the scattering chamber to improve the target cooling. The improved cooling of the target and a careful preparation of the implanted target greatly improved the signal to noise ratio in the second run of the experiment.

The thesis reports on the data collected in the second run of the experiment that ran for a week from September 5th 2006. The experiment was a collaboration between 7 universities and laboratories in Canada. My contributions can be found in Appendix H.

Energy levels (keV)	Lifetime (fs)
1507.5(4)	$(1.7\pm0.3)\times10^3$
1536.1(4)	16 ± 4
1615.4(4)	80 ± 15
2794.2(4)	100 ± 12
4034.5(8)	13^{+9}_{-6}
4143.5(6)	18^{+2}_{-3}
4200.3(11)	43^{+12}_{-9}
4377.8(6)	5^{+3}_{-2}
4547.7(10)	15^{+11}_{-5}
4601.8(8)	7^{+5}_{-4}
4634.0(9)	>1000

Table 1.3: Levels in ^{19}Ne and their lifetimes measured by the authors of Ref. [53] .

Chapter 2

Doppler Shift Attenuation Method

The Doppler shift is the change in the observed frequency of a wave due to the relative motion of the observer and the wave source. Doppler shifts find wide applications in several fields. Astronomy is one such field where astronomers use the Doppler shift to measure the radial velocity of stars. The spectra of stars show absorption lines that are characteristic of the composition of the star. A shift observed in the stellar absorption lines from rest frame laboratory sources is a measure of the radial velocity of the star.

In a nuclear reaction when an excited state of the product nucleus is populated, the γ ray emitted by the product nucleus suffers a Doppler shift dependent on the velocity of the nucleus. As the excited nucleus traverses the target material, it suffers an energy loss that results in a change of the velocity. The energy loss suffered by the excited nucleus in turn affects the Doppler shift of the emitted γ ray.

The Doppler Shift Attenuation Method (DSAM) relies on the Doppler shift and the attenuation suffered by emitting source (in the medium) to extract lifetimes of excited nuclear states. The shape of the Doppler shifted γ ray spectrum (line shape) is dependent on two parameters: the lifetime and the energy loss of the γ emitting nucleus. The lifetime is an intrinsic property of the state - the γ rays from a short lived state will suffer a larger Doppler shift than those from a long-lived one, all other parameters being the same. As the recoiling ion traverses the target medium it loses energy. The loss of energy is dependent on the density of the target medium and also on the characteristic stopping power of the ion. Thus the lifetime of the excited state and the stopping power of the target medium determine the Doppler shift of a transition.

Besides this shift, the line shape is also subjected to Doppler broadening. This broadening depends on the kinematics and the size and placement of the detectors used in the experiment. The finite solid angle of the detector and the velocity distribution of the recoiling ions both contribute to the Doppler broadening. The observed line shape is a convolution of the Doppler shift

and the Doppler broadening.

For a specific experimental setup, the effect of different lifetimes is seen in Fig. 2.1. The ^{3}He(^{20}Ne,α)^{19}Ne reaction was simulated at 34 MeV. The 4035 keV state in ^{19}Ne was populated in the simulations. The actual experimental solid angle and detector resolution were incorporated into the simulations. The recoiling ^{19}Ne ions passed through 12.5 μm of Au as they slowed down. The simulated line shapes for different lifetimes for the 4035 keV state in ^{19}Ne are plotted in Fig. 2.1. The abscissa is the Doppler shift and the ordinate shows the intensity. The top panel shows line shapes corresponding to lifetimes of 10 fs, 100 fs, 150 fs and 250 fs. The lower panel shows the line shapes corresponding to 1 fs, 10 fs, 50 fs and 100 fs. The number of ions that were allowed to decay was the same for each lifetime and therefore the area under each curve is identical. As is evident from Fig. 2.1, the average Doppler shift is maximum for the shortest lifetime. In both panels, as the lifetimes increase, two effects are observed - the Doppler shifts decrease and so do the slopes of the low energy tail. The long lifetimes have a smaller Doppler shift and a long low energy tail. Looking at the line shapes corresponding to lifetimes of 150 fs and 250 fs, we see a substantial contribution from the unshifted γ transitions as well as the Doppler shifted γ rays. This indicates that as lifetimes increase, the recoiling ions come to a stop before they decay and hence contribute largely to the unshifted γ ray peak. For lifetimes in the range of $100 < \tau < 250$ fs, the unshifted and Doppler shifted γ rays are both seen. We observed such a transition in the experiment and will discuss the details in Sec. 5.3.

2.1 Theory of the DSAM

The Doppler shift ΔE_γ for photons emitted from a moving source is

$$\Delta E_\gamma = E_\gamma^0[\frac{(1-\beta^2)^{\frac{1}{2}}}{1-\beta cos\theta} - 1] \tag{2.1}$$

where E_γ^0 is the unshifted gamma ray energy, β is the speed of the source in units of the speed of light and θ is the angle between the velocity of the source ($\vec{v}$) and the γ ray ($\vec{k}_\gamma$)

$$cos\theta = \frac{\vec{v}\cdot\vec{k}_\gamma}{|\vec{v}||\vec{k}_\gamma|} \tag{2.2}$$

When the speed of the source is much less than the speed of light (when $\beta \ll 1$), the above expression can be expanded in a Taylor series. Since the

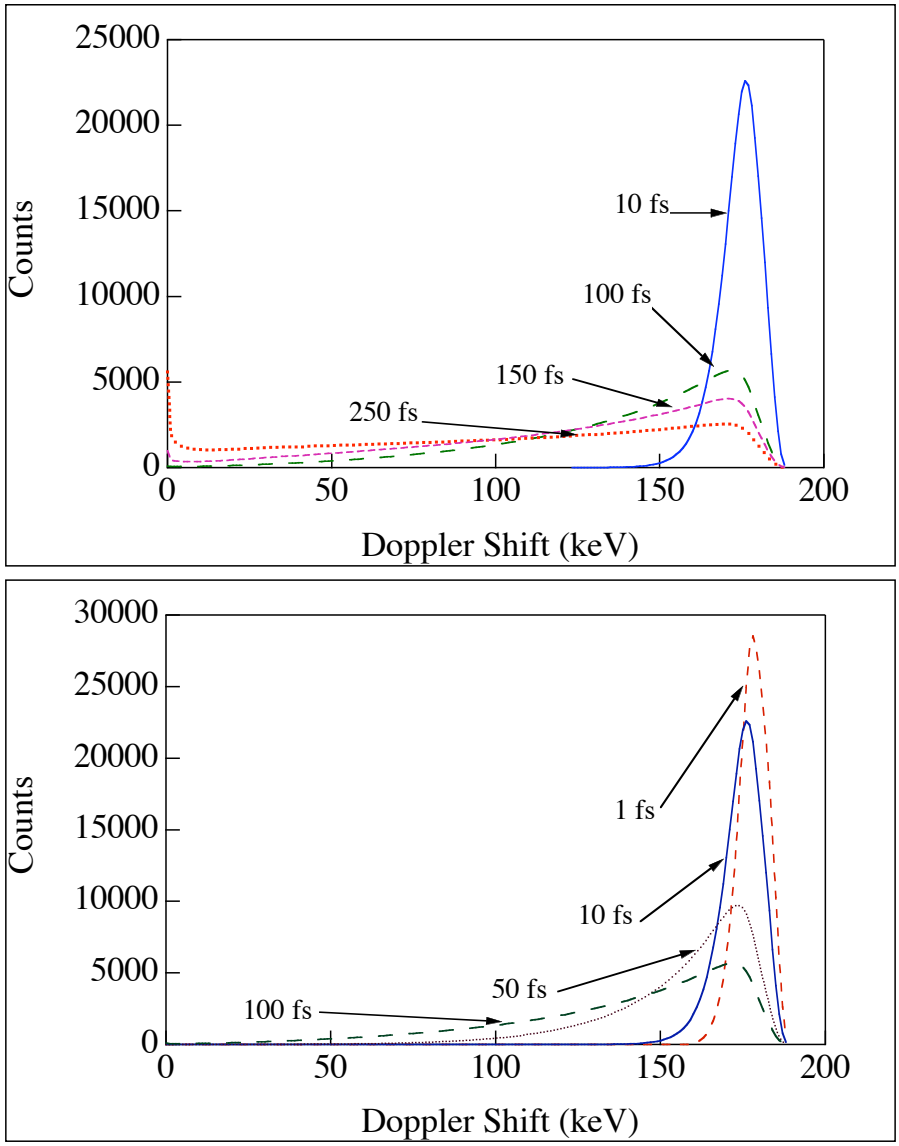

Figure 2.1: Line shapes of the 4035 keV state in ^{19}Ne corresponding to different lifetimes. The ^{19}Ne recoils were simulated in the ^{3}He(^{20}Ne,α)^{19}Ne reaction at a beam energy of 34 MeV and lost energy in 12.5 μm of Au. More details appear in the text.

source of the γ ray loses energy in the target medium, the velocity of the source changes with time. The variation of β gives rise to a distribution of γ energies.

Expanding Eq. 2.1 and keeping terms up to only the second order in β,

$$\Delta E_\gamma = E_\gamma^0(\beta cos\theta - \frac{\beta^2}{2} + \beta^2 cos^2\theta) \tag{2.3}$$

The observed γ energy is

$$E_\gamma = E_\gamma^0 + \Delta E_\gamma \tag{2.4}$$

Since the energy distribution has an implicit θ and time dependence Eq. 2.4 can be expressed as

$$E_\gamma(\theta, t) = E_\gamma^0[1 + \beta(t)cos\theta - \frac{\beta(t)^2}{2} + \beta(t)^2 cos^2\theta] \tag{2.5}$$

where the variation of β with time due to the recoiling ion losing velocity in the target is shown explicitly. To first order in β, the distribution of the γ spectrum will be continuous between E_γ^0 and $E_\gamma^0(1 + \beta(t = 0)cos\theta)$.

The line shape of the γ transition is the variation of the number of decaying nuclei in the γ spectrum as a function of the velocity of the recoiling nuclei. If the velocity of N recoiling nuclei that are excited to a state of lifetime τ at time t is v, then after a small time interval of dt, the velocity decreases by dv due to the stopping power. The number of recoiling nuclei decreases to N−dN as the excited state decays. The velocity of the nuclei at $t + dt$ is v−dv. The number of nuclei decaying between t and $t + dt$ is then dN(v) and can be calculated with a detailed knowledge of the stopping power.

Stopping Power

The energy loss of an ion is dependent on three quantities - its energy, the thickness of the target it traverses and its characteristic stopping power. A heavy ion (Z>2) with a β of 0.04− 0.06 stops in a dense material within a few hundred fs. If a state of the recoiling nucleus has a lifetime in the range of 1 fs to a 100 fs, a substantial fraction of the nuclei will decay as the nuclei slow down.

There are two ways the heavy ion can lose energy in the medium - via electronic collisions or via nuclear collisions. The energy losses due to the two processes depend on their respective stopping powers. The electronic

stopping refers to inelastic collisions between the heavy ion and the electrons attached to the atoms in the solid target. The electronic stopping power is characterized by small energy and momentum transfers due to large impact parameters (large distances between the incoming ion traveling in a straight line trajectory and the stationary target). The nuclear stopping refers to elastic collisions of the ion and the target nuclei. The nuclear stopping power is dominant at low energies and causes large deflections and energy transfers. In the energy region studied here, the electronic energy loss is dominant.

Each ion has a characteristic stopping power that is dependent on its mass and charge and also on the composition of the target. The dependence of the stopping power on the properties of the recoiling ion and on the density of the target material is shown explicitly in the equations described below.

The energy loss for the heavy ions with velocities close to the Bohr velocity (2.46×10^6 m/s) has been studied in several experiments. The stopping powers are fitted phenomenologically [50, 60] by

$$\frac{1}{\rho}\frac{dE}{dx} = K_e\frac{v}{v_0} + K_n(\frac{v}{v_0})^{-1} \tag{2.6}$$

where

- v_0 is the Bohr velocity and is αc where α is the fine structure constant given by $\frac{e^2}{\hbar c}$,
- v is the velocity of the recoiling ion,
- the coefficients K_e and K_n represent electronic and nuclear stopping coefficients and are obtained from experimental data and
- ρ is the density of the material in which the ion is slowing down.

Eq. 2.6 is used when the heavy ions have initial velocities v_i in the range of $0.1 < v_i/v_0 < 6$ [59].

We consider the reaction $M_t(m_p, m_e)M_r^*$ at a beam energy E_1. Here M_t stands for the mass of the target, m_p for the mass of the projectile, m_e the mass of the ejectile and M_r^* the mass of the recoiling ion. The ground state Q value of the reaction is M_t+m_p-m_e-M_r. The excitation energy E_x corresponding to the energy of the excited state of the recoiling ions M_r is included in the total mass of the recoiling ion denoted as M_r^*. All masses and energies are measured in MeV.

We assume that N_0 monoenergetic, unidirectional recoils in an excited nuclear state with excitation energy E_x and lifetime τ slow down in a medium

from their initial velocity v_i. The energy loss per unit distance can be equated to the force felt by the recoiling ion, i.e. -M$_r \frac{dv}{dt}$.

$$-M_r \frac{dv}{dt} = \frac{dE}{dx} \tag{2.7}$$

Rewriting Eq. 2.6

$$\frac{-M_r}{\rho}\frac{dv}{dt} = K_e \frac{v}{v_0} + K_n (\frac{v}{v_0})^{-1} \tag{2.8}$$

Multiplying and dividing the left side of Eq. 2.8 by the Bohr velocity v_0 we get

$$\frac{-M_r v_0}{\rho}\frac{d}{dt}(\frac{v}{v_0}) = K_e \frac{v}{v_0} + K_n (\frac{v}{v_0})^{-1} \tag{2.9}$$

Rearranging

$$\frac{-M_r v_0}{\rho K_e}\frac{d}{dt}(\frac{v}{v_0}) = \frac{v}{v_0} + \frac{K_n}{K_e}(\frac{v}{v_0})^{-1} \tag{2.10}$$

We now multiply both sides of the equation by $\frac{v}{v_0}$ and get

$$\frac{-M_r v_0}{\rho K_e}\frac{v}{v_0}\frac{d}{dt}(\frac{v}{v_0}) = (\frac{v}{v_0})^2 + \frac{K_n}{K_e} \tag{2.11}$$

$$\Rightarrow \frac{-M_r v_0}{2\rho K_e}\frac{d}{dt}(\frac{v}{v_0})^2 = (\frac{v}{v_0})^2 + \frac{K_n}{K_e} \tag{2.12}$$

Replacing $\frac{M_r v_0}{K_e \rho}$ by ζ, Eq. 2.12 can be rewritten as

$$\frac{-\zeta}{2}\frac{d}{dt}(\frac{v}{v_0})^2 = (\frac{v}{v_0})^2 + \frac{K_n}{K_e} \tag{2.13}$$

A change of the variable is done in Eq. 2.13. We set

$$W = (\frac{v}{v_0})^2 + \frac{K_n}{K_e} \tag{2.14}$$

Since $\frac{K_n}{K_e}$ does not vary with time, $\frac{dW}{dt}$ is $\frac{d}{dt}(\frac{v}{v_0})^2$. Eq. 2.13 then becomes

$$\frac{-\zeta}{2}\frac{dW}{dt} = W \tag{2.15}$$

Eq. 2.15 can be integrated to yield

$$W(t) = C_1 e^{\frac{-2t}{\zeta}} \tag{2.16}$$

$$\Rightarrow (\frac{v}{v_0})^2 + \frac{K_n}{K_e} = C_1 e^{\frac{-2t}{\zeta}} \tag{2.17}$$

where C_1 is evaluated by imposing the boundary conditions.

At time t=0, the velocity v is the initial velocity v_i. Then $(\frac{v(t=0)}{v_0})^2$ is $(\frac{v_i}{v_0})^2$. Then the constant C_1 is $(\frac{v_i}{v_0})^2 + \frac{K_n}{K_e}$.

Putting it all together, the solution to Eq. 2.12 can be written as

$$(\frac{v}{v_0})^2 + \frac{K_n}{K_e} = [(\frac{v_i}{v_0})^2 + \frac{K_n}{K_e}]e^{\frac{-2t}{\zeta}} \tag{2.18}$$

Rearranging

$$(\frac{v}{v_0})^2 = [(\frac{v_i}{v_0})^2 + \frac{K_n}{K_e}]e^{\frac{-2t}{\zeta}} - \frac{K_n}{K_e} \tag{2.19}$$

The velocity v is a function of time. This is seen in Eq. 2.19 where the time dependence is evident in the exponent. Expressing $\frac{v}{v_0}$ as V(t) and $\frac{v_i}{v_0}$ as V_i, we can rewrite the above equation Eq. 2.19 as

$$V(t)^2 = (V_i^2 + \frac{K_n}{K_e})e^{-\frac{2t}{\zeta}} - \frac{K_n}{K_e} \tag{2.20}$$

The form of the velocity V(t) seen in Eq. 2.20 is useful to derive the variation of the number of recoils as a function of the velocity V(t), i.e $\frac{dN(V)}{dV}$.

Using Eq. 2.20, we can express the time t in terms of the V(t) and V_i. Rearranging Eq. 2.20, we have

$$t = \frac{\zeta}{2} ln[\frac{V_i^2 + \frac{K_n}{K_e}}{V(t)^2 + \frac{K_n}{K_e}}] \tag{2.21}$$

When V(t) reaches zero the decaying nuclei contribute only to the unshifted γ ray line shape. The cut-off time t_c is defined as the time when V(t)=0. Using Eq. 2.21, t_c is

$$t_c = \frac{\zeta}{2}[ln(V_i^2 + \frac{K_n}{K_e}) + ln\frac{K_e}{K_n}] \tag{2.22}$$

All nuclei decaying after the cut-off time will not emit Doppler shifted γ rays. The number of nuclei that contribute to the line shape N(t) is the difference between the total number of decaying ions N_0 at t=0 and the number of nuclei N_c that survive at the cut-off time t_c.

$$N(t) = N_0 - N_c \tag{2.23}$$

From the exponential decay law,

$$N(t) = N_0 e^{-\frac{t}{\tau}} \tag{2.24}$$

The rate of decay is

$$\frac{dN}{dt} = -\frac{N_0}{\tau} e^{-\frac{t}{\tau}} \tag{2.25}$$

Rearranging Eq. 2.25 we can write

$$dN = -\frac{N_0}{\tau} e^{-\frac{t}{\tau}} dt \tag{2.26}$$

Expressing t and dt in terms of V(t) from Eq. 2.21, we can rewrite Eq. 2.26 as

$$dN = \frac{N_0}{\tau} \zeta [\frac{V(t)^2 + \frac{K_n}{K_e}}{V_i^2 + \frac{K_n}{K_e}}]^{\frac{\zeta}{2\tau}} \frac{V(t)}{V(t)^2 + \frac{K_n}{K_e}} dV \tag{2.27}$$

Thus one finds a direct correlation between the velocity distribution of the recoiling ions and the lifetime of the decaying states.

However one has to account for the nuclei that are in the excited state beyond the cut-off time. The variation of the number of decaying nuclei with velocity can then be written as

$$\frac{dN(V)}{dV} = \frac{N_0}{\tau} \zeta [\frac{V(t)^2 + \frac{K_n}{K_e}}{V_i^2 + \frac{K_n}{K_e}}]^{\frac{\zeta}{2\tau}} \frac{V(t)}{V(t)^2 + \frac{K_n}{K_e}} + N_c \delta(V(t)) \tag{2.28}$$

The second term on the right side of Eq. 2.28 accounts for the nuclei that decay after the cut-off time and contribute to the unshifted γ ray spectrum. For long lived excited states, the recoiling ion comes to a stop before emitting a γ ray. In this case no Doppler shift is observed and the first term of Eq. 2.28 is zero. Integrating the second term over the velocity V ensures the conservation of the total number of decaying nuclei.

The line shape is broadened by the solid angle subtended by the γ detector and the range of the initial velocities of the recoiling ions. The experiment should be designed to minimize the line broadening by producing an ensemble of recoiling ions that are unidirectional and monoenergetic [21].

From kinematics, the component of the velocity of the recoiling ion in the lab along the beam direction (taken as the z axis) at time t = 0 is given by

$$\beta_z(0) = \beta_{cm}(1 + \eta^{-1} cos\theta_{cm}) \tag{2.29}$$

where

$$\eta^{-1} = \frac{M_t m_e}{m_p M_r^*} [1 + \frac{m_p + M_t}{m_e + M_r} \frac{(m_p + M_t) Q'}{M_t E_1}]^{1/2} \tag{2.30}$$

Q$^{'}$ refers to the difference between the ground state Q value of the reaction and the energy of the excited nuclear state (E$_x$).

$$Q^{'} = Q - E_x \tag{2.31}$$

The factor $(m_p + M_t)/\ (m_e + M_r)$ is close to 1 since the mass of the reactants is almost equal to the mass of the proucts. Therefore Eq. 2.30 simplifies to

$$\eta^{-1} = \frac{M_t m_e}{m_p M_r^*}[1 + \frac{(m_p + M_t)Q^{'}}{M_t E_1}]^{1/2} \tag{2.32}$$

The other factors in Eq. 2.29 are

- β_{cm} is the velocity of the center of mass (in units of c) and
- θ_{cm} is the center of mass angle of the recoiling ion.

In order to do a lifetime measurement using the DSAM, it is imperative to reduce the spread in velocity for the recoils. This implies minimizing the value of η^{-1}. There are several ways of minimizing this spread. Looking at Eq. 2.32, it is seen that η^{-1} depends on the masses of the target, projectile, ejectile and the recoiling ion as well as on the value of $Q^{'}$. Looking at the square bracket in Eq. 2.32, it is clear that a second term determines the magnitude of η^{-1}. Since there is a Q$^{'}$ dependence for η^{-1} , a positive value for Q$^{'}$ would increase η^{-1} and a negative value for Q$^{'}$ would decrease η^{-1}, reducing the spread of the recoils. A reaction in inverse kinematics ($M_t < m_p$) with a negative value for Q$^{'}$ will reduce η^{-1} even further. The advantages of using inverse kinematics are summarized in the next section.

The response of the detector has to be folded into the line shape before comparing with the experimental data. There are two different responses of the detector that need consideration. They are the geometric efficiency of the detector and the intrinsic response of the detector. Both the intrinsic response and the geometric efficiency affect the line shape.

2.2 Advantages of Inverse Kinematics in DSAM

The DSAM has been used to measure lifetimes of nuclear states in the range of 1 fs to about 500 fs. The sensitivity of the DSAM for lifetimes in this time range for heavy recoiling ions is due to several reasons and are listed below.

- The recoiling velocities are generally 3 - 6% of the speed of light, ensuring a large Doppler shift. This ensures that the Doppler shifted peak is distinct from the unshifted peak.

- The stopping powers for ions recoiling into dense backing materials peak at recoiling velocities of $0.03c$ to $0.05c$. DSAM is most sensitive in this energy region for the ions. A very crude estimate of the sensitivity can be found from the relation

$$\Delta\tau = \frac{\nu \Delta E_\gamma}{\beta E_\gamma^0} \tag{2.33}$$

  where ν is the characteristic slowing down time for ions recoiling into the backing material and is of the order of about a few hundred fs, β is the recoil velocity in units of c, E_γ^0 is the unshifted γ ray energy and $\Delta\mathrm{E}_\gamma$ is the smallest measurable Doppler shift. Ge detectors have extremely good resolution. The factor $\Delta E_\gamma / E_\gamma^0$ varies with the energy of the γ ray; we take the factor to be 0.05% for this calculation. Assuming $\beta = 0.04$ and $\nu = 200$ fs, we can expect a sensitivity of about 2.5 fs with a DSAM measurement.

- Nuclear stopping changes both the direction and magnitude of the velocity of the recoiling ions. However, in the realm of dominant electronic stopping, the direction does not change much. There are two advantages due to the dominance of the electronic stopping process. Short lived states at a velocity of $\sim 0.03c$ - $0.05c$ would all decay before they slow down sufficiently for nuclear stopping powers to take effect. This implies that the changes in the mean recoil angle are small during the slowing down period and can be safely neglected, simplifying the data analysis. The second advantage of electronic stopping powers dominating in this velocity range is that they are known far better than the nuclear stopping powers.

- Since the stopping powers for every combination of nuclei have not been measured, one has to interpolate from other measured combinations. Electronic shell effects could be important and could be a cause for errors during the interpolation. The error is smaller at higher velocities and so a reaction in inverse kinematics with a large recoil velocity is more desirable than one in normal kinematics.

Chapter 3

Experimental Details

Levels in ^{19}Ne were populated in the ^{3}He(^{20}Ne,α)^{19}Ne reaction using a 34 MeV ^{20}Ne^{5+} beam from the TRIUMF-ISAC facility. The average current was measured to be 75 nA. The target was ^{3}He implanted in a 12.5 μm thick Au foil, cooled to $\sim -70°$C to prevent diffusion of ^{3}He from the Au target and avoid the buildup of hydrocarbons on the target. γ rays detected in coincidence with α particles were the principal focus of the experiment. The α particles were detected in Si detectors and the γ rays were detected in Ge detectors. The electronics were set up to trigger on a particle in both Si detectors or a $\gamma - \gamma$ coincidence. A scattering chamber was built to ensure the cooling of the target and to hold the Si detectors.

3.1 The Scattering Chamber

The target in the experiment was ^{3}He implanted in Au. The ^{3}He atoms remain implanted in the backing material at room temperature but diffuse out as the temperature rises. The beam power of ^{20}Ne^{5+} of $\sim$ 0.5 Watt causes a temperature rise of $\sim$ 22.5°C in 12.5 μm thick Au foil. The temperature rise is larger in a 12.5 μm Al foil and is $\sim$ 30°C. The calculations detailing the rise of temperature in the target can be found in Appendix A. To prevent the diffusion of ^{3}He from the backing foil, it was important to cool the target. The scattering chamber was designed to ensure effective cooling of the target.

The scattering chamber consisted of two parts: a stainless steel (SS) spider and a cylindrical aluminum chamber. A three dimensional rendering of the chamber and its several parts is seen in Fig. 3.1. On the left panel, scaled diagrams of the SS spider, Al chamber and the Ge detector are shown. The direction of the beam is also labeled on the bottom of the panel. The essential parts of the SS spider and the Al chamber are shown in the right panel. The shroud was aligned inside the SS spider. A liquid nitrogen (LN_2) dewar was mounted on the top flange of the spider. The target ladder was mounted on the bottom flange of the Al chamber. The Be-Cu springs and

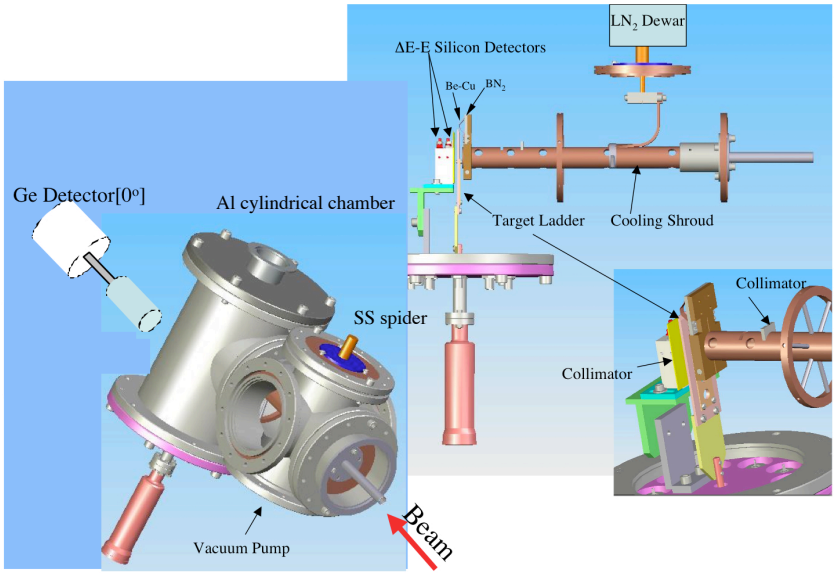

Figure 3.1: A three dimensional rendering of the SS spider, Al cylindrical chamber and the Ge detector is shown on the left panel. The right panel shows the shroud, target ladder and the detector mounts. The bottom right inset illustrates the position of the collimators.

the boron nitride (BN_2) plate are also shown in the right panel. The Si detector mount is also shown in the right panel. The lower right panel shows the position of the collimators. The details of the various parts will be discussed next.

The spider was designed to couple to an existing scattering chamber on one end (shown as the Laval chamber in Fig. 3.2) and to the new Al chamber on the other. The spider also supported the copper shroud that was an integral part of the entire cooling assembly. The entire scattering chamber was differentially pumped through a 1 cm aperture. This aperture was supported by a tube that was attached to one of the flanges of the spider. The tube was 5 cm long and fitted inside the copper shroud. The shroud, made of copper to ensure good thermal conductivity, was 27.5 cm long and had an inner diameter of 2.7 cm. The LN_2 dewar mounted on the top flange

of the spider was attached to a cold finger. The copper shroud was connected to the cold finger via a copper braid. The temperature gradient across the shroud was 330 K/m. The differential pumping and the cooling provided by the shroud were critical to minimize the buildup of hydrocarbons on the target.

The shroud also had two collimators of diameter 3 mm and 4 mm placed at 5.4 cm and 7.4 cm respectively from the target. The current on the collimators was minimized by steering the beam through the apertures of the collimators. The beam spot on the target was less than 2 mm in diameter. The cylindrical Al scattering chamber that coupled to the spider was 15 cm in diameter and 28 cm in height. It held a Cu target ladder and an Al platform. The Cu target ladder rode on a shaft that was coupled through an actuator and had a dial to read out the different target positions. The Al platform was mounted inside the chamber to hold the silicon detectors. The height of the platform could be varied to ensure alignment of the detectors with the beam axis. A detailed scaled sketch of the scattering chamber can be found in Fig. 3.2.

The copper target ladder held three targets. The target frames were squares of side 1.0 cm and were spaced 0.5 cm apart on the ladder. The target ladder was 4 mm away from the end of the shroud. The distance between the shroud and the ladder was critical for the vertical movement of the ladder. An electrically insulating BN_2 plate was mounted at the end of the shroud and two BeCu springs were mounted on the BN_2 plate. These springs made contact with the target ladder as the ladder moved vertically and ensured that the target was cooled. A detailed sketch of the target ladder, the BeCu contacts and the detectors in the Al mount is shown in Fig. 3.3.

The scattering chamber had eight pins on the bottom flange for electrical connections. These pins were used for several purposes.

- Two pins were used to provide high voltage to the two Si detectors and carry their signals to the electronics mounted outside.

- Three pins were used to measure the currents on the two collimators and the target ladder. The current on the collimator was minimized while simultaneously maximizing the current on the target ladder. The current readout from aperture A in Fig. 3.2 was monitored by the accelerator operations group.

- One end of a platinum wire was connected to an electrically grounded pin on the bottom flange of the scattering chamber. The other end

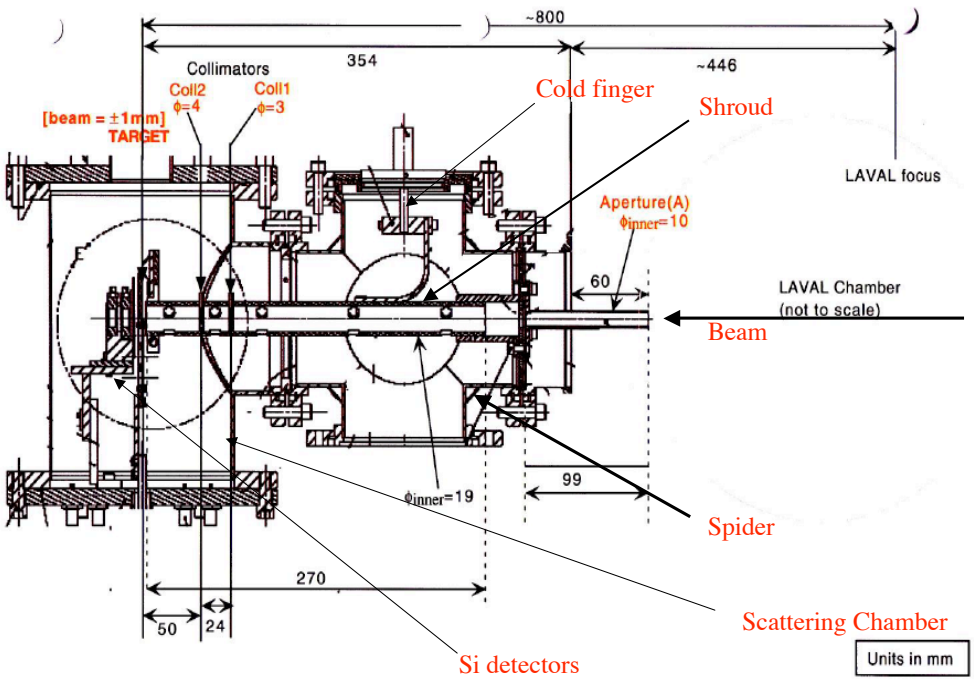

Figure 3.2: The cross sectional side view of the scattering chamber built for the experiment. Details of the various parts are described in the text. The various parts of the scattering chamber and the spider are to scale.

of the wire made contact with the target ladder. The resistance of the platinum wire was read with a multimeter. The resistance of the platinum wire was constantly monitored during the experiment and served as an indicator of the temperature of the target. As the target ladder cooled, the platinum wire cooled as well and the resistance of the wire decreased. Since the temperature dependence of the resistivity of the Pt wire is known, the temperature of the wire was deduced. Details about the calibration can be found in Appendix B.

The cooling of the target ladder was calculated assuming a 100% efficiency for conductive cooling. The details of the calculations of the cooling can be found in Appendix C. It was observed that the target ladder did not cool to below $-2°$C in the previous experiment [32] when the area of contact between the BeCu springs and the target ladder was ~ 0.2 cm^2. The area of contact was increased to improve the overall cooling of the target. Two additional Cu brackets of area ~ 3.7 cm^2 each were attached to the shroud.

The additional Cu brackets are made up of three plates - 2 parallel plates and a third perpendicular to the other two. The two parallel plates have the same width and height but were designed to have different lengths. The entire Cu bracket was mounted on the boron nitride piece by coupling the longer of the parallel plates to the boron nitride piece. The additional copper brackets cool down to the shroud temperature. The shorter parallel plate made contact with the target ladder after the shroud was cold. This plate was designed to be short to ensure that the ladder could move vertically without disturbing the alignment of the shroud and the additional Cu brackets. The position of the shroud relative to the target ladder was optimized so that contact was made only when the shroud was cold and fully retracted. Initially the target ladder was retracted while the shroud cooled. Any hydrocarbons then condensed on the shroud. Once the shroud had reached -105°C, the target was raised to the beam axis. Since the targets were warmer than the shroud, the condensation of residual hydrocarbons occurred preferentially on the colder shroud rather than on the target. The additional Cu brackets however cooled the target ladder and the target to -70°C ensuring that no diffusion of the ^{3}He from the target occurred and reduced the reaction yield. With a beam power of 0.5 Watt, the highest observed temperature on the target was $-58°$C.

The Si charged particle detectors were placed directly behind the target ladder on the platform. An iron plate with a circular aperture of 8 mm and thickness 1.5 mm was placed between the target and the detectors and served to define the angular acceptance of the Si detectors. Two small

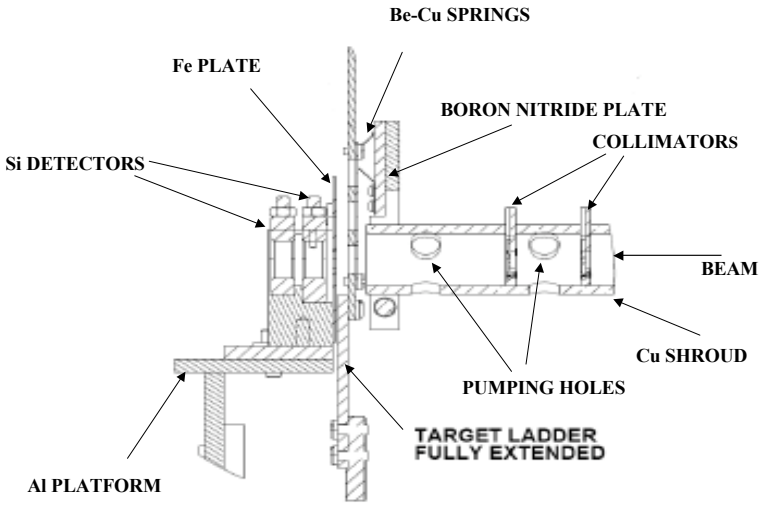

Figure 3.3: A detailed sketch of the area of contact between the target ladder and the cooling shroud. Details of the various parts are described in the text. The figure is to scale.

magnets attached to the iron plate suppressed secondary electrons.

3.2 The Experimental Setup

Two Si detectors and two Ge detectors were used in the experiment. The two Si detectors were 25 μm and 500 μm thick and were used to identify particles by measuring their energy losses ΔE and residual energies E. The surface area of the ΔE detector was 150 mm^2, implying a radius of 7 mm. The distance between the target and the Fe plate was $\sim$12 mm. Since the aperture in the Fe plate was 8 mm, the angular acceptance of the Si detectors was a cone of half angle $\pm 19°$.

Three targets were mounted on the target ladder - one ^{3}He implanted Al foil and two ^{3}He implanted Au foils. The foils measured 1 cm $\times$ 1 cm $\times$ 12.5 μm. 30 keV ^{3}He ions from a Van de Graaff accelerator at the Université de Montréal were implanted into the foils, resulting in a mean implantation depth of 0.1 μm. The number density of ^{3}He was $\sim 6\times10^{17}$ cm^{-2}.

Two 80% high purity germanium detectors were used to detect the γ rays. The detectors were 8 cm in diameter and 12 cm long. The first detector was placed at a distance of 9.5 cm from the target on the beam line and defined a conical angular acceptance of half angle 23°. The setup used during the experiment is shown in Fig. 3.4.

The second detector was oriented perpendicular to the beam axis at a distance of 23 cm from the target. This detector was shielded from the target by a lead brick that was 10.5 cm thick. A 9 kBq ^{88}Y source was placed at a distance of 12 cm from the second detector such that it was about 8 cm from the front face of the first detector and about 16 cm from the chamber. The position of the two Ge detectors and the ^{88}Y source is shown in Fig. 3.4. The scattering chamber is shown along with the two Ge counters. The positions of the weak ^{88}Y source and the Pb brick are also indicated.

Fig. 3.5 is a photograph of the actual experimental set up. The scattering chamber (labeled 'a'), the spider (labeled 'b') as well as the two liquid nitrogen dewars are seen. The dewar on the left corresponds to the Ge detector aligned to the beam axis while the dewar on the right cools the copper shroud via the cold finger.

3.3 The Reaction

The reaction studied in this experiment was ^{3}He(^{20}Ne. This reaction occurred at the front of the foil where the ^{3}He was implanted. The depth of

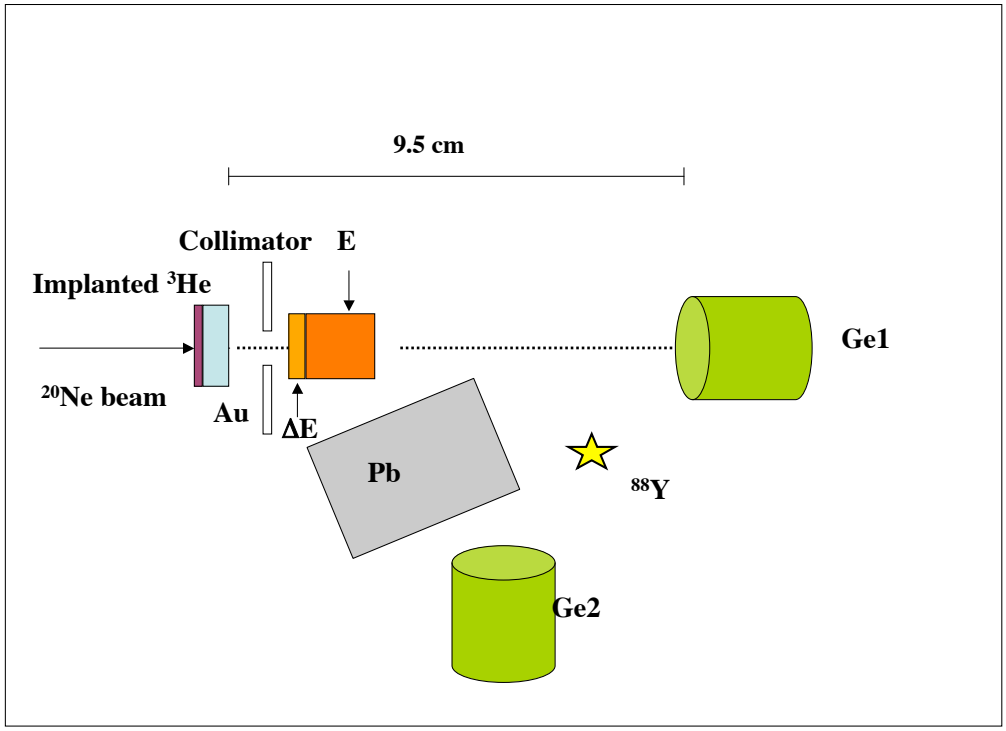

Figure 3.4: (Not to scale) The experimental setup showing the ^{20}Ne beam impinging on a Au foil implanted with ^{3}He, the ΔE and E Si detectors and the Ge detectors.

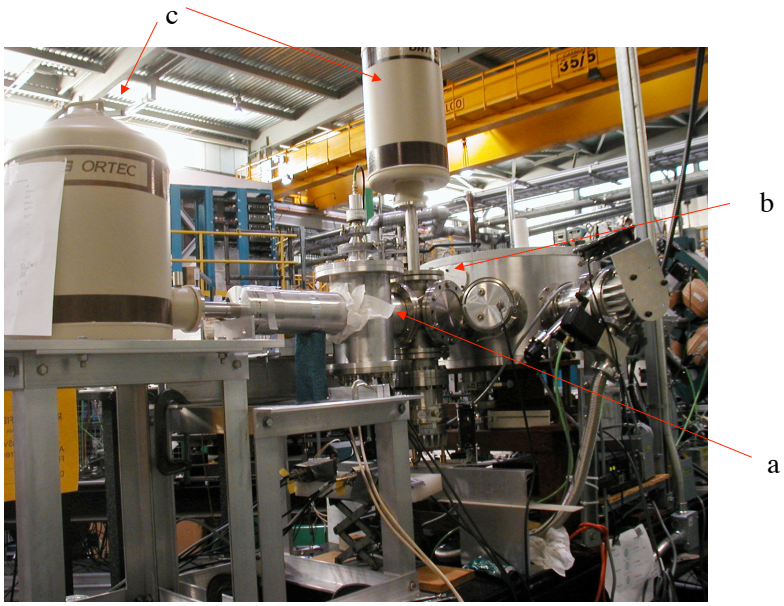

Figure 3.5: The setup during the experiment. The scattering chamber with the targets and the Si detectors is labeled 'a', the spider that supported the shroud is labeled 'b' and the liquid nitrogen dewars are labeled 'c'.

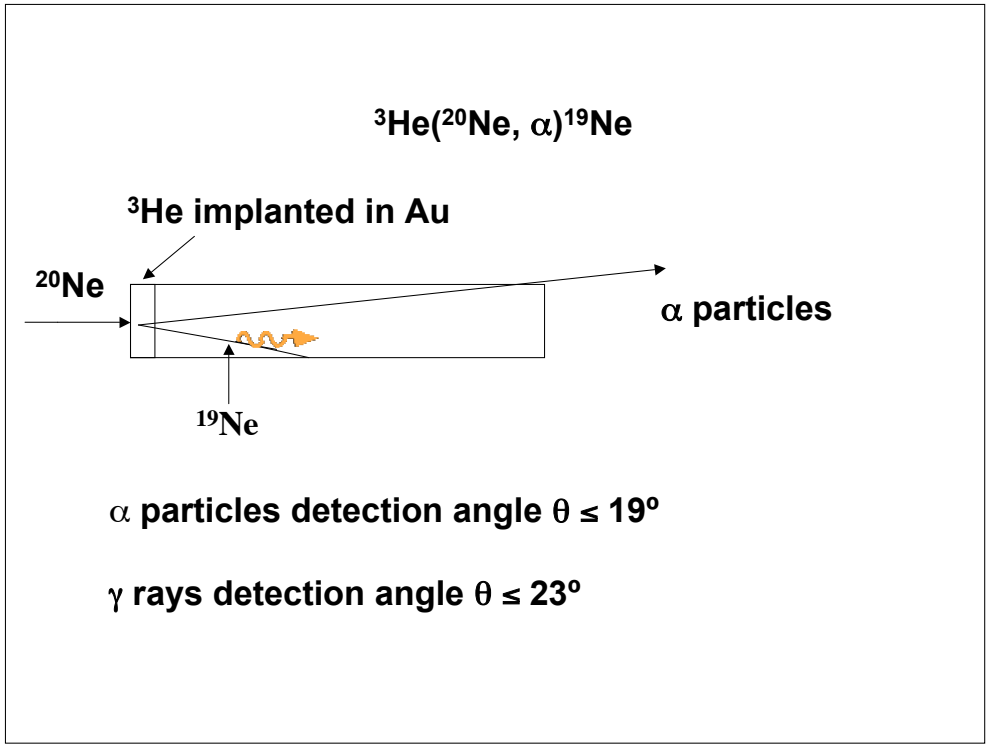

Figure 3.6: Schematic diagram of the reaction.

the implantation was optimized to approximately equal the product of the recoil velocity and the lifetime of the excited state. Since the lifetimes of the states in ^{19}Ne above 3.53 MeV were of order of 10 femtoseconds, most of the Doppler shifted γ rays were observed over a narrow range of the recoiling ^{19}Ne energies.

A schematic diagram of the reaction is shown in Fig. 3.6. Light reaction products such as isotopes of H, He and Li lost some energy in the foil before being detected in the Si detectors. The recoiling ^{19}Ne ions, the ^{20}Ne beam and nuclei with $Z > 3$ were stopped by the foil. The γ rays emitted in the reaction were detected by the Ge detector on the beam axis at a distance of 9.5 cm. These γ rays were subjected to a line shape analysis.

3.4 Detectors

All of the Si and Ge detectors were calibrated with radioactive sources of known energy. The calibration of the detectors is discussed below.

3.4.1 Si Detectors

Light particles were detected in surface barrier Si detectors. Both the detectors were circular, standard ORTEC detectors. The detectors were used in a particle identification telescope geometry, i.e., the E detector was placed directly behind the ΔE. Coincident signals from the two detectors served to identify the particles. The two detectors were independently calibrated with a triple α source. The source consists of ^{239}Pu, ^{241}Am and ^{244}Cm emitting α particles of energies 5.245 MeV, 5.638 MeV and 5.902 MeV respectively.

The thin ΔE detector does not stop 5 MeV α particles. Calculations were done with SRIM [66] to estimate the energy loss of the alpha particles from the source in a 25 μm layer of Si. The calculations are summarized in Table 3.1. The first column in Table 3.1 is the α emitting nucleus and the second column is the energy of the α particle. The third column shows the energy loss of the α particles in 25 μm of Si, as calculated by SRIM [66] and was used for the calibration of the ΔE detector.

The plot of the energy deposited in the ΔE detector *vs* the measured energy loss is shown in Fig. 3.7. The error bars include the straggling of 2.5% for the α particles, as estimated by the SRIM calculations [66]. The straggling was estimated by passing 10000 α particles of the three different energies through 25 μm of Si and fitting the energy spread with a Gaussian.

The thick E detector was then placed in front of the triple α source and calibrated. The 500 μm thick detector stops all the α particles from the source. The width of the α peaks in the E detector was measured to be ∼16.7 keV. This was consistent with the manufacturer's listing of 15.8 keV for α particles with energies of 5 MeV.

The plot of the energy deposited in the E detector *vs* the measured energy is shown in Fig. 3.8. The α particles stop in the Si E detector and the widths of the peaks are reflected in the error bars. The linear calibrations from Figs. 3.7 and 3.8 were used to convert the ADC channels to the ΔE and E energies respectively. The detectors were assumed to be linear beyond the calibration range.

In a particle identification telescope geometry, the kinetic energy of the α particle is distributed between the ΔE and E detectors. The energy lost in the ΔE detector and the residual energy in the E detector were added

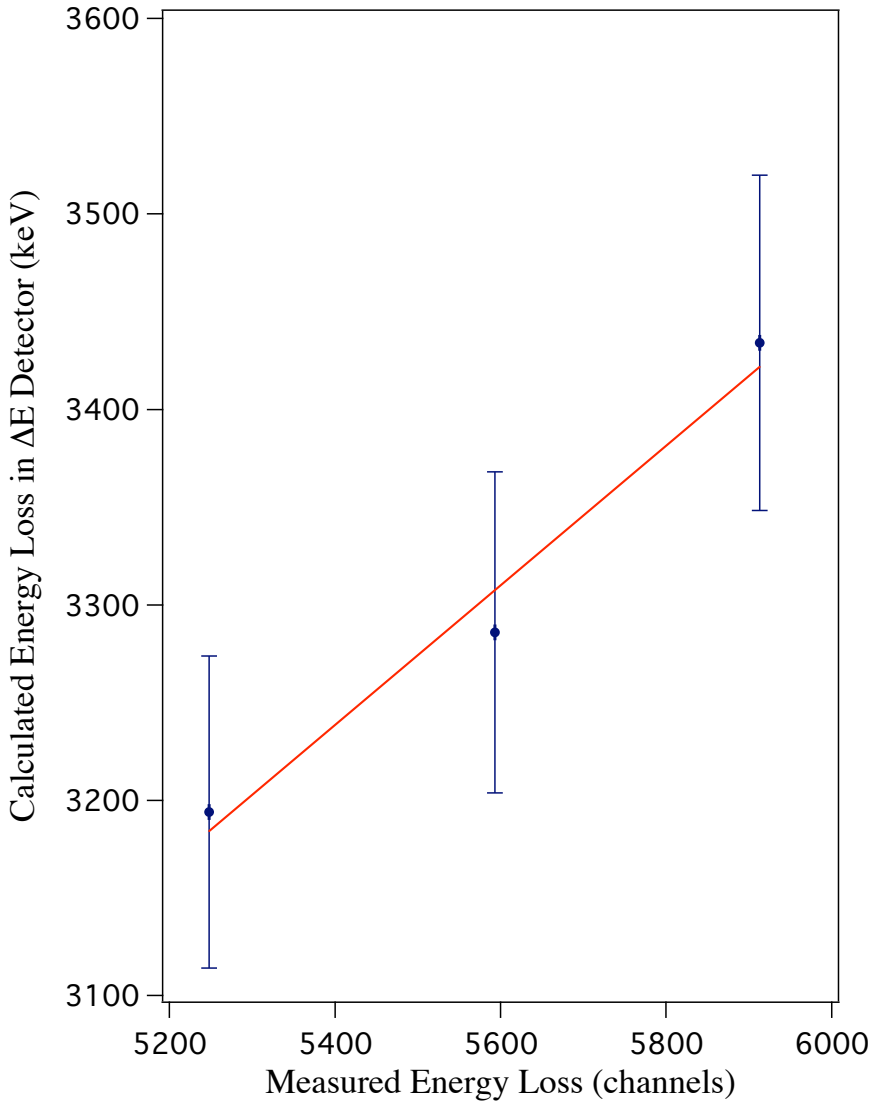

Figure 3.7: Calculated energy loss *vs* the measured energy loss for the ΔE detector along with the best linear fit.

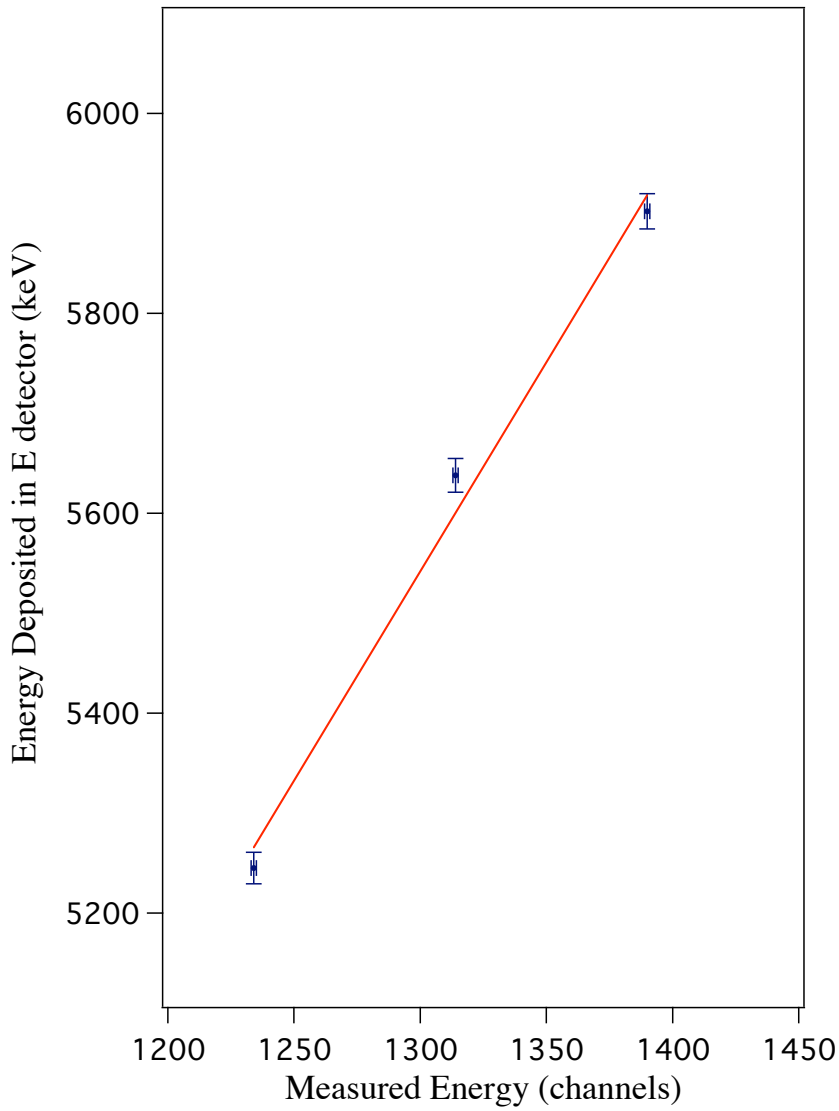

Figure 3.8: Energy deposited *vs* the measured energy for the E detector along with the best linear fit.

α Emitting Nucleus	E_α (MeV)	Energy Deposited in ΔE Detector (MeV)
^{239}Pu	5.245	3.434
^{241}Am	5.638	3.286
^{244}Cm	5.902	3.194

Table 3.1: Energy lost by α particles emitted by the triple α source in 25 μm of Si.

to obtain the kinetic energy of the particles - E_α^{total}. The calibration of the two Si detectors was necessary to define the particle gates and also to apply the kinetic energy E_α^{total} gate. In the reaction studied, the E_α^{total} energy is kinematically correlated with the energy of the recoiling ^{19}Ne ion, which in turn affects the Doppler shift of the γ ray emitted during the reaction.

3.4.2 Ge Detectors

The γ detector aligned to the beam axis was used for line shape analysis. The second detector at an angle of $\sim 90°$ was used as a reference for electronics drift during the course of the experiment and to establish a $\gamma-\gamma$ coincidence. Both the Ge detectors were calibrated with radioactive γ ray sources. The sources used were ^{60}Co and ^{88}Y. The energies of the γ rays from these sources are listed in Table 3.2.

Both the Ge detectors were calibrated with the two sources listed in Table 3.2. The Ge detector aligned with the beam axis was also calibrated with a ^{56}Co source. This procedure was followed to get a realistic description of the intrinsic response of the detector. A detailed description of the intrinsic response can be found in Appendix D. The standard deviation (σ) of the Ge detector for the 3.25 MeV γ ray from ^{56}Co was found to be 1.5 keV.

Fig. 3.9 shows the plot of the photon energy *vs* the measured photon energy for the different sources. The two γ lines from ^{88}Y and ^{60}Co as well as the 3253.42 keV line from ^{56}Co are shown in the plot. The line fitted to the data is also shown. The calibration of the γ detector is based on this linear fit.

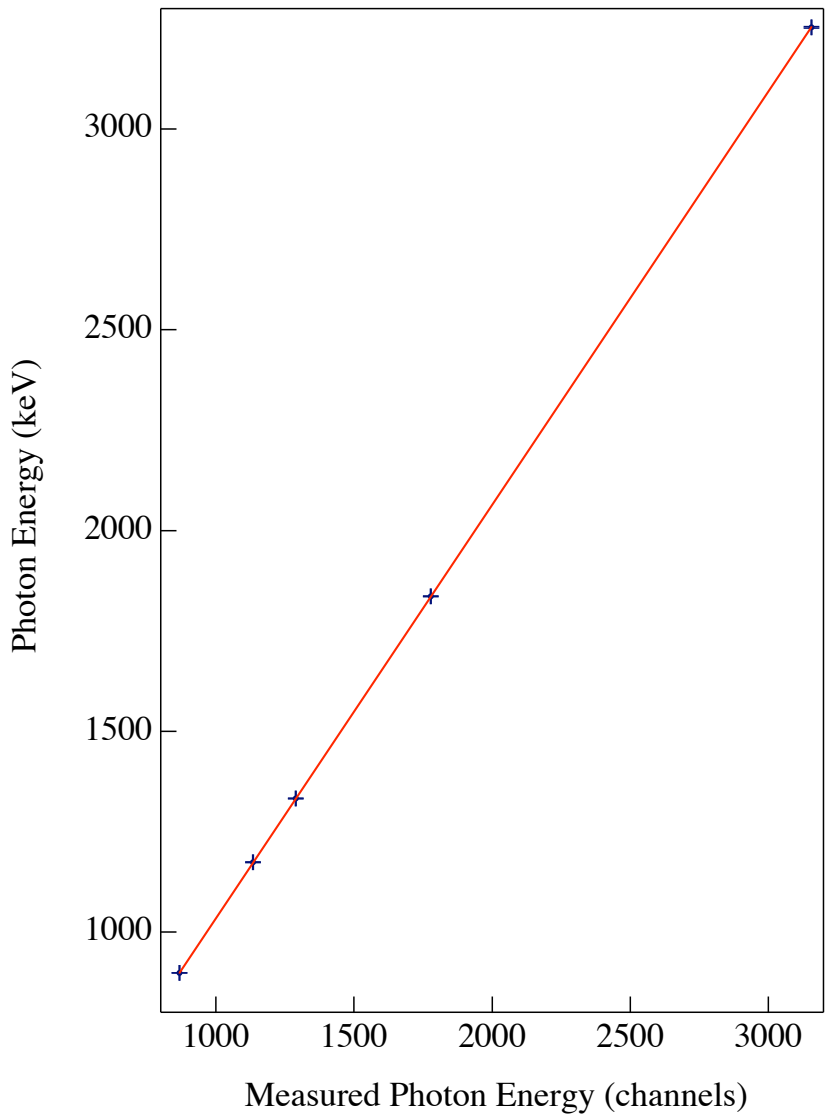

Figure 3.9: Photon energy *vs.* the measured photon energy with a linear fit.

γ Emitting Nucleus	E_γ (keV)
^{88}Y	898
^{60}Co	1173
^{60}Co	1332
^{88}Y	1836

Table 3.2: Energies of γ rays (E_γ) emitted by the radioactive γ ray calibration sources.

The calibrations of the Si and Ge detectors were done before the start of the experiment and also after the experiment ended. The calibrations had not shifted significantly during the course of the experiment.

3.5 Electronics

Preamplifiers coupled the detectors to the electronics and carried the bias voltage to the detectors. The fast and slow outputs from the preamplifiers provided timing and energy information respectively. The fast outputs from the preamplifiers were inputs to Timing Filter Amplifier (TFA) and the energy outputs from the preamplifiers served as inputs to the linear (spectroscopy) amplifiers (LA). The timing signals from the ΔE and E detectors were used to select ΔE - E coincidences. The two strong lines in ^{88}Y at 898 keV and 1836 keV were seen in both the Ge detectors. The timing signals from the two Ge detectors were also used to select γ - γ coincidences. The γ - γ coincidences served to reduce the background in the Ge detectors.

The master trigger was initiated by a ΔE - E coincidence or a γ - γ coincidence. The event rate due to the particle detection (coincidence in the Si detectors) was typically 14 times larger than the $\gamma - \gamma$ coincidence rate. With an event rate of 150 Hz, 10 events per second were due to γ -γ coincidence and the rest were from particle detections.

The γ - α coincidence was established off line. γ rays from the Ge detector aligned parallel to the beam axis that were in coincidence with α particles of the relevant energy were analyzed. The details of this procedure appear in Chapter 4.

The outputs from the TFA modules were used to measure the relative timing of the Si signals. The outputs from the TFA modules were sent to Constant Fraction Discriminators (CFD). The signals from the CFDs of the ΔE and E detectors were then delayed. The delays were initially set with a pulser. The delayed CFD signals were viewed on the oscilloscope and adjusted such that there was maximum overlap between the CFD outputs of the ΔE and E detectors. The delays were fine tuned with the beam prior to data collection.

The delayed signals were sent into a coincidence logic unit that triggered only when both signals were present. This ensured that the signals from both the detectors were in coincidence. The coincident signals from the two detectors were recorded.

Coincidences between the two Ge counters were set up using a second set of TFAs and CFDs. Again the CFD outputs were appropriately delayed and fed into a logic unit that would trigger only when signals from both the Ge counters were present.

The signals from the two coincidence gates discussed above were then fed into a third logic unit which would trigger on an "OR" gate. This meant that the third logic unit would output a signal if at least one of the coincidence gates was present. The final third logic output was used as a master trigger in the electronics. The presence of a master trigger thus implied a coincidence between the Si detectors or between the Ge detectors or both.

The master trigger started the data acquisition (DAQ) system allowing the events to be recorded. The signals from the CFDs of the ΔE and E detectors and the two Ge counters were delayed again to compensate for the latent delay due to the logic units. The delay of the CFD signals was adjusted so that they arrived at the TDC a few nano seconds after the master trigger. The delayed signals were the inputs to the Timing Digital Converter (TDC). The TDC accepted signals after the master trigger arrived at the TDC and registered the relevant events. The information provided by the relative timing of the events was used in the analysis.

One of the outputs of each CFD channel was directly fed to a scaler. The scaler readout was an indicator of the rate in the different detectors. Since elastic scattering was the dominant reaction, the rate in the E detector served as a measure of the concentration of ^{3}He in the target. The scaler

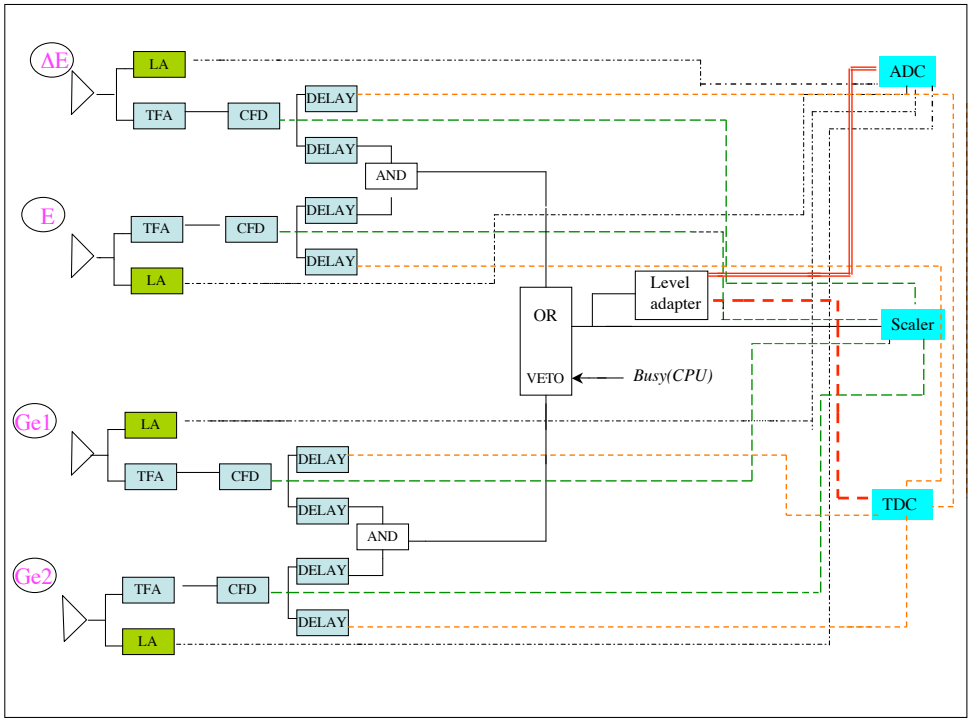

Figure 3.10: A sketch of the electronics used in the experiment.

was monitored during the experiment and was one of the checks done to ensure that everything was working normally.

The LA signals contained information on the energies of the pulse. The amplitudes of the signals were digitized by an Analog to Digital Converter (ADC). The ADC requires a gate to begin converting. The master trigger served as this gate and was delayed sufficiently to arrive just before the signals from the LAs. The delayed master trigger opened the ADC to accept events. The outputs from the four LAs were fed into different channels of the ADC to record the energy from the four detectors. A schematic sketch of the electronics used in the experiment is shown in Fig. 3.10.

The TFAs, LAs, CFDs and logic units were mounted in NIM crates while the ADC, TDC and scalers were in a CAMAC crate. A level adapter module

reversed the polarity of NIM signals and made them compatible with the ADC and TDC. The master trigger was vetoed from accepting more events when the computer was busy.

Chapter 4

Analysis

Individual spectra from the Si ΔE and E detectors as well as the two Ge detectors were built separately, using appropriate calibrations. Coincident detections in the Si ΔE and E detectors are shown in Fig. 4.1. The energy loss ΔE of an ion depends on several factors. For a given stopping material, ΔE varies directly as MZ^2 (where M is the mass of the ion and Z is the proton number) and inversely as the energy E_{total}. The plot of ΔE vs E_{total} would therefore separate the ions according to MZ^2. In Fig. 4.1 the energy loss ΔE is plotted as a function of the residual energy E which is the difference of the total energy and the energy loss, i.e.,

$$E = E_{total} - \Delta E \tag{4.1}$$

It can be seen in Fig. 4.1 that groups with different proton number Z are distinct. However the separation for the two Z=2 isotopes, ^{3}He and α particles is not large since their energy losses scale as their masses. The ratio of the masses of ^{3}He and α particles is 0.75.

In Fig. 4.1, the horizontal locus near the He isotopes (ΔE $\sim$ 2.00 MeV and 1 < E < 8 MeV) have very low statistics. These events are due to the punch through or incomplete deposition of energy by ^{3}He particles.

The α particles correspond to the long curved band in the group labeled He and were concentrated in three groups corresponding to the population of states in ^{19}Ne above 4 MeV, states in the 1.5 MeV region and those that were low lying (0.275 MeV, 0.238 MeV and the ground state). However the energy of the elastically scattered ^{3}He was similar to the energy of α particles corresponding to the population of ^{19}Ne states above 4 MeV. Fig. 4.2 shows the lower region of the ΔE vs E spectrum. The proximity of the elastically scattered ^{3}He and the α particles corresponding to populating the states in the 4 - 5 MeV region in ^{19}Ne is seen clearly in Fig. 4.2. Since the elastic scattering events were many orders of magnitude more numerous than the events of interest, it was important to cleanly separate the elastically scattered ^{3}He from the α particles. An unambiguous α particle gate was created by defining an energy loss discrepancy function.

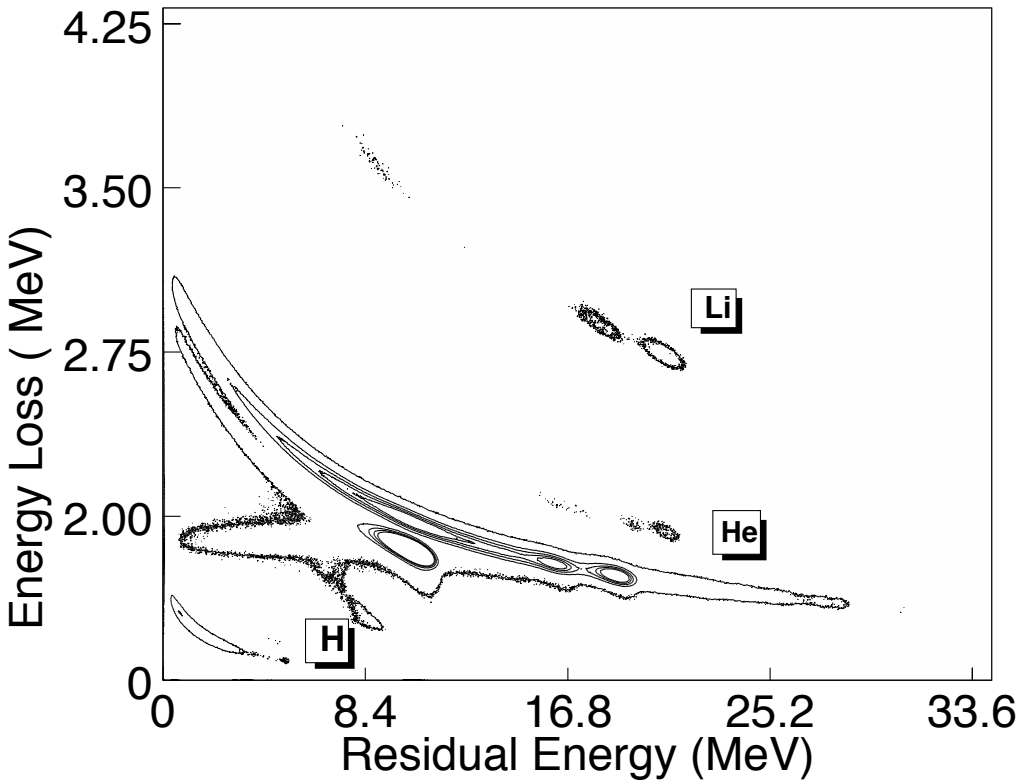

Figure 4.1: ΔE *vs* E: The coincident light particles (isotopes of H, He and Li) detected in both the ΔE and E detectors.

The measured energy losses of α particles ΔE were fitted as a function of the residual energy E. The fitting function was the product of a decaying exponential and a second order polynomial. The coefficients of the polynomial terms and the exponent were varied till a best fit was obtained for the ΔE *vs* E spectrum of the α particles. The coefficients of the functional form were then fixed. The fit is seen in the top panel of Fig. 4.3. The energy loss ΔE is inversely proportional to the total energy E_{total} (as discussed earlier). The bottom panel of Fig. 4.3 shows the variation of the energy loss with the total energy and follows the same pattern as the top panel of the figure. Since the two panels show similar variation of the energy loss, the use of the fitting function to characterize the variation of the energy loss with residual energies is reasonable.

The energy loss discrepancy of a particle was defined as the difference between its measured energy loss and the energy loss calculated with the α particle fitting function. The energy loss discrepancy is thus close to 0 for α particles and finite for all other particle groups. The energy loss discrepancy spectrum is shown in Fig. 4.4. The group of α particles (a) show a discrepancy that is close to zero while the elastic ^{3}He particles (b) show a definite clustering around channel 400. A gate on the energy loss discrepancy that selected only the α particles effectively removed the contribution from elastic scattering. Events with energy loss discrepancies less than -300 channels and greater than 160 channels were filtered out. The events in Fig. 4.1 satisfying the α particle energy loss discrepancy gate are shown in Fig. 4.5.

In our experiment, the energy range of the α particles that correlated with the population of states in the 4 - 5 MeV region in ^{19}Ne is $\sim$ 10 - 17 MeV. Since the α particles lose energy in the 12.5 μm thick Au foil, the energy deposited by the α particles in the two Si detectors ranges from 8 to 15.5 MeV.

The two dimensional ΔE - E plot in Fig. 4.5 shows three groups of α particles. The total energy of the α particles was found by adding the energy loss in the ΔE detector and the residual energy in the E detector. The α particle energy spectrum is shown in Fig. 4.6. The three peaks in Fig. 4.6 correspond to the same three groups seen in Fig. 4.5. Since the α particles and the excited ^{19}Ne ions share the available energy, the excitation of states in ^{19}Ne above the α threshold corresponds to the smaller α particle energy group labeled 'a' in Fig. 4.6. Thus the γ rays emitted from levels in ^{19}Ne above 3.53 MeV were detected in coincidence with α particles with energies beween 8 and 15.5 MeV while the γ rays from the levels in ^{19}Ne around 1.5 MeV were in coincidence with α particle energies between 17 and 19

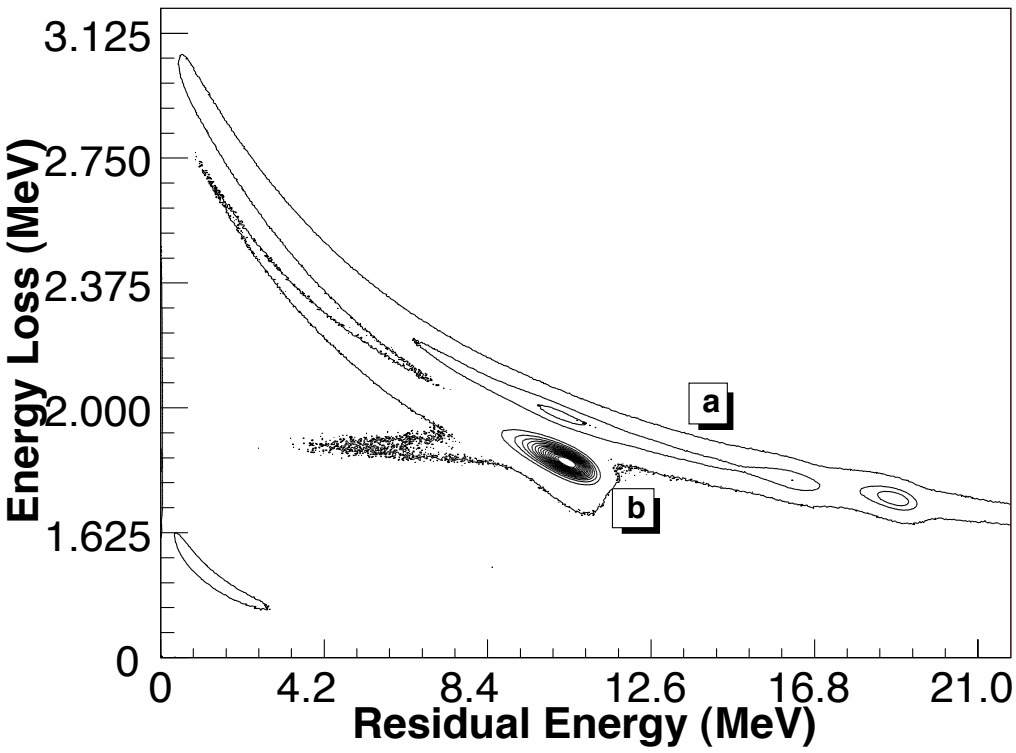

Figure 4.2: Low energy region of the ΔE *vs* E plot showing the proximity of the elastically scattered ^{3}He particles (b) and the α particles (a) correlated with the population of ^{19}Ne states above 4 MeV.

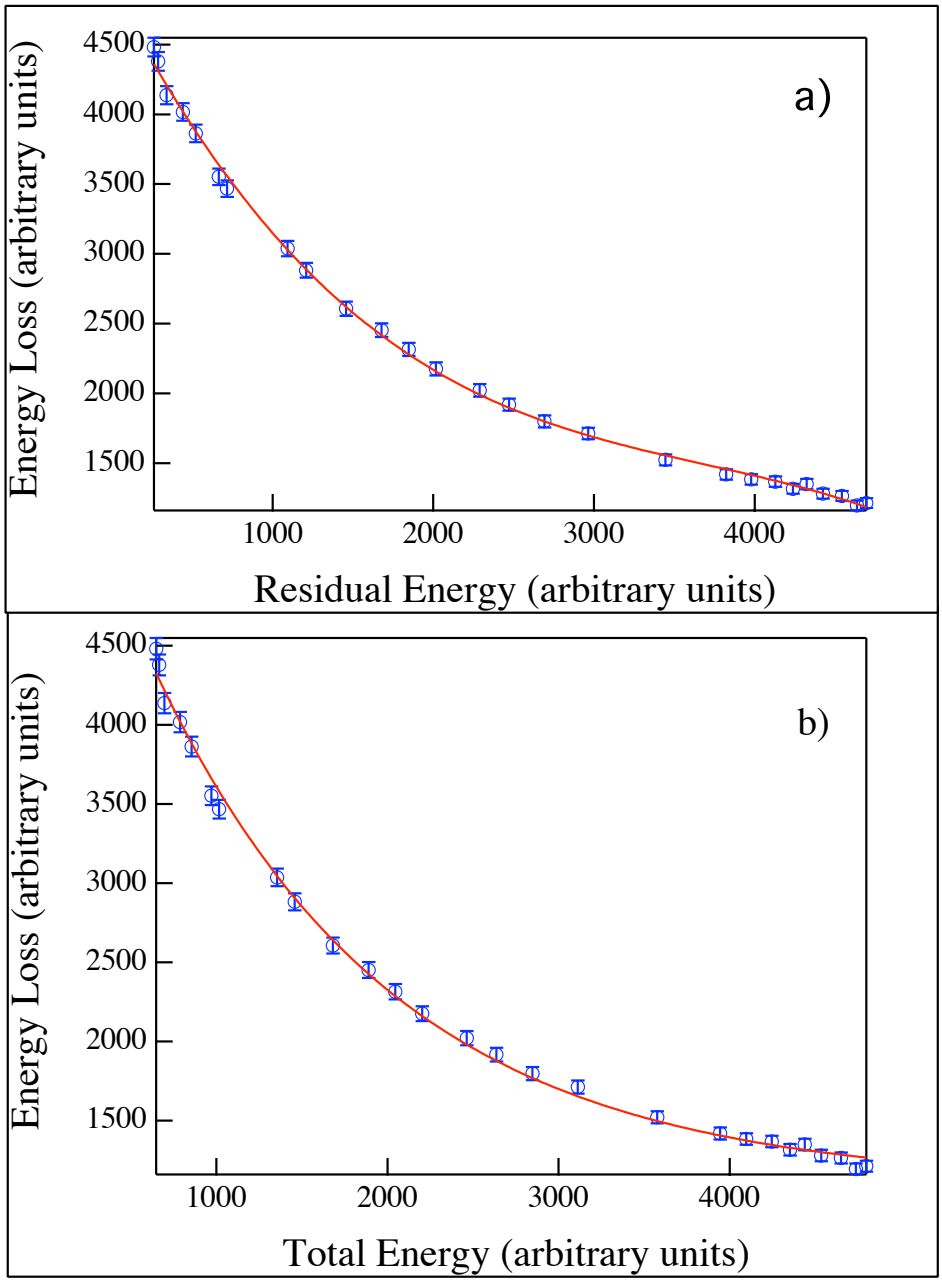

Figure 4.3: The top panel shows the energy loss fitted as a function of residual energies. The bottom panel shows the fit of the energy loss as a function of the total energy.

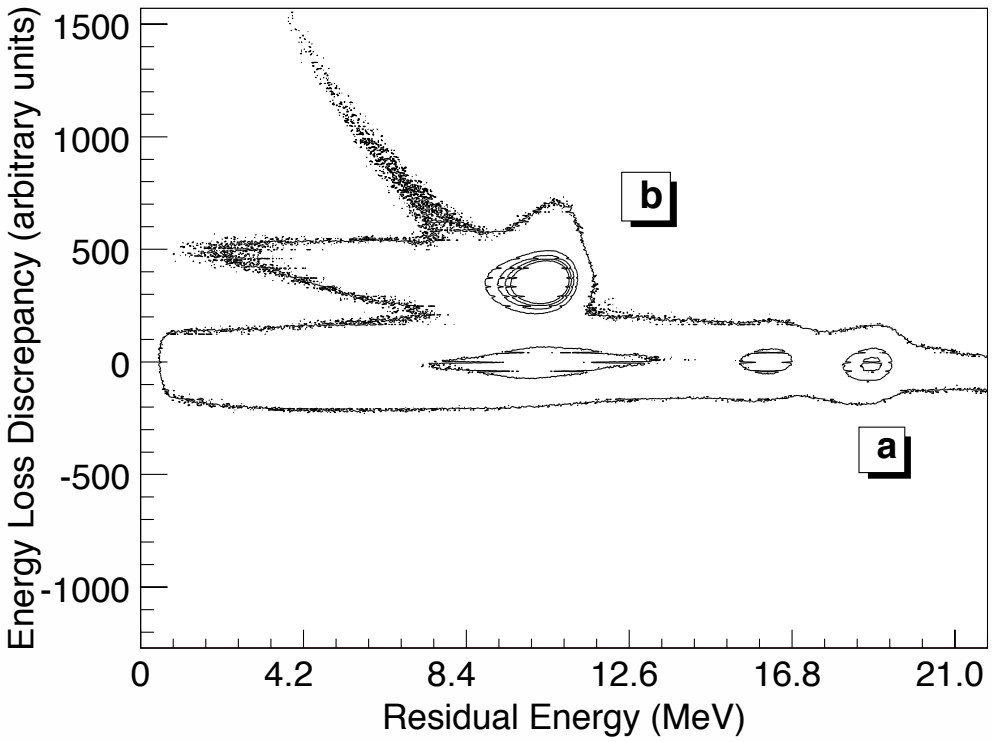

Figure 4.4: The energy loss discrepancy plotted as a function of residual energies. The ^{3}He particles (b) and α particles (a) are seen to be well separated in this plot.

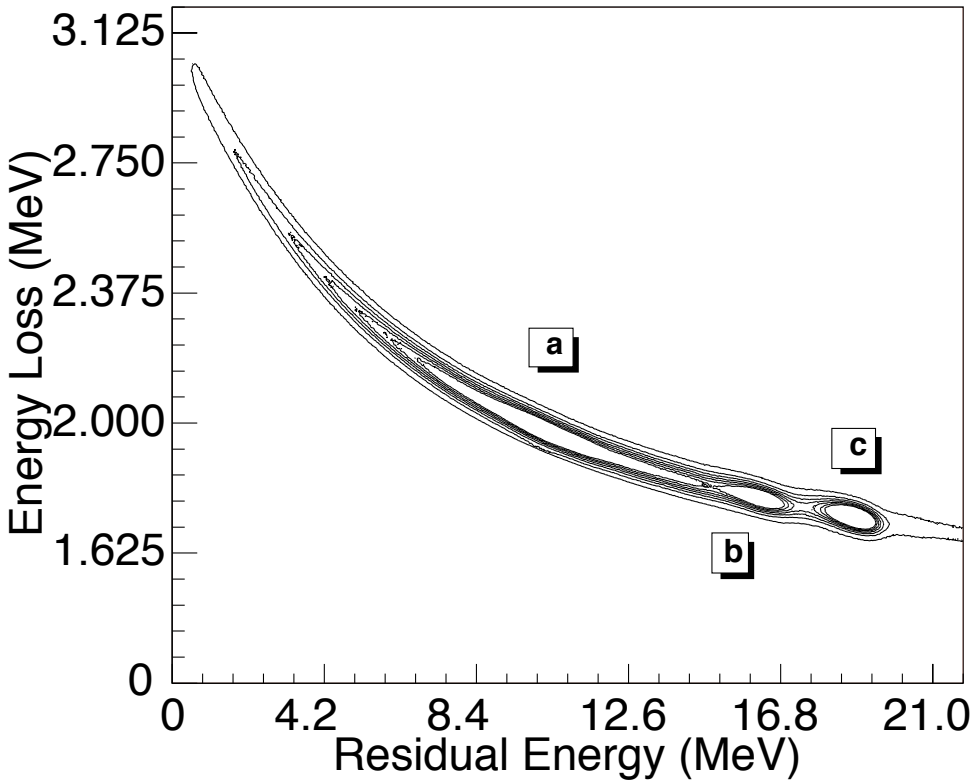

Figure 4.5: ΔE - E coincidence events surviving the α particle energy loss discrepancy test. The three groups of α particles are seen clearly. Group (a) corresponds to states with excitation energies around 4 MeV in ^{19}Ne, group (b) corresponds to ∼1.5 MeV excited states and group (c) corresponds to the ground state and low lying excited states between 0.2-0.3 MeV. A detailed discussion can be found in the text.

MeV. The ground state and the γ rays decaying from the low lying states in ^{19}Ne were seen in coincidence with α particles with energies between 19 and 22 MeV. The small number of events satisfying 22 MeV $< E_\alpha <$ 25 MeV may correspond to the α particles from the reaction of ^{20}Ne on ^{12}C, i.e, the ^{12}C(^{20}Ne,α)^{28}Si reaction.

The calibration constant for the Ge detector aligned to the beam axis was close to 1 keV/channel. This ensured that the γ ray spectrum from this detector was built in bins of $\sim$ 1 keV size. The data were rebinned in three different bin sizes to improve statistics while preserving the visibility of features in the γ spectrum. Bin sizes of 2 keV, 2.5 keV and 3 keV were tried. It was found that a bin size of 2.5 keV was the optimum choice to meet the above mentioned dual requirements of good statistics and satisfactory energy resolution.

A timing gate was defined by examining the events in the TDC spectrum that correspond to the ground state transition of the 4035 keV state. This yielded a prominent peak in the TDC spectrum that was used to set the position and the width of the timing gate. A plot of the TDC spectrum gated with the Doppler shifted γ ray from the 4035 keV state of ^{19}Ne is shown in Fig. 4.7. The strong line at around channel 4000 represents the overflow of the TDC. The events of interest are located at about channel 1500. The inset in Fig. 4.7 shows the structure of the timing gate of interest. For analysis the timing gate was set between 1200 and 1800 channels.

The α particle total energy gate was fine tuned further to enhance the signal to noise ratio. This was done by varying the α total energy cuts in steps of 0.5 MeV in the energy range 8 - 16 MeV. The width of the gate was varied from 2.5 MeV to 3.5 MeV to improve statistics. The signal to noise ratio of the Doppler shifted γ line from the 4035 keV state of ^{19}Ne was calculated for different α energy cuts. The α gate that yielded the highest signal to noise ratio was used for analysis. The range of 11 to 14.5 MeV was found to be optimum for isolating levels above 4 MeV in ^{19}Ne. The α particle energy loss discrepancy gate, the appropriate α particle total energy gate and the timing gate were applied before building the γ spectrum. The gated γ spectrum, shown in Fig. 4.8, reveals several γ rays above 4 MeV from ^{19}Ne. The lines correspond to the decay of the 4035 keV state to the ground state, the decay of the 4378 keV state to the 238 keV state, the two branches of the 4548 keV level (decaying to the 275 keV level and to the ground state) and the decay of the 4602 keV state to the 238 keV state. These lines were not seen if any one of the three gates mentioned above was incorrectly applied. All the γ ray spectra shown in this work resulted from applying these three gates unless otherwise mentioned.

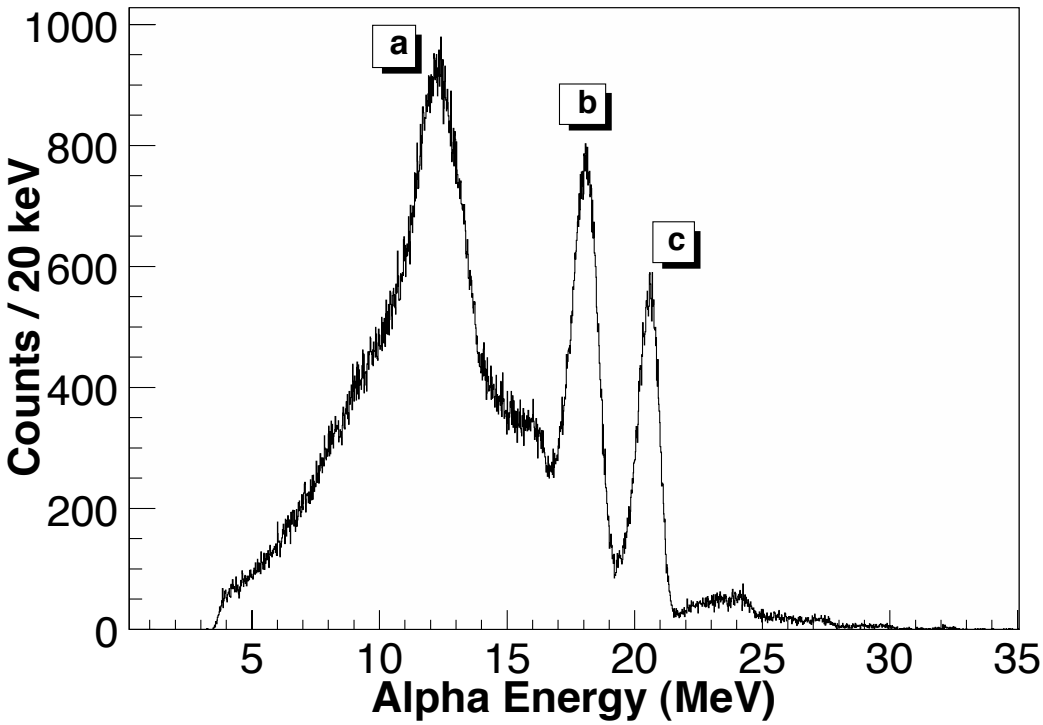

Figure 4.6: α particle total kinetic energy spectrum. The three groups of α particles, as displayed in Fig. 4.5, are seen clearly. The groups (a), (b) and (c) correspond to ^{19}Ne states with excitation energies above 4 MeV, around 1.5 MeV and below 0.3 MeV respectively.

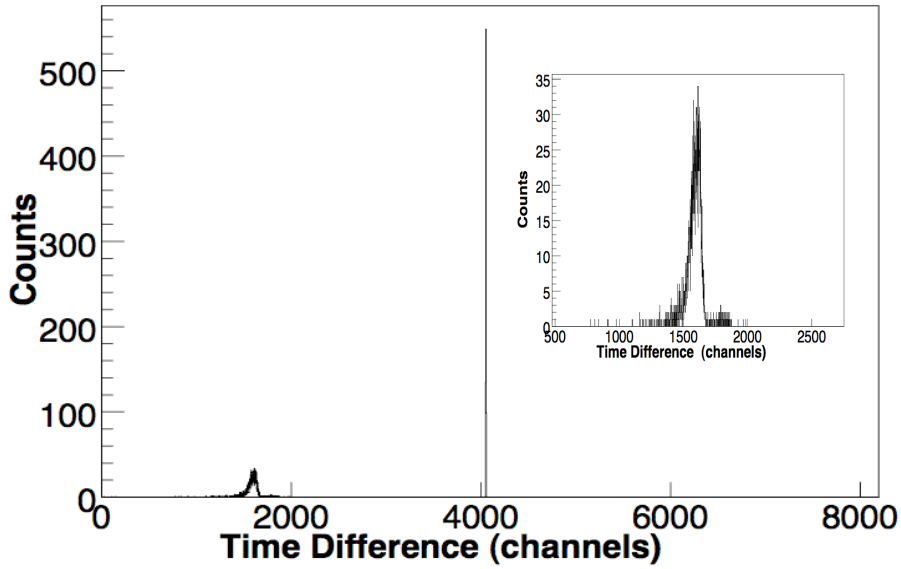

Figure 4.7: TDC spectrum of ground state transitions of the 4035 keV level. An overflow is evident around channel 4000 and the peak of interest is at channel 1500. The inset shows the details of the peak at channel 1500.

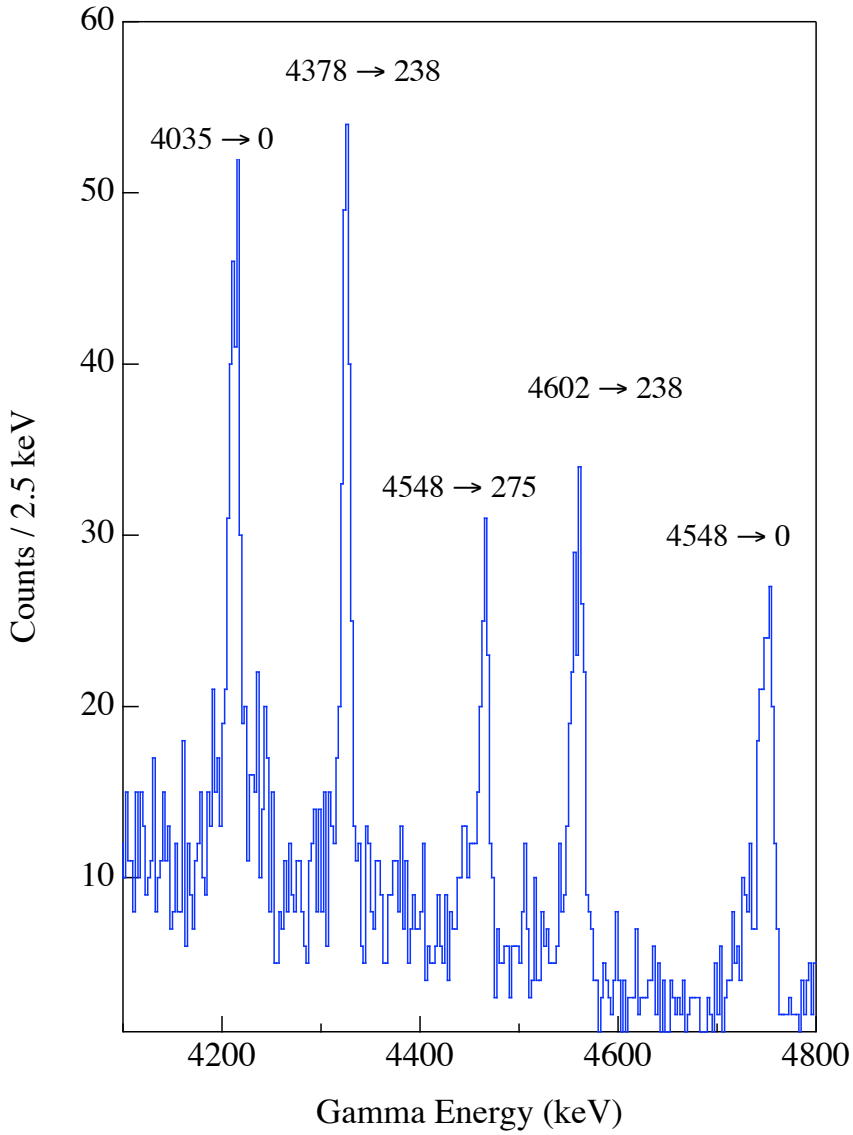

Figure 4.8: Gamma rays within the timing window in coincidence with α particles of energy between 11 and 14.5 MeV. Transitions between states in ^{19}Ne are labeled by the excitation energies of the states in keV.

4.1 Computer Code

A FORTRAN computer code was used to calculate the line shapes corresponding to different lifetimes after incorporating the effects of the stopping power on the kinematically allowed energies of the recoiling ^{19}Ne ions. The calculations take account of the solid angle coverage of the Si and Ge detectors, the intrinsic response of the Ge detector and the angular detection efficiency of the γ rays. The line shape code is described in Ref. [19] and has been tested extensively in several DSAM experiments at Chalk River, Ontario, Canada [1, 5, 33].

The lifetimes studied here are short compared to the nuclear stopping time and hence most of the recoiling nuclei decay almost instantaneously, with little change of velocity. However the entire range of energies allowed by the kinematics and the effects of angular broadening are treated in the code. In Sec. 2.1, the effects of $Q^{'}$ and η^{-1} were discussed in the context of angular broadening. It was important that η^{-1} be small to ensure that recoils were not spread over a large angular region. Table 4.1 summarizes the values of Q$^{'}$ and η^{-1} associated with two levels in ^{19}Ne. In Table 4.1, the 4035 keV and the 4602 keV states in ^{19}Ne are shown in the first column as E$_x$. The value of $Q^{'}$ for the two states is shown in column 2 and the value for η^{-1} is shown in the column 3.

E$_x$ (keV)	$Q^{'}$ (keV)	η^{-1}
4035	-506	0.029
4602	-1073	0.027

Table 4.1: Energies of states in ^{19}Ne, the associated $Q^{'}$ and η^{-1}. Further details appear in the text.

As is clear from Table 4.1, the value of η^{-1} that determines the angular broadening is very small in this experiment. The recoiling ions are almost mono-energetic and unidirectional; however, the admissible variations in energy and angle are treated by the computer code.

γ rays that were identified as transitions from ^{19}Ne states with excitation energies of 4 - 5 MeV were analyzed to extract the lifetimes of the decaying states. Fig. 4.8 shows several lines above 4 MeV which exhibit line shapes associated with short lifetimes. The line shapes of the γ rays arriving in coincidence with α particles of the appropriate energy and within the relevant timing window were analyzed with the DSAM line shape code.

The code requires the excitation energies of the ^{19}Ne levels to calculate the kinematically allowed energies for the α particle and ^{19}Ne ions, the transition energies of the emitted γ rays and the Doppler shifted line shapes. The level energies of ^{19}Ne from Refs. [53, 54] were used to calculate the transition energies. There are seven states in ^{19}Ne above the ^{15}O + α breakup threshold whose γ decays are well established [54]. All seven states are known to be directly fed and no transitions from higher lying states have been reported. The states are the $\frac{3}{2}^+$ state at 4035 keV, the $(\frac{9}{2})^-$ state at 4144 keV, the $(\frac{7}{2})^-$ state at 4200 keV, the $\frac{7}{2}^+$ state at 4378 keV, the $(\frac{1}{2}, \frac{3}{2})^-$ state at 4548 keV, the $(\frac{5}{2})^+$ state at 4602 keV and the $\frac{13}{2}^+$ state at 4634 keV. Doppler shifted lines from all these states have been observed in this experiment.

Besides the transition energies, there are three groups of input parameters to the code. These are the geometry of the experimental setup, the stopping power of the recoiling ions in the target foil and the detector response parameters.

The reaction kinematics and the geometry of the experimental setup dictate the maximum velocity of the recoiling ions and the angular acceptance of the detectors. The angular acceptance of the detectors is defined by the placement of the detectors during the experiment, characterizing the maximum angle at which the α particle and the γ ray can be detected in their respective detectors. The maximum velocities of the ^{19}Ne recoils were calculated using the kinematics of the reaction after incorporating the appropriate solid angle for the Si and Ge detectors.

The stopping power of ions in matter provides the most important ancillary input to any DSAM measurement [58]. Our computer code offers the flexibility of choosing different stopping powers for the recoiling ion in the target foil. The computer code SRIM [66] is used widely for calculating the stopping power. As shown in Ref. [31], the stopping powers calculated with SRIM differ by 5 -10% from the experimentally measured stopping powers for most ions passing through Au in the energy region of our interest. An empirical parameterization of experimental data on the stopping powers of Ne ions in Au in the energy region of interest exists [20]. The empirical

stopping powers from Ref. [20] were compared with the SRIM calculations. The difference in the stopping powers due to the empirical and the SRIM calculations can be seen in Fig. 4.9. The incident energy is plotted as the abscissa in Fig. 4.9. The ordinate of Fig. 4.9 is the ratio of the difference between the empirical stopping power and the SRIM calculations to the empirical stopping power and is expressed as a percentage. Since the SRIM stopping powers are smaller, the choice of stopping powers from Ref. [66] would systematically increase the extracted lifetimes.

Another feature of the line shape code is the possibility of using a two foil approach to account for the ^{3}He implanted region. Though ^{3}He is implanted to a very small depth in the Au foil, the implantation itself causes the ^{3}He + Au layer to swell, increasing its thickness and reducing its density. This results in a change of the stopping power in the implanted region. Following the prescription in Ref. [2], the effect of this swelling was incorporated into the calculation of the lifetimes. In addition to the energy loss of the ^{20}Ne beam in the front layer of pure Au, the energy losses of the recoiling ^{19}Ne in the swollen layer of ^{3}He and Au and then in the pure Au layer were taken into account in the line shape analysis. The details of the two foil approach can be found in Appendix E.

The response of the Ge detector is represented in the third group of input parameters to the code. The detection efficiency as a function of angle and the intrinsic response of the Ge detector are both required. The position of the Ge detector determines its geometric efficiency. The geometric efficiency was weighted by the quantum efficiency of detecting γ rays of a particular energy. The volume of the detector, its geometry and the energy of the incident γ ray play a large role in determining the overall detection efficiency. The absolute efficiencies of the Ge detector are not required by the code. Only the relative efficiency is needed to incorporate the variation of the γ efficiency with the angle of detection. The detection efficiency of the detector for 2 MeV and 4 MeV γ rays emitted isotropically was simulated using a GEANT4 Monte Carlo simulation [25]. The geometry of the detector is discussed in Appendix F.

The line shapes predicted for different lifetimes were used in conjunction with a constant background to fit the γ-ray spectrum.A linear background was also tried, but did not appreciably improve the fits or alter the lifetimes. The lifetimes,the background and the amplitude of the Doppler shifted γ ray line were varied to obtain the best fit by χ^2 minimization.

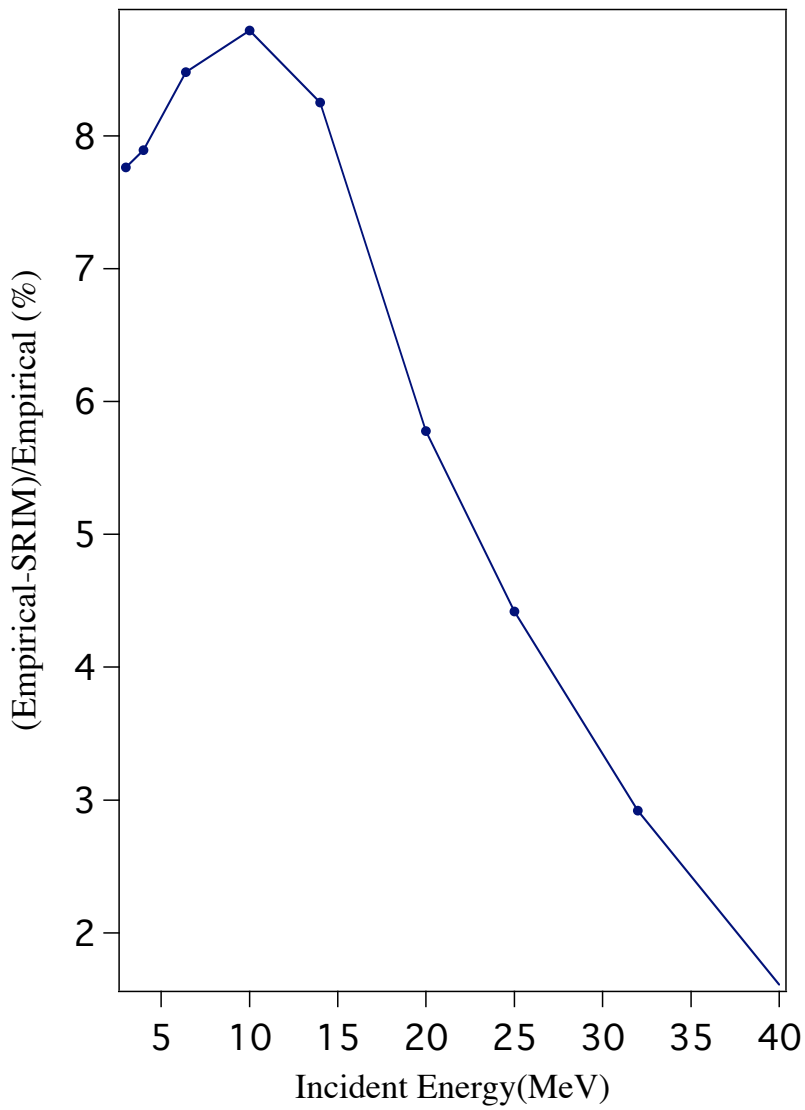

Figure 4.9: The stopping powers of ^{19}Ne in 12.5 μm of Au were calculated using SRIM. The difference of the SRIM calculations from the empirical stopping powers plotted as a function of the incident energy. The line is drawn to guide the eye.

4.2 Systematic Errors

Several sources of systematic error in the measured lifetimes were considered. The sources of possible errors considered were - the stopping power, the distribution of the ^{3}He ions in Au, the beam energy, the transition energies, the intrinsic response, possible misalignments and calibration drifts of the Ge detectors and anisotropic emission of γ rays. The main sources of error were due to the stopping power, the ^{3}He distribution and the beam energy and will be discussed below.

4.2.1 Stopping Power

The authors of Ref. [20] assigned a $\pm 4\%$ error on the measured stopping powers. Therefore the stopping power was varied by $\pm 4\%$ and the data were fitted with the line shapes recalculated with the new stopping power. The lifetimes were extracted by the χ^2 minimization, as described above. The error on the lifetimes due to the stopping power varied with the transitions and was in the range of 4 - 12%.

The interplay of the stopping power and the lifetime in the observed line shape is best summarized in the first term of Eq. 2.28. The stopping power coefficient K_e enters the expression in ζ. The factor ζ/τ appears as the coefficient of N_0 as well as in the exponent. A shorter lifetime shows larger sensitivity to the change of the stopping power, while a longer lifetime is less sensitive to the variations of the stopping power.

4.2.2 Reaction Vertex Depth

The target was made by implanting 30 keV ^{3}He ions on a 12.5 μm thick Au foil. Using SRIM [66], we simulated the passage of 10000 ^{3}He ions at 30 keV through a 12.5 μm Au foil. The range of the ions was then fitted with a Gaussian to characterize the centroid as well as the width of the ^{3}He distribution. It was found that the centroid was at 0.07 μm and the standard deviation was 0.06 μm. The range calculations from SRIM and the Gaussian fit are shown in Fig. 4.10.

Using 1σ values for the depth, there was a 68% chance that the reaction occurred anywhere from 0.01 μm to 0.13 μm. Since the ^{20}Ne beam could interact with the ^{3}He in this range of the distribution, it was important to account for the effect of the reaction vertex depth. If the reaction of interest occurred at the beginning of the ^{3}He distribution, the incident energy was 34 MeV. If however the reaction occurred elsewhere in the ^{3}He distribution,

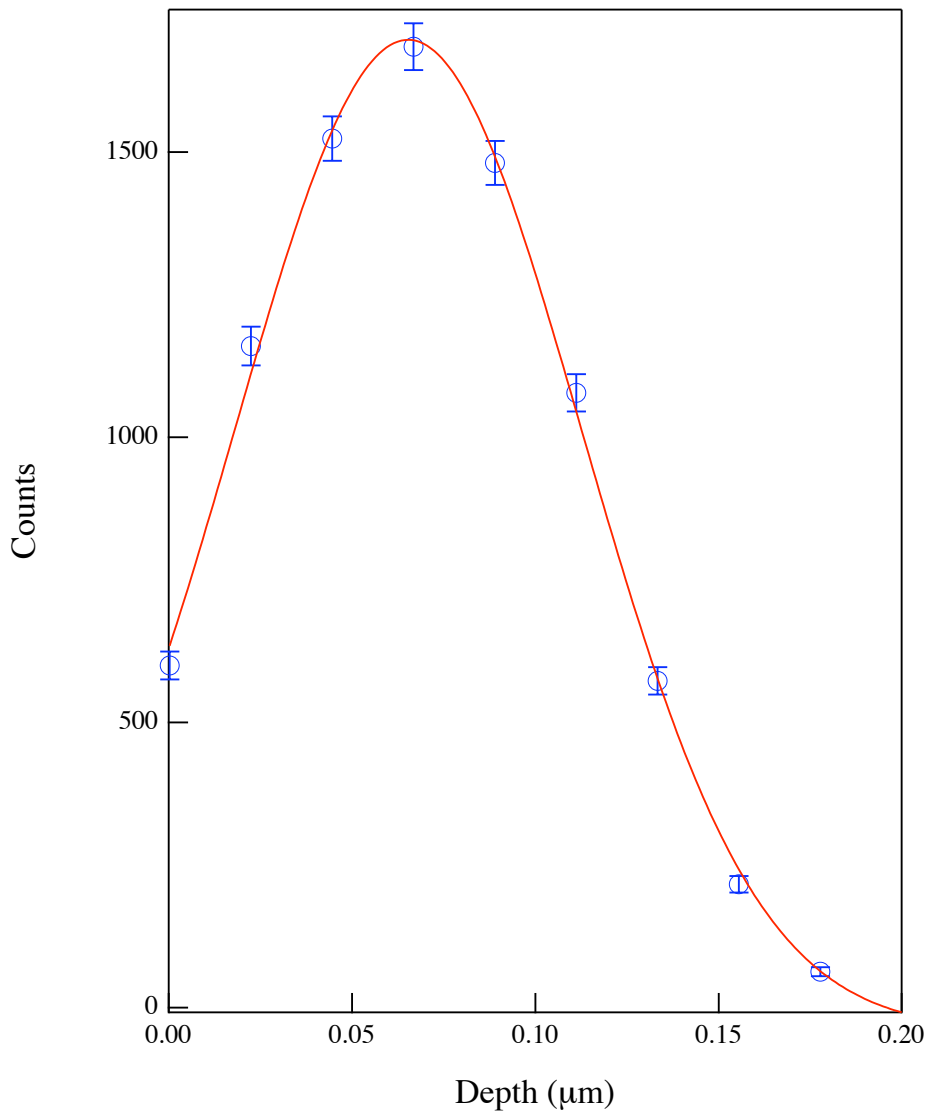

Figure 4.10: The range of 30 keV ^{3}He in 12.5 μm of Au is shown. Also shown is a Gaussian fit with a centroid of 0.07 μm and a standard deviation of 0.06 μm.

say, at 0.07 μm, the beam energy had to be corrected for energy loss in 0.07 μm of the implanted region. The energy loss would change the energy of the ^{20}Ne ions that participate in the reaction, affecting the energy of the recoiling ^{19}Ne ions and hence the Doppler shifted γ rays. The energy of the beam at the beginning of the foil, at the centroid of the ^{3}He distribution (0.07 μm) and at 0.13 μm were used to calculate the Doppler shifted line shapes for the different transitions. It was found that the effect of the reaction vertex depth was different for different lifetimes. The maximum effect was seen for the short lived state at 4378 keV.

The transition for the 4378 keV $\rightarrow$ 238 keV was fitted with a one foil approach as well. The stopping power of ^{19}Ne in just the Au foil was used to calculate the line shapes corresponding to different lifetimes. It was found that an one foil approach yielded a higher lifetime than the lifetime extracted from the two foil approach. For the short lived state, the difference was 15%.

4.2.3 Beam Energy

There were two different effects that contributed to the uncertainty of the beam energy. The effects are specified at the 1σ level. The uncertainty in the centroid of the beam energy was $\pm$ 0.1%. The spread of the beam energy was $\pm$ 0.2%. Adding the two effects in quadrature, the uncertainty in the beam energy was $\pm$ 0.2% at the 1σ level. All the transitions were refitted to estimate the effect of the beam energy variation. The range of the variation of the lifetimes was found to be 0-11%. The long lived transition of the 4200 keV state showed no sensitivity while the short lived transition from the 4378 keV state showed the maximum difference of 11%.

The effects of the other factors listed above were also examined. The effect of the uncertainties of the transition energies was investigated. While the centroid shift affected the χ^2 marginally, the lifetime corresponding to the minimum χ^2 did not change. We found that the lifetimes were not affected by the small uncertainties associated with the transition energies or the emitted γ ray energies.

In Appendix D, the values of the parameters β and σ characterizing the intrinsic response are listed along with the associated errors. The line shape calculations need an intrinsic response for the Ge detector; the central values of the β and σ parameters were extrapolated to the energy of interest and used to define the intrinsic response of the detector. The parameters were varied within the errors quoted and their effect on the lifetimes probed. The lifetimes that fit the data did not vary with the variation of the parameters β and σ.

Care was taken to align the Ge detector to the beam axis. The errors associated with the measuring tools (vernier calipers and the ruler) were used to calculate the maximum admissible misalignment of the Ge detector. The maximum angle by which the Ge detector could have been misaligned was found to be $\pm 1°$. The misalignment affected the angular range of the Ge detector, changing it from $\pm 23°$ to either -22° to +24° or -24° to +22°. Calculations with the misaligned Ge detector did not alter the lifetime of the transitions, although the fits (χ^2) altered in some cases.

The γ rays from ^{88}Y were monitored through the run. It was found that the 1836 keV line from ^{88}Y drifted slightly. The drift was diurnal and could be fitted with a Gaussian that had a standard deviation of 140 eV. This was very small compared to the resolution of the Ge detector, which was of the order of 1.5 keV for a 3.253 MeV γ ray. Hence the calibration drifts of the Ge detector did not affect the position of the peaks and the associated lifetimes.

The line shape code allowed the choice of an anisotropic angular distribution for the γ rays. Dipole and quadrupole angular distributions for the emission of the γ rays were tried and the line shapes were extracted. The choice of anisotropic angular distributions had no effect on the lifetimes.

The results of the systematic error analysis are summarized in Table 4.2. The first column lists the excitation energies of the ^{19}Ne levels (E_x) and the second column is the energy of the emitted γ ray (E_γ). The next four columns list the systematic errors that were obtained for the different transitions at the 1σ level and are listed as percentages of the measured lifetime. The third column is the error due to the stopping power, the fourth is due to the uncertainty associated with the reaction vertex and the fifth column lists the errors observed due to the beam energy uncertainty. These three main sources of error (stopping power, reaction vertex depth and the beam energy) that contributed to the systematic errors were added in quadrature. The total systematic uncertainty in the lifetimes measured here is listed in the sixth column and ranged from $\pm 4\%$ - $\pm 19\%$.

E_x (keV)	E_γ (keV)	Errors due to Stopping Power (±%)	Reaction Vertex Depth (±%)	Beam Energy (±%)	Total (±%)
4035	4035	4.30	2.80	7.04	8.71
4035	2499	4.69	6.25	6.06	9.89
4144	2636	4.40	2.20	7.14	8.67
4200	2693	4.00	0.00	0.00	4.00
4378	4140	11.50	10.36	11.10	19.05
4548	4548	3.92	6.75	8.50	11.55
4548	4273	3.40	3.00	8.54	9.67
4602	4364	4.25	7.00	7.89	11.37

Table 4.2: Systematic errors associated with the transitions studied in the experiment.

Chapter 5

Results

This chapter discusses the line shape analysis of transitions from seven states in ^{19}Ne above 3.53 MeV. Fig. 5.1 shows the levels in ^{19}Ne that were populated in the experiment. The γ ray transitions of interest are also shown. The line shapes of the Doppler shifted γ rays from different transitions were analyzed to extract lifetimes. The data were fitted with a background and the line shape corresponding to a lifetime. The best fit was determined by the minimization of χ^2.

For N data points (x,y), fitted by the functional form f(x), χ^2 is defined as

$$\chi^2 = \sum_{i=1}^{N} \frac{(f(x_i) - y_i)^2}{y_i} \tag{5.1}$$

The lifetime of the observed transition was the value used in the fit that yielded the minimum χ^2. Since the χ^2 fit was obtained by varying the lifetime, the background and the normalization, for N data points there are N - 3 degrees of freedom. The reduced χ^2 (χ^2_{red}) was calculated by dividing the total χ^2 obtained from the fit by N-3.

All errors in this chapter are specified at the 1σ level unless mentioned otherwise. The generally asymmetric statistical errors are shown as superscript and subscript; the symmetric systematic errors follow the statistical errors.

Besides the γ rays from ^{19}Ne, γ rays from states in ^{197}Au were also observed. These γ rays were observed due to the Coulomb excitation of ^{197}Au (coulex lines). One of the coulex lines seen in this experiment has been reported only in polarized deuteron scattering experiments [48, 65].

5.1 The state at 1536 keV

The input parameters to the line shape code were verified by extracting the lifetime of the well measured state at 1536 keV. The transition of the 1536 keV state to the 238 keV state is seen in Fig. 5.2 along with the best fitting

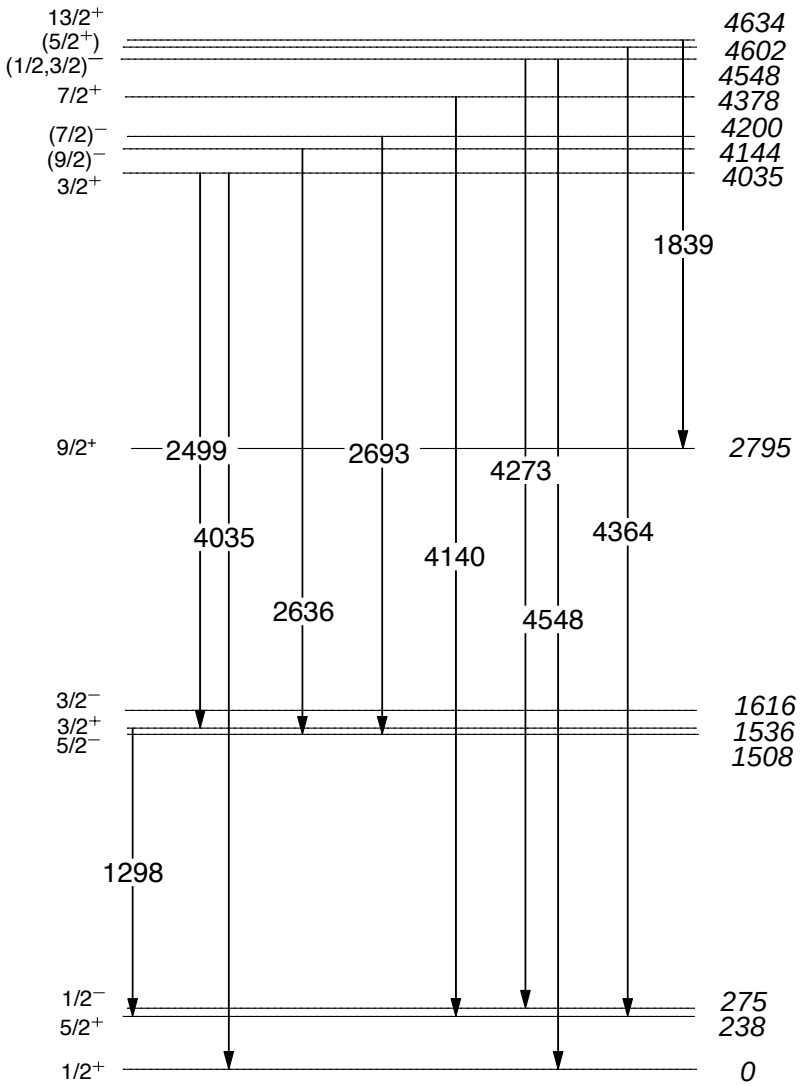

Figure 5.1: Transitions of states in ^{19}Ne studied in this experiment. The energy levels are labeled by their spins, parities and excitation energies in keV.

line shape corresponding to a lifetime of 19.1 fs. The lifetime of $19.1^{+0.7}_{-0.6}\pm1.1$ fs agrees well with earlier reported measurements [53, 54].

5.2 The state at 4035 keV

This state is predicted to contribute dominantly to the initial breakout from the hot CNO cycles [18]. It has three branches [17, 54] - an 80±15% branch to the ground state, a 15±5% branch to the level at 1536 keV and a 5±5% branch to the level at 275 keV. Two branches of this state were observed in this experiment.

5.2.1 The 80% Branch

In Fig. 4.8, the Doppler shifted transition from the 4035 keV state to the ground state appears along with other γ rays corresponding to the de-excitation of higher lying levels. The transition was isolated and subjected to a line shape analysis. The best fitting line shape is shown along with the data in the top panel of Fig. 5.3. The fit describes the data well and represents a line shape corresponding to 7.1 fs. The lifetime of this state was found to be $7.1^{+1,9}_{-1.9}\pm0.6$ fs, consistent with the measurements reported earlier - 13^{+9}_{-6} fs from Ref. [53] and 11^{+4}_{-3} fs from Ref. [32].

Fig. 5.3(b) shows the second transition of the 4035 keV level, which will be discussed next. The values of the reduced χ^2 for the two fits are included in the figure caption.

5.2.2 The 15% Branch

This is the first time that the second branch of the 4035 keV state has been observed in lifetime studies. From kinematics, the transition was expected to be seen with an α particle energy (E_α) between 11 MeV and 14.5 MeV - the gate that corresponds to the excitation of the 4035 keV level. The second, weaker branch of the 4035 keV level was identified and analyzed. The peak at 2608 keV in Fig. 5.4 is attributed to the Doppler shifted transition from the 4035 keV level to the 1536 keV level. This γ ray is not seen with E_α gates outside the range given above.

The energy of this γ ray transition is lower than the 80% branch of the 4035 keV level. Hence the background is considerably higher than the background of the 80% branch observed at 4212 keV. The data and the best fitting line shape corresponding to 6.6 fs are shown in the bottom panel of Fig. 5.3. The lifetime is consistent with that deduced from the stronger

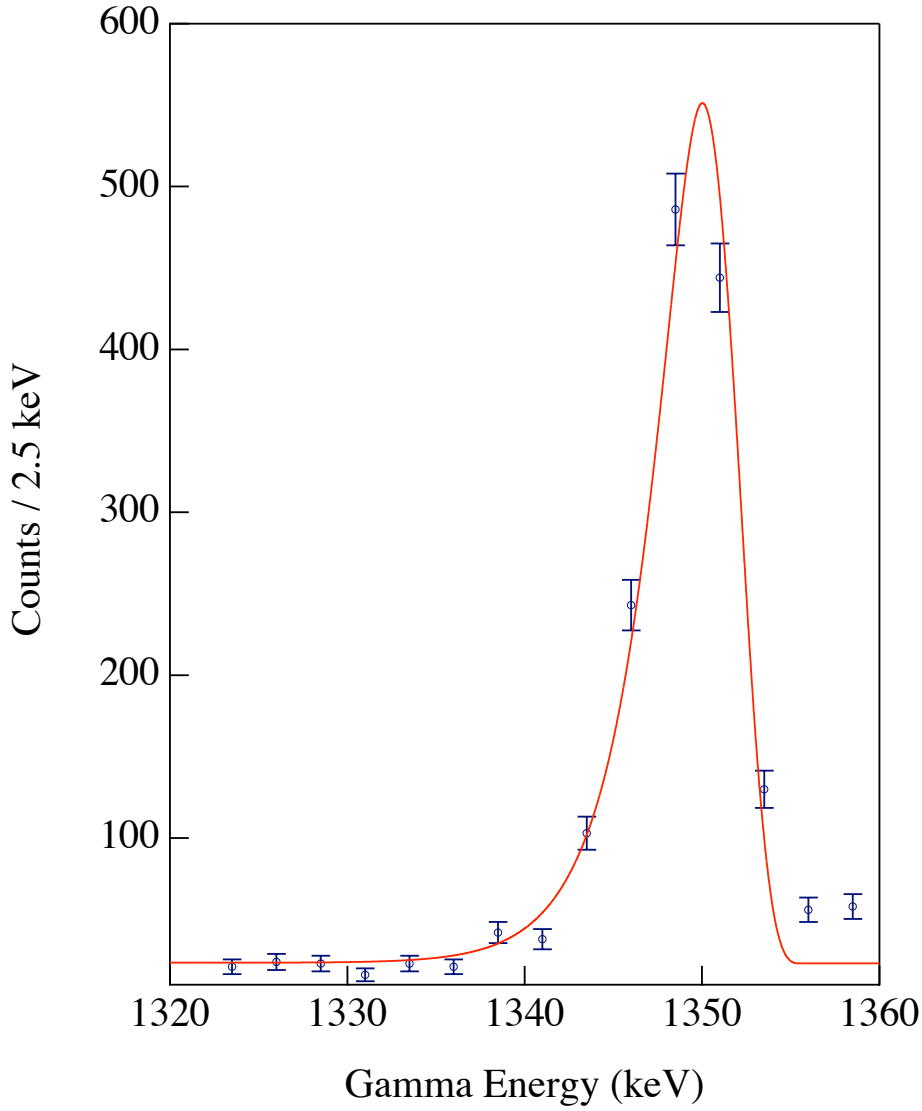

Figure 5.2: The transition due to the 1536 keV level. The lifetime of this state was determined to be $19.1^{+0.7}_{-0.6} \pm 1.1$ fs.

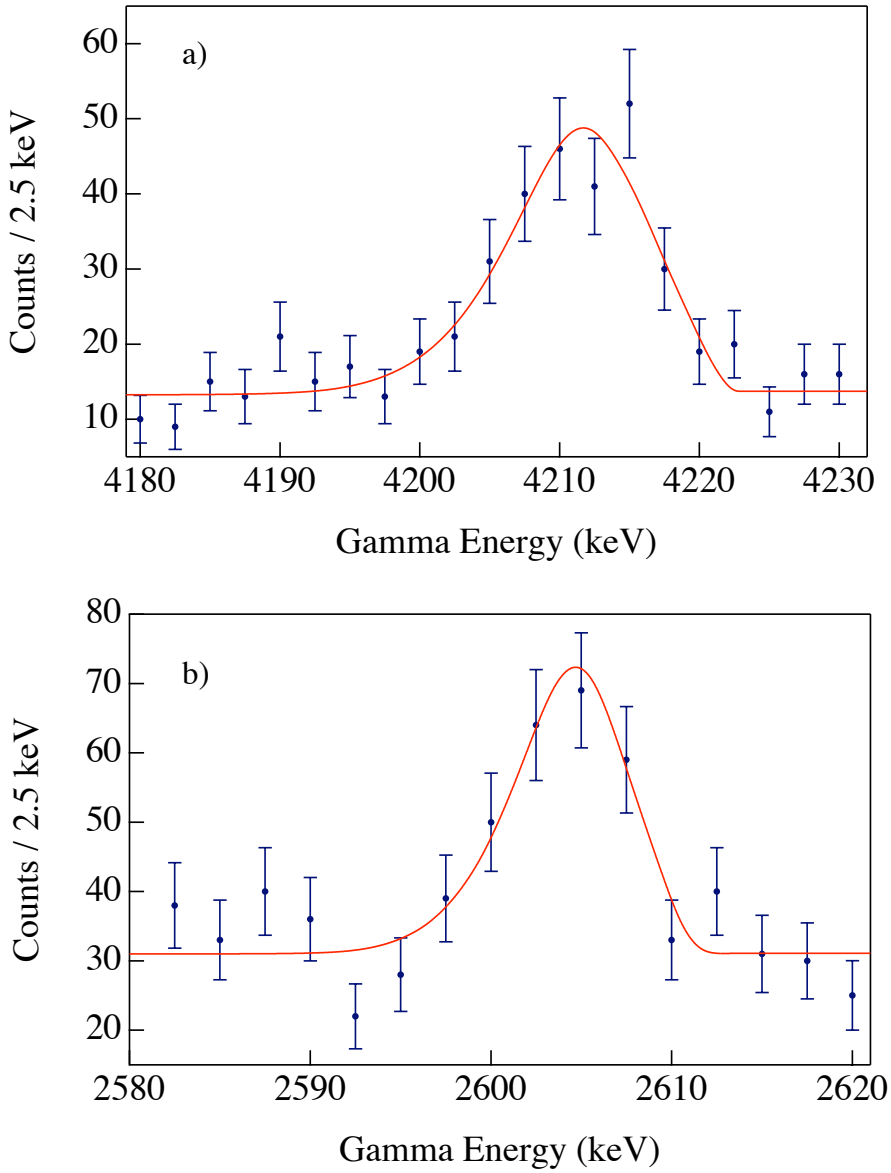

Figure 5.3: Doppler shifted line shapes due to two branches of the 4035 keV level. Panel (a) shows the decay to the ground state with a best fitting line shape corresponding to a lifetime (τ) of 7.1 fs. Panel (b) shows the decay to the level at 1536 keV fitted with a best fitting line shape corresponding to a τ of 6.6 fs. χ^2_{red} for the two transitions are 0.7 and 1.1 respectively.

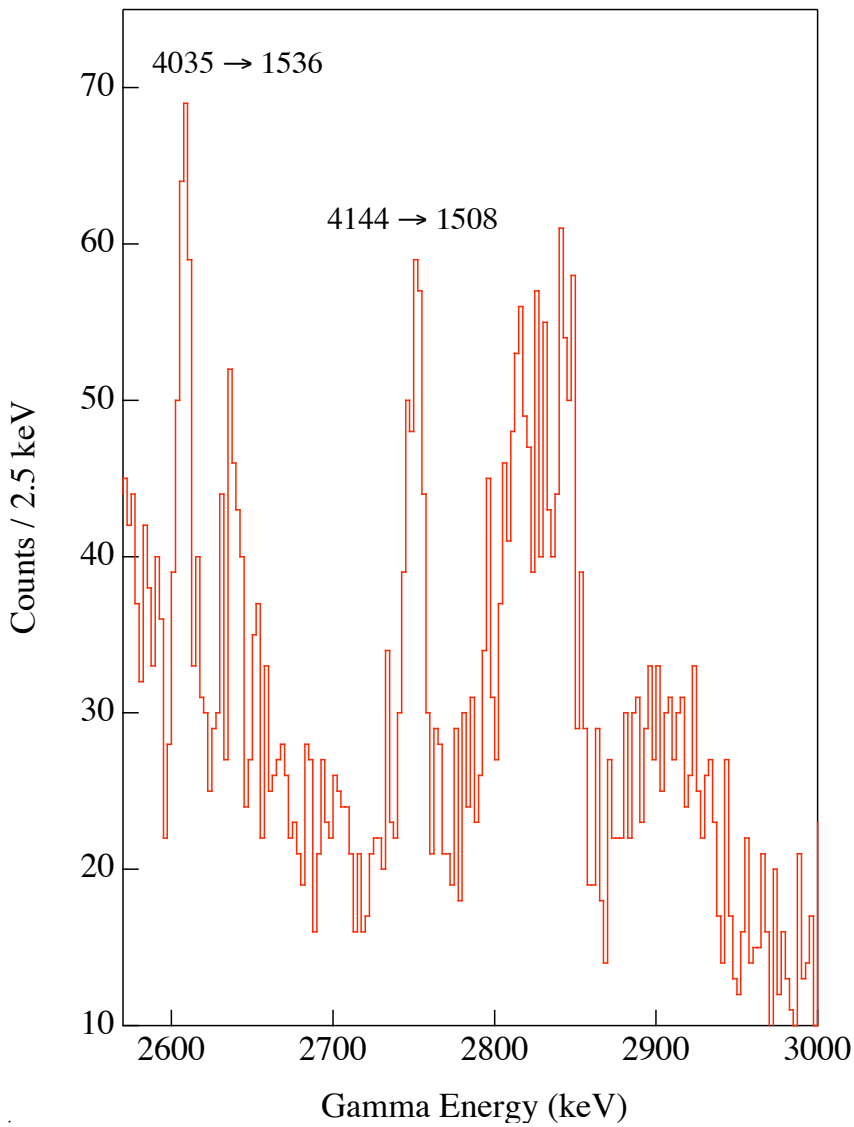

Figure 5.4: The Doppler shifted γ ray from the 4035 keV state in ^{19}Ne decaying to the 1536 keV state and the de-excitation of the 4144 keV state to the 1508 keV state.

branch. The excellent agreement of the lifetimes of the two branches and the observation of the γ ray at 2608 keV with an α gate that corresponds to the excitation of the 4035 keV level represent incontrovertible evidence that the second branch of the 4035 keV level has been observed in this experiment.

The transition of the 4035 keV state to the ground state gives a lifetime of $7.1^{+1.9}_{-1.9}\pm0.6$ fs and the lifetime of the state measured via the second branch (4035 keV →1536 keV) was $6.6^{+2.4}_{-2.1}\pm0.7$ fs.

5.2.3 Joint Likelihood

Whenever there are two or more independent measurements available for the lifetime τ, one can combine the different results, weight them with appropriate errors and construct a joint likelihood function. The methodology for this approach is explained below.

The likelihood function $l(\tau)$ satisfies

$$l(\tau) \propto e^{-}\frac{\Delta\chi^2(\tau)}{2} \tag{5.2}$$

where $\Delta\chi^2(\tau)$ is

$$\Delta\chi^2(\tau) = \chi^2(\tau) - \chi^2_{min} \tag{5.3}$$

where χ^2_{min} is the minimum value of $\chi^2(\tau)$, i.e.,

$$\chi^2_{min} = Min(\chi^2(\tau) \mid 0 < \tau < \infty) \tag{5.4}$$

The function $l(\tau)$ is the probability distribution function for a single measurement, evaluated with the data obtained in the experiment and is a function of τ alone.

If there are two or more independent measurements, a likelihood function is constructed for each measurement and the joint likelihood is the product of the individual likelihood functions. For N measurements, the joint likelihood function satisfies

$$L(\tau) \propto \prod_{i=1}^{N} l_i(\tau) \tag{5.5}$$

where the subscript i runs from 1 to N. Using Relation 5.2, we get

$$L(\tau) \propto e^{-\sum_{i=1}^{N}\frac{\Delta\chi_i^2(\tau)}{2}} \tag{5.6}$$

To find the most likely value from 2 or more measurements, we must find the maximum of the joint likelihood function. This corresponds to minimizing

$$\chi^2 \equiv \sum_{i=1}^{N} \Delta\chi_i^2(\tau) \tag{5.7}$$

To facilitate interpolation, $\Delta\chi^2$ is computed for a number of τ values and the locus fitted with a polynomial of order 5 for each of the N measurements. χ^2 is computed by adding the fitted functions together, as per Eq. 5.7. The joint likelihood function was normalized by requiring

$$\int_0^\infty L(\tau)d\tau = 1. \tag{5.8}$$

The most likely value of τ is identified as the minimum. The 1σ, 2σ and 3σ errors correspond to $\chi^2 = \chi^2_{min}+1$, $\chi^2_{min}+4$ and $\chi^2_{min}+9$ respectively.

The plots of the combined $\Delta\chi^2$ and the joint likelihood function for the 4035 keV state are shown in Figs. 5.5 and 5.6 respectively. The joint likelihood function peaks at 6.9 fs; hence we obtain 6.9 fs as the most probable central value of the lifetime for the 4035 keV state. Combining the two measurements resulted in a slight lowering of the statistical errors. For the 4035 keV state, the most likely lifetime was $6.9^{+1.5}_{-1.5}\pm0.7$ fs. The joint likelihood approach was followed whenever we had more than one transition from a certain state.

5.3 The 2500-3000 keV region in the γ spectrum

There are several peaks of interest in the 2500-3000 keV region of the γ spectrum shown in Fig. 5.7. This plot contains the γ rays coincident with α particles of all energies (not the usual range of 11 MeV $\leq$ E_α $\leq$ 14.5 MeV). There are five lines in the spectrum that were identified as transitions of ^{19}Ne states and two lines that likely originated from fusion evaporation residues. The compound nucleus formed by the fusion of ^{3}He and ^{20}Ne (^{23}Mg) would have sufficient energy to emit particles and γ rays. The emissions from the compound nucleus are referred to as fusion evaporation residues.

- The peak at 2557 keV, labeled (a) is the unshifted transition of the 2795 keV state to the 238 keV state. The Doppler shifted line due to this transition is labeled (c) in Fig. 5.7 and discussed later in this section. This is the only state for which we observed the unshifted and Doppler shifted transition.

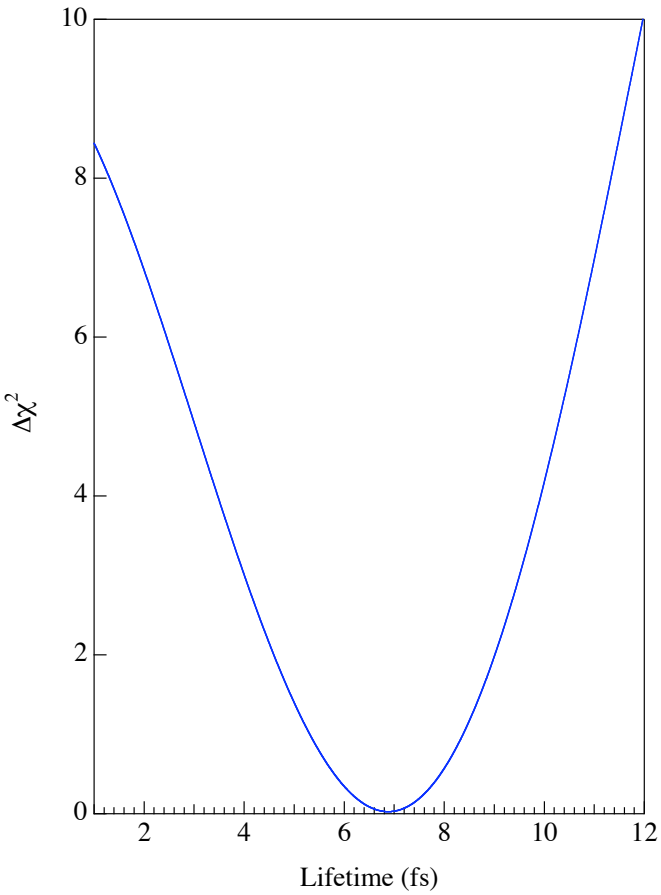

Figure 5.5: $\Delta\chi^2$ for the two measurements of the lifetime of the 4035 keV state.

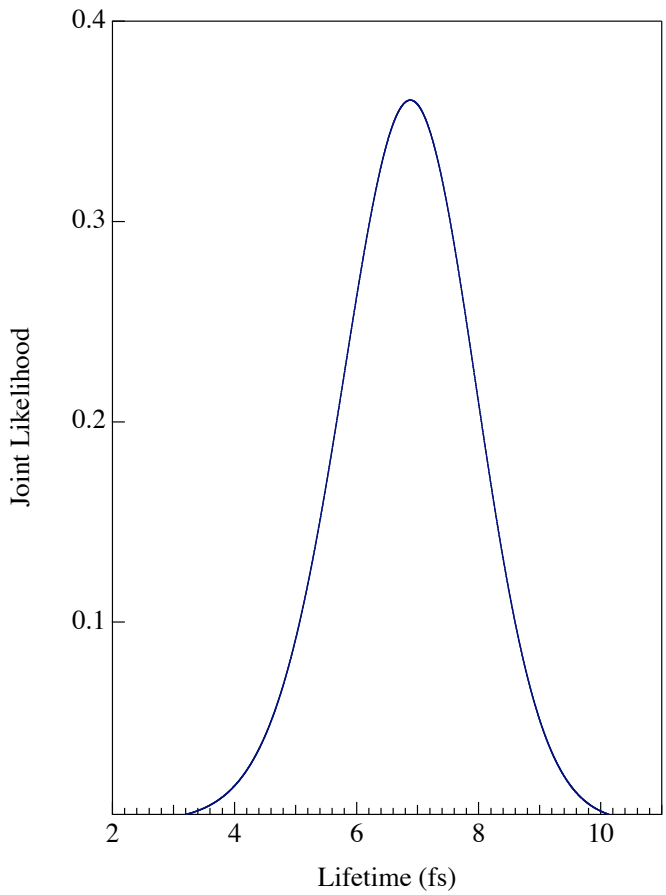

Figure 5.6: The joint likelihood for the lifetime of the 4035 keV state. The joint likelihood includes both transitions of the 4035 keV level observed in this experiment and yields a τ of $6.9^{+1.5}_{-1.5}\pm0.7$ fs. A detailed explanation can be found in the text.

- The peak at 2608 keV is the second branch of the 4035 keV state in ^{19}Ne decaying to the 1536 keV level. This line is seen with a better signal to noise ratio when 11 MeV $\leq$ E$_\alpha$ $\leq$ 14.5 MeV. It is labeled (b) in Fig. 5.7, was discussed in Sec. 5.2.2 and is seen in two other plots - Figs. 5.3(b) and 5.4.

- The peak at 2640 keV, labeled (c) in Fig. 5.7 is the Doppler shifted transition from the 2795 keV level in ^{19}Ne to the 238 keV level. This line is seen with good statistics with an E$_\alpha$ gate from 13.5 MeV to 17.0 MeV. Since the lifetime of this state is of the order of 140 fs [54], there are events due to Doppler shifted transitions as well as the unshifted line. The unshifted transition is labeled (a) in Fig. 5.7.

- The peak at 2748 keV is seen only when E$_\alpha$ lies between 11 MeV and 14.5 MeV. The peak labeled (d) in Fig. 5.7 corresponds to the transition of the 4144 keV level in ^{19}Ne to the 1508 keV level; it is discussed in Sec. 5.4 and shown in Fig. 5.4.

- The peak at 2814 keV is seen for E$_\alpha$ ranging from 11 MeV to 14.5 MeV. This is the transition of the 4200 keV level in ^{19}Ne to the 1508 keV level. The line peaks at 2814 keV and is discussed in Sec. 5.5. The γ ray is labeled (e) in Fig. 5.7. The large background that is observed with this γ ray is discussed below.

- The peak at 2840 keV is broad and close to the Doppler shifted transition of the 4200 keV level (decaying to the 1508 keV level) in ^{19}Ne. While the two peaks are distinct, the line at 2840 keV is seen with all values of E$_\alpha$, unlike the line at 2814 keV that is seen only for 11 MeV $<$ E$_\alpha$ $<$ 14.5 MeV. This is suggestive of a fusion evaporation origin for the line peaking at 2840 keV. Probing the possibility of a fusion reaction between ^{3}He and ^{20}Ne, the state at 2714 keV in ^{23}Mg appears to be a likely candidate [3]. Since ^{23}Mg fused in this way has an energy close to the beam energy ($34\times\frac{20}{23}$ MeV), the β for the compound nucleus $\sim$ 0.05. This implies that the 2714 keV line would be Doppler shifted to around 2840 keV. The long lifetime of this state (131 fs) leads to a long tail on the low energy side. The proximity of the transition from the 4200 keV level of ^{19}Ne, peaking at 2814 keV, impedes the observation of such a long tail from the state in ^{23}Mg. There is no clear way of isolating this line at 2840 keV to test this conjecture. The broad peak is labeled (f) in Fig. 5.7. The long low

energy tail of this line contributes to the background of the 2814 keV peak (Fig. 5.7(e)).

- The peak at 2910 keV, labeled (g) in Fig. 5.7 also appears for all values of E_α. This could be the Doppler shifted 2771 keV line from the compound nucleus ^{23}Mg. This state is long lived with a half life of 154 fs [3]. The line shape of the γ ray at this energy shows a long low energy tail indicating a fairly long lived state.

It is of particular interest that different line shapes afford a qualitative comparison of the lifetimes. A long tail in the low energy tail indicates a long lived state, as is the case with the lines at 2814 keV and 2910 keV while a sharp low energy tail is indicative of a short lifetime for the decaying state. The states at 2608 keV and at 2748 keV are relatively short lived and show a sharper low energy tail.

5.4 The state at 4144 keV

This state decays to the level at 1508 keV [54]. The γ ray of 2636 keV is Doppler shifted to yield a peak at 2748 keV. This is one of several lines of interest in the 2500 to 3000 keV region, shown in Figs. 5.4 and 5.7(d). Applying the appropriate E_α and timing gates, this line was isolated for lifetime analysis. The lifetime of the level was determined to be $14.0^{+4.2}_{-4.0}\pm1.2$ fs. The data and the best fitting line shape for this transition are shown in Fig. 5.8.

5.5 The state at 4200 keV

The state at 4200 keV is known to decay via two branches - an 80±5% branch to the level at 1508 keV and a 20±5% branch to the level at 238 keV [54]. The former transition results in a γ ray of 2693 keV while the latter has a higher energy of 3962 keV.

The 2693 keV line is Doppler shifted to 2814 keV. The γ spectrum, with appropriate α energy and timing gates is shown in Fig. 5.9. The spectrum revealed a long low energy tail indicating a fairly long lived state. The spectrum also showed a broad line peaking at 2840 keV, the possible source of which was discussed in Sec. 5.3. However the broad line lies on the high energy side of the line of interest and does not significantly affect the fitting of the low energy tail of the ^{19}Ne transition. The lifetime of this level was determined to be $38^{+20}_{-10} \pm 2$ fs and agrees with the only other measurement

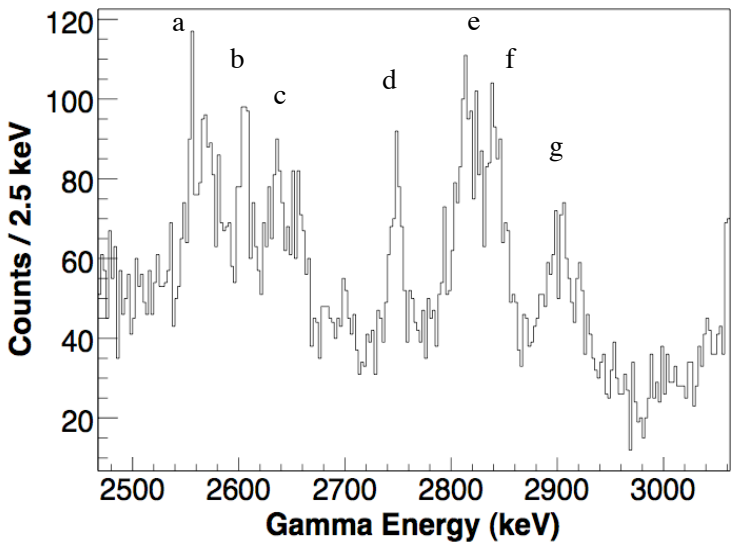

Figure 5.7: The γ rays in the 2500-3000 keV range using α particle and timing gates. The origin of the γ rays labeled $a - g$ is discussed in the text.

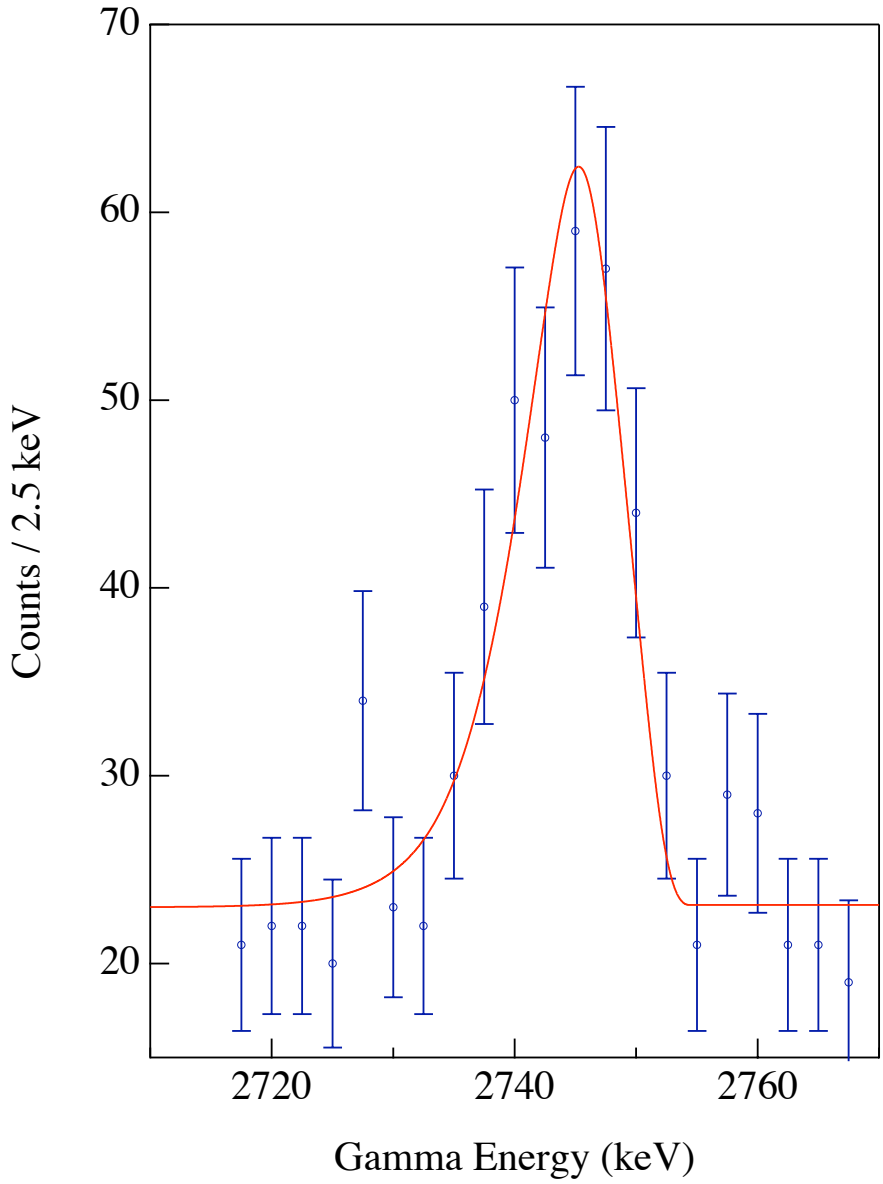

Figure 5.8: The γ ray due to the decay of the 4144 keV level is seen clearly, peaking at 2748 keV, with the appropriate E_α gate. The best fitting line shape corresponding to a lifetime of 14 fs is also plotted.The χ^2_{red} for this fit is 0.8.

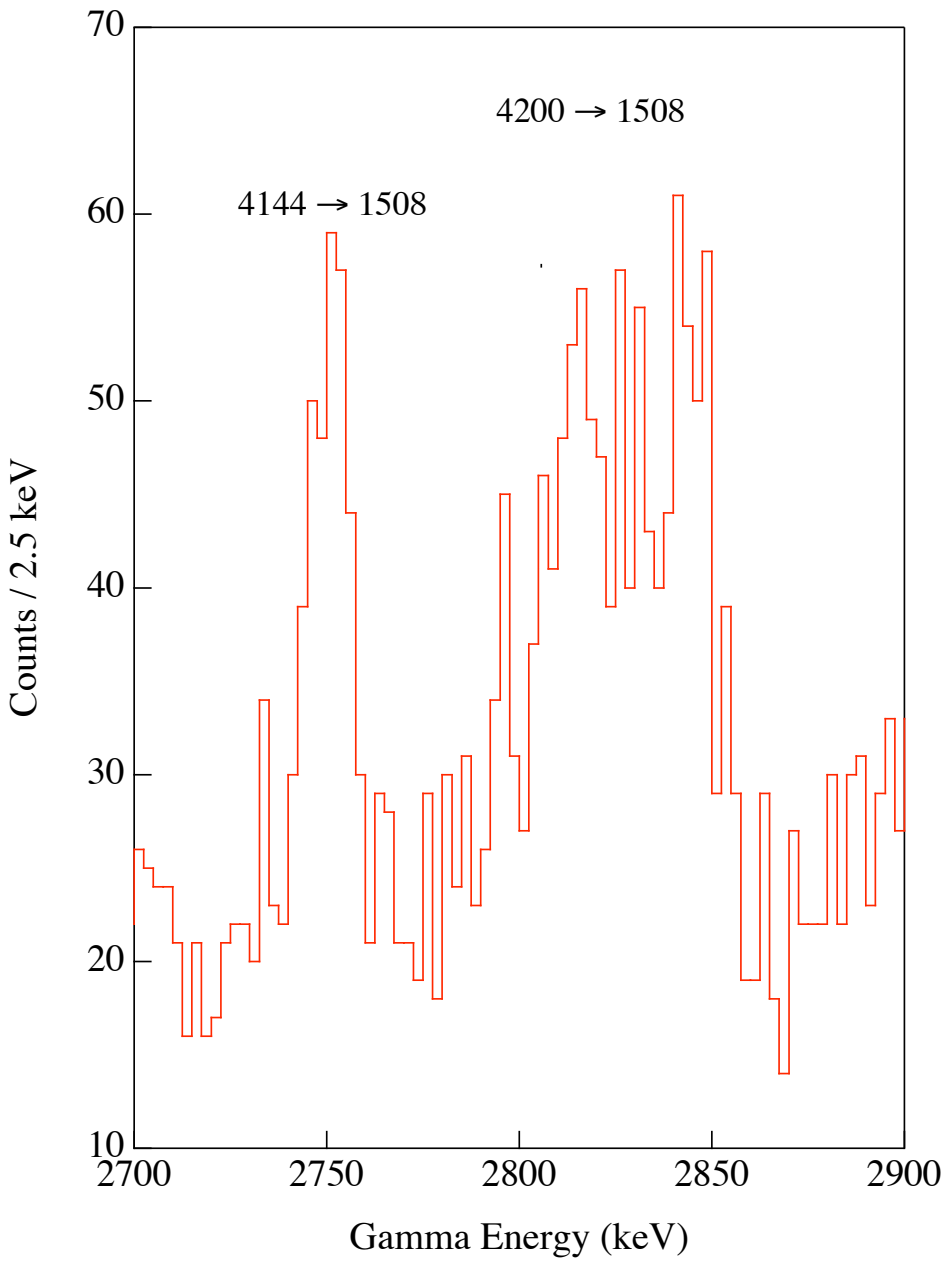

Figure 5.9: The γ ray due to the decay of the 4144 keV state is evident at 2748 keV. Also shown is the decay of the 4200 keV level peaking at 2814 keV.

[53]. The data for the Doppler shifted line from the 4200 keV level and the best fitting line shape to the data is shown in Fig. 5.10.

5.6 The state at 4378 keV

This is the shortest lived state we observed. It decays with an 85±4% probability to the 238 keV state and with a 15±4% probability to the state at 2795 keV [54]. This state was the benchmark for testing the Ge detector response. Since the lifetime for this state is short, the calculated line shape was expected to be most sensitive to the input parameters.

The stronger of the two transitions was identified with the appropriate E_α and timing gates. This γ line appears in Fig. 4.8. The line shape was analyzed and the minimum χ^2 was obtained for a lifetime of 2.9 fs. Fig. 5.11 shows the data and the best fitting line shape for this transition. The 1σ statistical and systematic errors were found to be ± 1.4 fs and ± 0.6 fs respectively. Although it was possible to determine a best fitting line shape and 1σ upper and lower limits on the lifetime of this state, the line shapes corresponding to lifetimes less than 1.5 fs were not distinguishable. Thus we were not confident of calculated line shapes for $\tau < 1.5$ fs. Instead of quoting a value for the lifetime with associated errors, an upper limit on the lifetime is specified at the 95% confidence level (CL).

To specify a 95% CL upper limit for the lifetime, the line shapes from several lifetimes were fitted to the data. The χ^2 for each lifetime was calculated. The minimum χ^2 was obtained for τ= 2.9 fs and the difference ($\Delta\chi^2$) between the χ^2 for each lifetime and the χ^2 corresponding to 2.9 fs line shape fit was evaluated. Fig. 5.12 shows the $\Delta\chi^2$ for different values of τ and a fifth order polynomial fit to the locus of $\Delta\chi^2$. The 95% CL upper limit is the lifetime that has a $\Delta\chi^2$ of 2.69. This corresponds to $\tau = 5.2$ fs. The systematic error was added in quadrature to the statistical $\Delta\tau$ and the 95% CL upper limit was determined to be 5.4 fs.

5.7 The state at 4548 keV

This level decays 65±25% of the time to the 275 keV level and the remainder of the time to the ground state with a decay probability of 35±25% [54]. Both branches of this level have been observed. The γ rays due to the two transitions were labeled in Fig. 4.8. The lifetime of this state was also calculated using the joint likelihood approach described in Sec. 5.2.3.

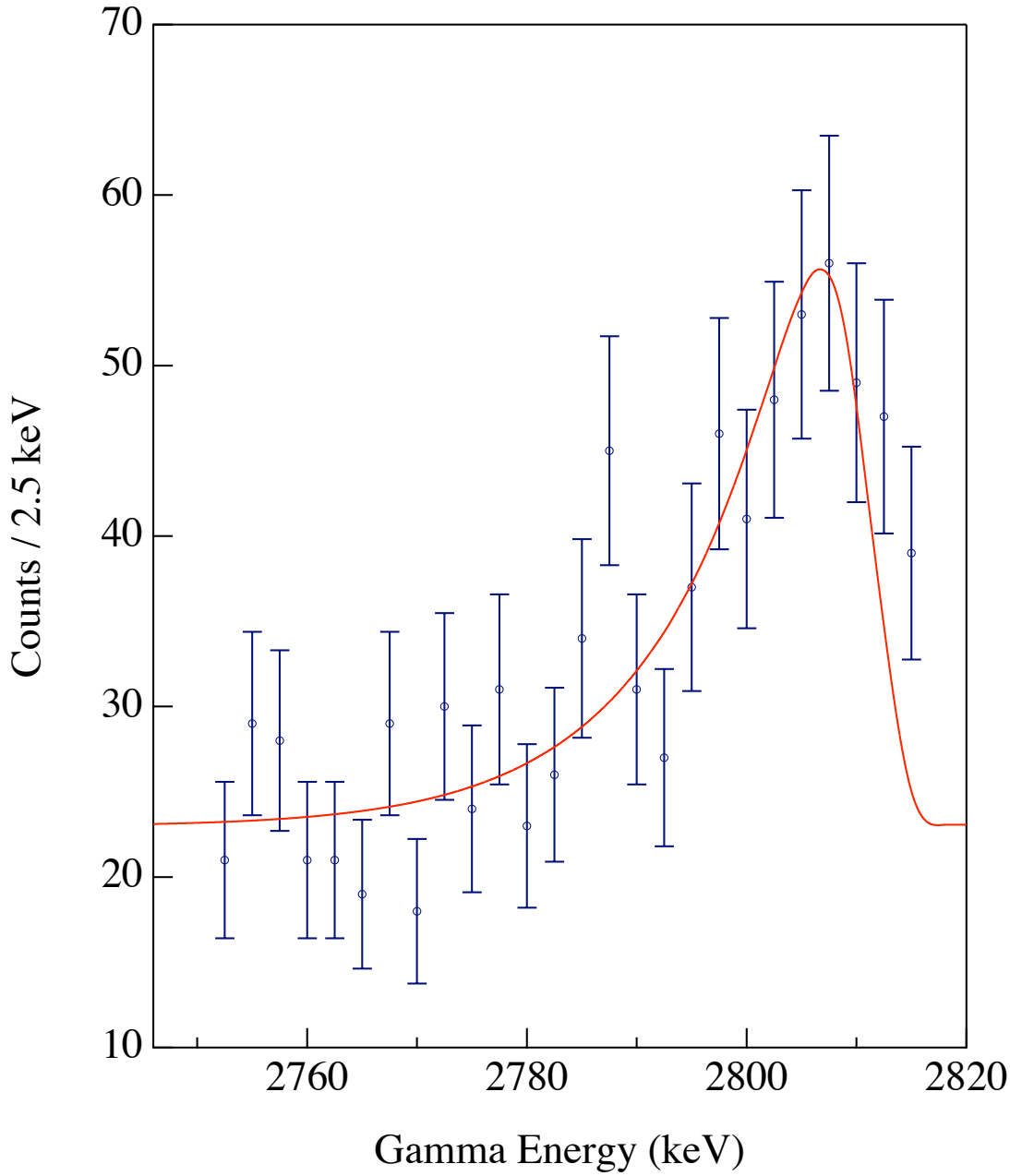

Figure 5.10: The γ ray spectrum due to the decay of the 4200 keV level and the best fitting line shape corresponding to a lifetime of 38 fs. The high energy tail has contributions from other γ rays, as described in the text. The χ^2_{red} for this fit is 0.9.

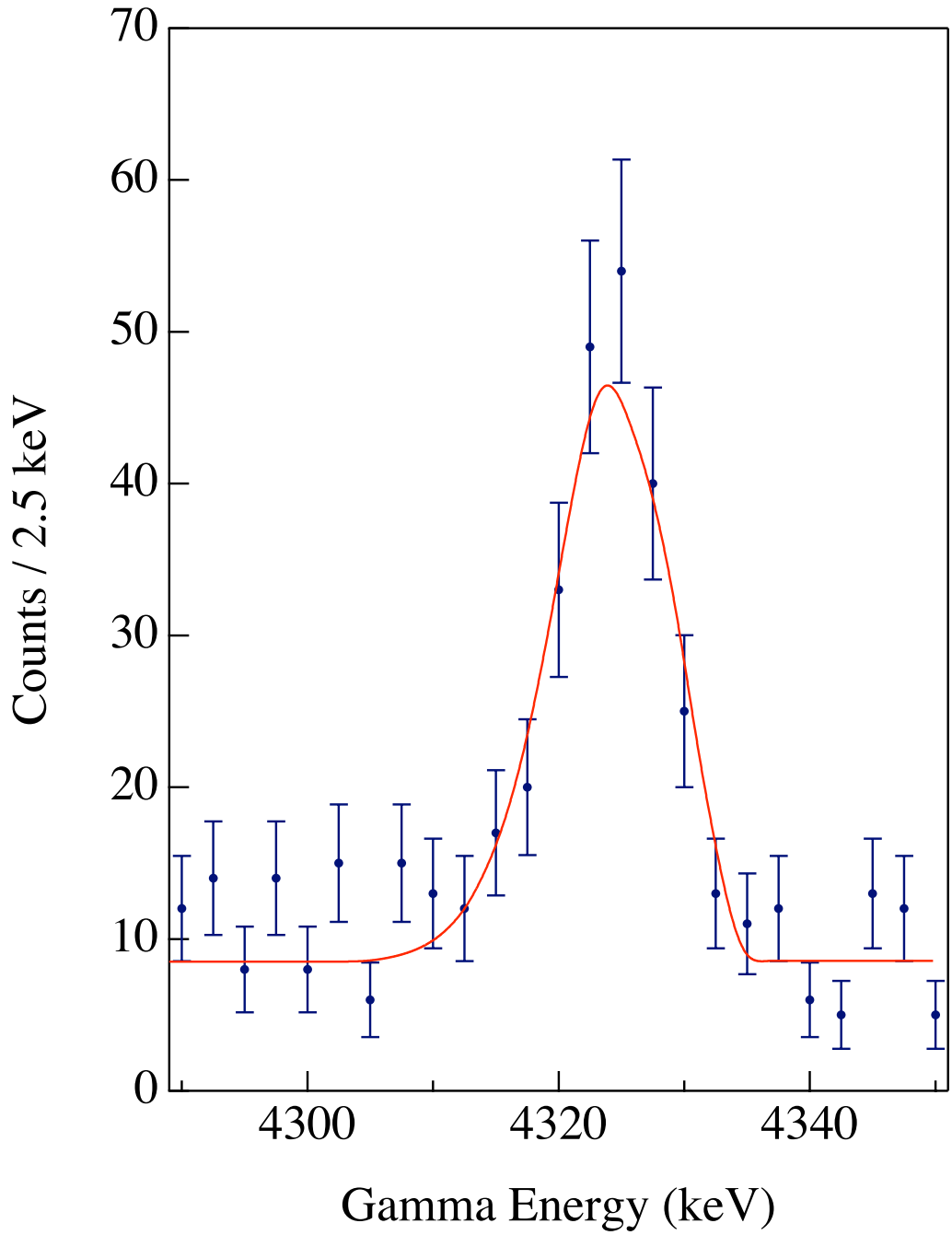

Figure 5.11: The γ ray due to the decay of the state at 4378 keV to the 238 keV state and the best fitting line shape corresponding to a τ of 2.9 fs. The χ^2_{red} for this fit is 0.6.

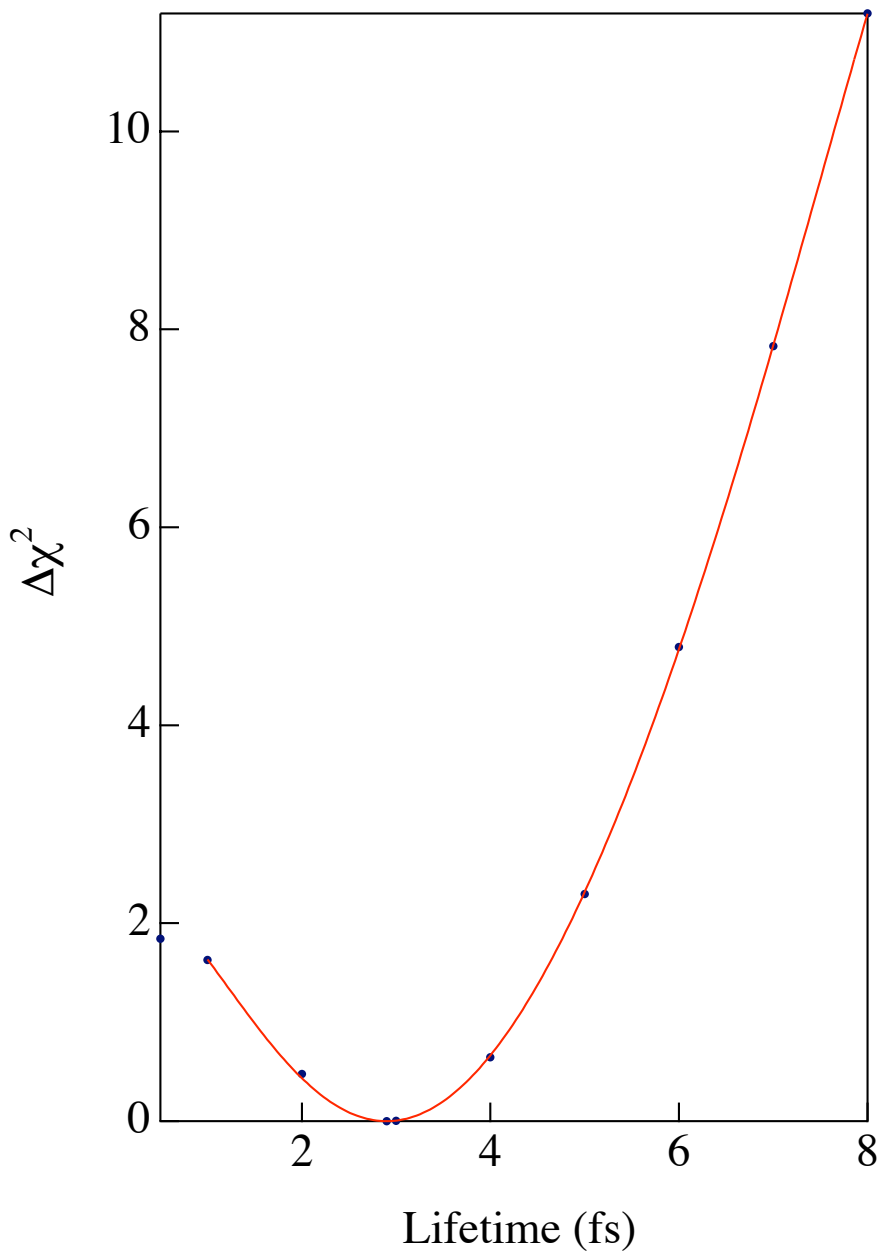

Figure 5.12: $\Delta\chi^2$ corresponding to different lifetimes for the 4378 keV state is shown by the closed circles. The solid line is a fifth order polynomial fit to the locus of $\Delta\chi^2$. The minimum at τ=2.9 fs and the increase of $\Delta\chi^2$ on both sides of τ=2.9 fs is evident.

The stronger branch yields a Doppler shifted line at 4462 keV. The lifetime was measured to be $16.6^{+4.4}_{-3.6}\pm1.6$ fs. The data and the best fitting line shape are shown in Fig. 5.13(a).

The γ ray corresponding to the transition of the 4548 keV level to the ground state was the highest energy γ ray analyzed in this experiment. The lifetime for this transition was found to be $19.9^{+3.0}_{-3.6}\pm2.3$ fs. Fig. 5.13(b) shows the ground state transition and the best fitting line shape.

Both branches yielded a consistent range for the lifetime for this state. The most probable value for the lifetime of the 4548 keV was calculated by combining the lifetimes of the two branches of the 4548 keV state and constructing a joint likelihood function. The likelihood function shown in Fig. 5.14 peaks at 18.7 fs. The most likely value of the lifetime is $18.7^{+3.0}_{-2.6}\pm2.2$ fs.

5.8 The state at 4602 keV

This state decays with two branches - a 90±5% branch to the 238 keV level and a 10±5% branch to the 1536 keV level [54]. The transition to the 238 keV level was observed at 4558 keV with good statistics, as seen in Fig. 4.8. The lifetime of this state was determined to be $7.6^{+2.1}_{-2.0}\pm0.9$ fs. The data and the best fitting line shape corresponding to a lifetime of 7.6 fs is shown in Fig. 5.15.

5.9 The state at 4634 keV

This high spin $\frac{13}{2}^+$ state decays exclusively to the $\frac{9}{2}^+$ state at 2795 keV [54]. The transition yields a γ ray of energy 1839 keV. This state is expected to be longer lived than the other states in the 4 MeV region [54] and its lifetime is expected to be over 1 ps. Hence the line shape would reflect a small shift from the unshifted γ ray energy of 1839 keV.

A γ ray was observed at 1848 keV with the appropriate E_α gate. This γ ray was not seen if the E_α gate selected another region of ^{19}Ne excitation energy. However some random coincidences with the 1836 keV transition of our ^{88}Y source were always observed. This can be seen by comparing the two plots in Fig. 5.16. Panel (a) shows the γ spectrum when E_α lies between 11 MeV and 14.5 MeV. Two peaks are seen, at 1836 keV and 1848 keV. In panel (b) of Fig. 5.16, the E_α gate was set between 16 MeV and 20 MeV. The 1848 keV line is not seen since the E_α energy range excluded the 4634 keV level in ^{19}Ne. Only the 1836 keV peak is seen. It is also seen that

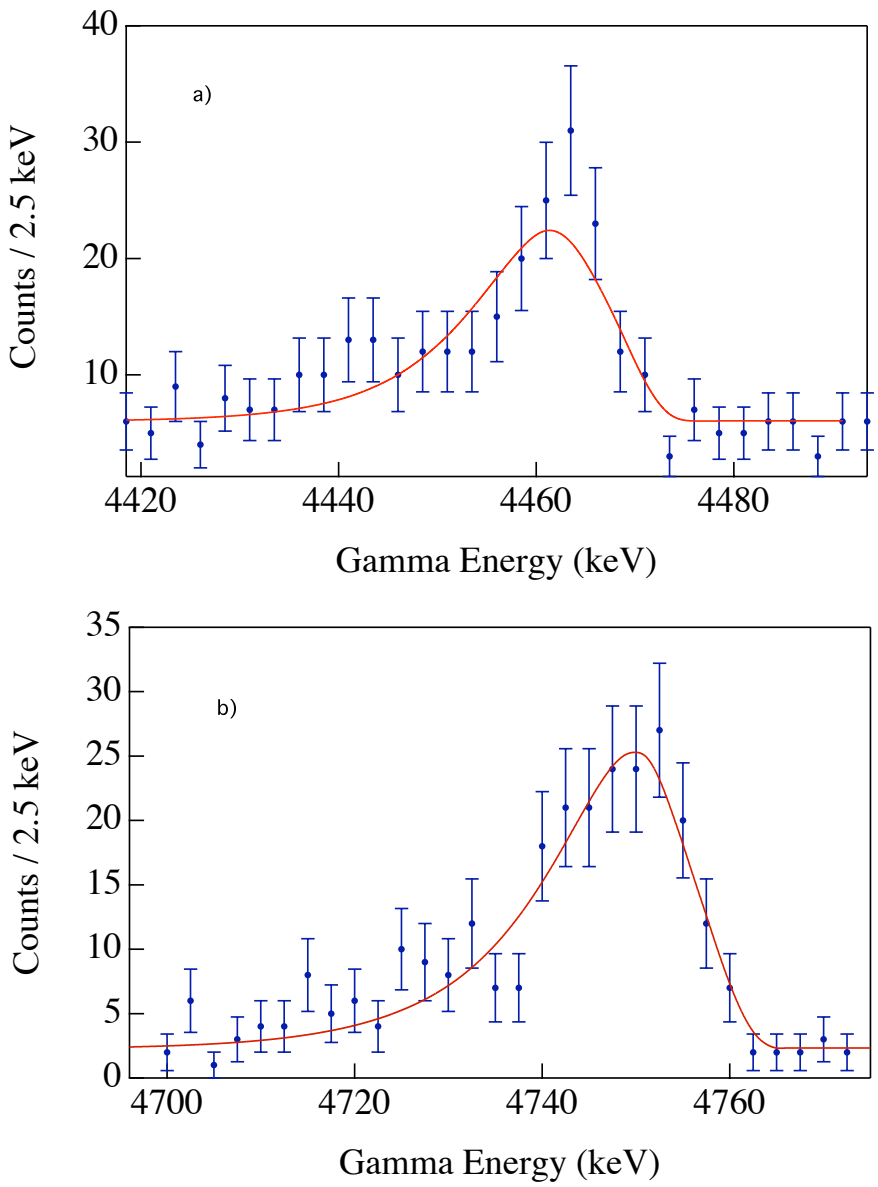

Figure 5.13: The data and the best fitting line shapes for the two branches of the 4548 keV level. The top panel (a) shows the best fitting line shape corresponding to a lifetime of 16.6 fs for the transition of the 4548 keV level to the 275 keV level and the bottom panel (b) shows the best fitting line shape corresponding to a lifetime of 19.9 fs for the transition to the ground state. The χ^2_{red} for the two transitions are 1.1 (panel (a)) and 0.9 (panel (b)).

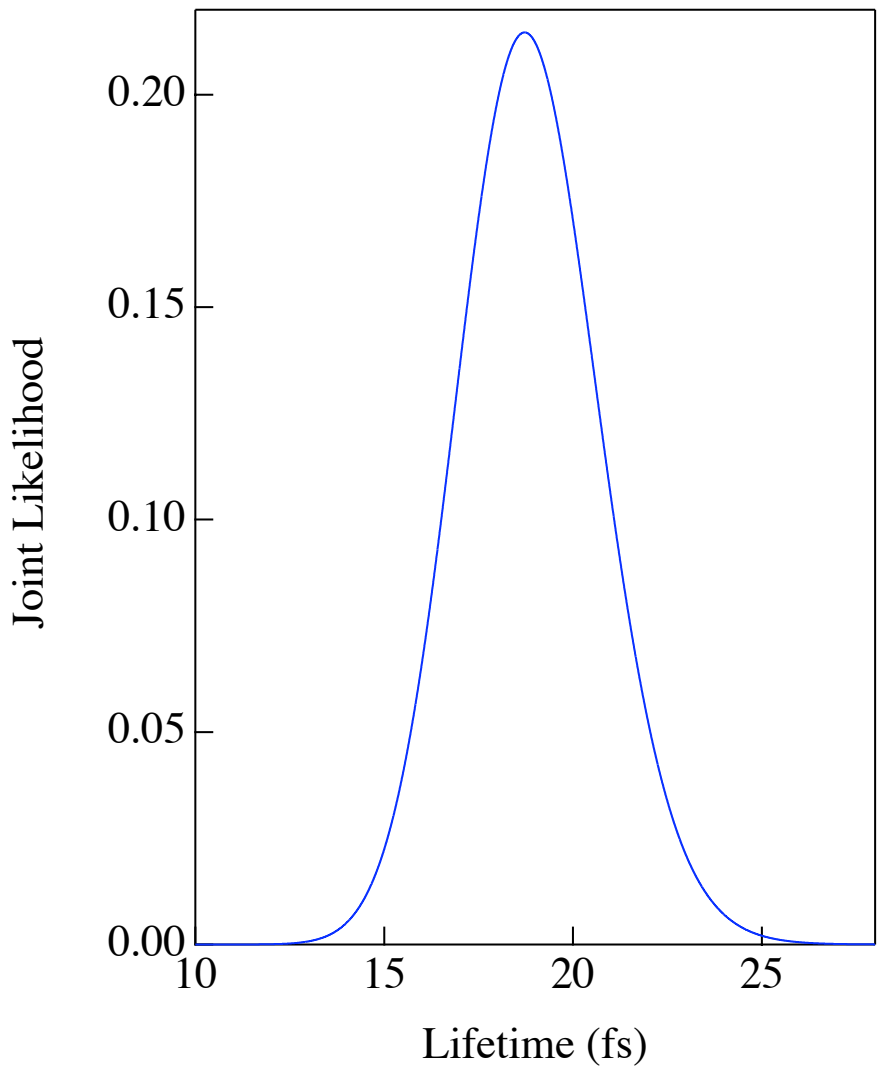

Figure 5.14: The joint likelihood for the lifetime of the 4548 keV state taking into account both transitions observed in this experiment. The lifetime measurements of the two branches were combined using the prescription detailed in Sec. 5.2.3. The likelihood function peaks at 18.7 fs.

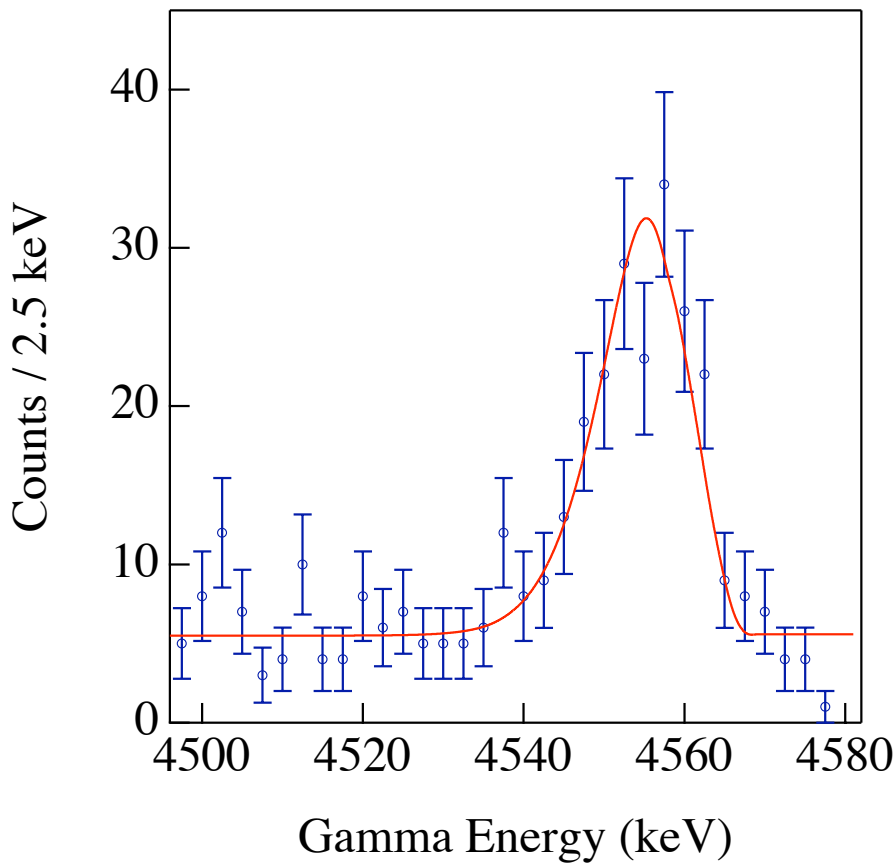

Figure 5.15: The data and the best fitting line shape corresponding to a lifetime of 7.6 fs for the 4602 keV level. The χ^2_{red} for this fit is 0.7.

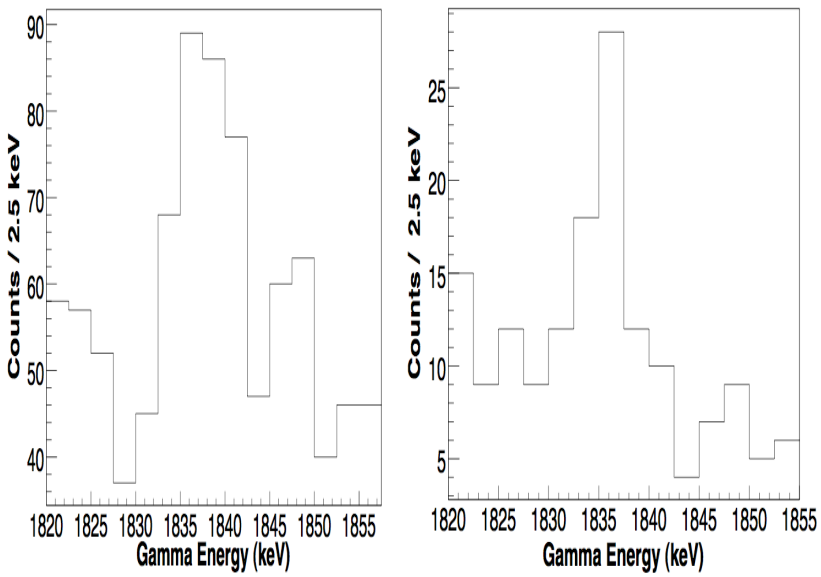

Figure 5.16: The γ ray energy spectrum around 1840 keV with differing E_α gates. Panel (a) is for 11 MeV$\leq$ E_α $\leq$14.5 MeV and panel (b) is for 16 MeV$\leq$ E_α $\leq$20 MeV. The differences in the two panels indicate that the 4634 keV state in ^{19}Ne was populated.

the 1836 keV peak is narrower in panel (b). The line appears broader in the panel (a) where the 1848 keV line is seen and its width reflects the long lifetime (and long low energy tail) of the 4634 keV $\rightarrow$ 2795 keV transition. Since the 1836 keV line from ^{88}Y was riding on the low energy tail of the γ ray at 1848 keV, no information regarding the lifetime of this state could be extracted from this line shape.

5.10 Summary Tables

Table 5.1 shows a summary of the transitions studied and the lifetimes measured in this experiment. The columns are the excitation energy of the level [54], the transition energy and the earlier reported measurements of the

lifetimes [32, 53]. The lifetimes measured here are shown in the last column. The combined lifetime measurements from both branches of the 4035 keV as well as the 4548 keV level are presented in the Table 5.1. Both statistical and systematic errors are included in the table.

The errors listed thus far are only 1σ errors. For the sake of completeness, the 2σ statistical errors and the 3σ statistical errors were also determined for all the lifetimes measured in this work. A $\pm 1\sigma$ range represents a 68% confidence interval, a $\pm 2\sigma$ range represents a 95% confidence interval and a $\pm 3\sigma$ range represents a 99.7% confidence interval. Table 5.2 summarizes the results for the 6 lifetimes measured for states in ^{19}Ne and the 1σ, 2σ and 3σ errors.

While the upper 1σ, 2σ and 3σ errors were determined for all the states, the lower 2σ and 3σ errors could not be determined for the state at 4378 keV. This is due to the similarity of the calculated line shapes for lifetimes shorter than 1.5 fs. However the upper 1σ, 2σ and 3σ limits for the 4378 keV state are tabulated along with a lower 1σ limit.

Three lifetimes measured here for transition energies above 4 MeV are the most precise thus far. However for the two transitions in the 2.5 to 3 MeV range, the results are not as precise because of the large background that could originate from fusion evaporation residues.

5.11 Coulomb Excitation of Gold

We observed several γ rays due to Coulomb excitation of the Au target by the ^{20}Ne beam. These γ rays arrived in random coincidence with particles in the ΔE-E telescope. The γ rays at 547 keV and 583 keV were of particular interest. The line at 547 keV was observed in neutron scattering experiments as well as in Coulomb excitation experiments. The state from which the 547 keV γ ray originates has a spin and parity of $(7/2)^+$ [3]. However the state at 583 keV has been observed only in polarized deuteron scattering experiments and has no spin assignment thus far. The strengths of the two Au coulex lines at 547 keV and 583 keV are comparable, as can be seen from Fig. 5.17.

Level Energy (keV)	E_γ (keV)	Lifetime (fs) Ref. [53]	Lifetime (fs) Ref. [32]	Lifetime (fs) This work
1536	1297.8(4)	16±4		$19.1^{+0.7}_{-0.6}\pm1.1$
4035	2498.5(9)			$6.6^{+2.4}_{-2.1}\pm0.7$
	4034.5(8)	13^{+9}_{-6}	11^{+4}_{-3}	$7.1^{+1.9}_{-1.9}\pm0.6$
	Combined			$6.9^{+1.5}_{-1.5}\pm0.7$
4144	2635.9(7)	18^{+2}_{-3}		$14.0^{+4.2}_{-4.0}\pm1.2$
4200	2692.7(11)	43^{+12}_{-9}		$38^{+20}_{-10}\pm2$
4378	4139.5(6)	5^{+3}_{-2}		≤ 5.4 (95% C.L.)
4548	4272.6(10)			$16.6^{+4.4}_{-3.6}\pm1.6$
	4547.7(10)	15^{+11}_{-5}		$19.9^{+3.0}_{-3.6}\pm2.3$
	Combined			$18.7^{+3.0}_{-2.6}\pm2.2$
4602	4363.5(8)	7^{+5}_{-4}		$7.6^{+2.1}_{-2.0}\pm0.9$

Table 5.1: Lifetimes of states of ^{19}Ne. The energy of the decaying level, the transition energy of the γ ray and the measurements from Refs. [53] and [32] are listed in the first four columns. The fifth column summarizes the lifetime measurements from this work. The 1σ statistical and systematic errors associated with this measurement are shown separately. The statistical errors are shown as superscript and subscript, followed by the statistical errors.

Level Energy (keV)	E_γ(keV)	Lifetime(fs)			
		Central	1σ	2σ	3σ
4035	2498.5(9)	6.6	$^{+2.4}_{-2.1}$	$^{+4.8}$	$^{+7.2}$
	4034.5(8)	7.1	$^{+1.9}_{-1.9}$	$^{+4.2}_{-4.7}$	$^{+6.8}$
	Combined	6.9	$^{+1.5}_{-1.5}$	$^{+3.1}_{-3.5}$	$^{+4.8}$
4144	2635.9(7)	14.0	$^{+4.2}_{-4.0}$	$^{+9.3}_{-7.0}$	$^{+15.7}_{-10.6}$
4200	2692.7(11)	38	$^{+20}_{-10}$	$^{+52}_{-19}$	$^{+93}_{-26}$
4378	4139.5(6)	2.9	$^{+1.4}_{-1.4}$	$^{+2.9}$	$^{+4.5}$
4548	4272.6(10)	16.6	$^{+4.4}_{-3.6}$	$^{+9.8}_{-7.3}$	$^{+17.1}_{-10.7}$
	4547.7(10)	19.9	$^{+3.0}_{-3.6}$	$^{+7.9}_{-6.2}$	$^{+12.8}_{-8.9}$
	Combined	18.7	$^{+3.0}_{-2.6}$	$^{+5.8}_{-4.9}$	$^{+9.4}_{-7.1}$
4602	4363.5(8)	7.6	$^{+2.1}_{-2.0}$	$^{+4.3}_{-4.3}$	$^{+6.9}$

Table 5.2: The excitation energy, transition energy and lifetime of states in ^{19}Ne are shown in the first three columns. The statistical 1σ, 2σ and 3σ errors are arranged in the next three columns.

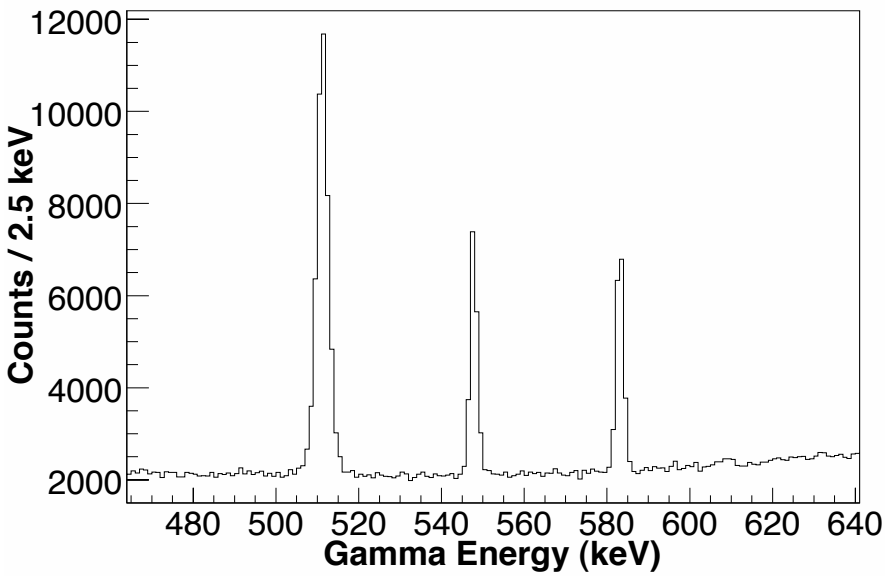

Figure 5.17: The e^+e^- annihilation peak at 511 keV and the two Coulex lines from gold at 547 and 583 keV.

Chapter 6

Discussion

Calculating the reaction rate for resonant α capture by ^{15}O above temperatures of 0.1 GK and below 2 GK requires detailed information on the states in ^{19}Ne above the α threshold of 3.53 MeV. The lifetimes of five of the states of ^{19}Ne above 3.53 MeV were measured in this experiment. These measurements led to two results, both of astrophysical importance.

Using Eq. 1.12 the strength $\omega\gamma$ of a ^{19}Ne resonance populated via the ^{15}O$(\alpha,\gamma)^{19}$Ne reaction can be written as

$$\omega\gamma = \frac{2J+1}{(2J_{^{15}O}+1)(2J_\alpha+1)} B_\alpha(1-B_\alpha)\frac{\hbar}{\tau} \tag{6.1}$$

where

- J is the spin of the resonance,
- $J_{^{15}O}$, the intrinsic angular momentum of ^{15}O is 1/2 and
- J_α, the spin of the α particle is 0.

To calculate $\omega\gamma$ for the resonance of spin J, the lifetime τ and the α decay branching ratio B_α are needed.

There has been only one previous measurement of the lifetimes of all six levels above the α threshold studied here [53]. In addition there was a measurement of the lifetime of the 4035 keV level [32]. The present measurement agrees well with the previous measurements. Moreover the values of three lifetimes measured here are considerably more precise than the earlier measurements. Two of these three states are of great astrophysical importance as they contribute dominantly to the breakout from HCNO cycles in X-ray bursts. The high precision of the measurement done here is useful in calculating the reaction rate. Details follow in Sec. 6.1. The lifetime measurements also led to a conjecture about interchanging the spins of two states in ^{19}Ne with tentative spin assignments that will be discussed in Sec. 6.2.

6.1 Astrophysical Reaction Rates

This work has yielded the most precise values for the lifetimes of several states in ^{19}Ne. The lifetimes of 5 states in ^{19}Ne above the α threshold are now well known. In particular the lifetime of the 4035 keV state in ^{19}Ne, believed to contribute dominantly to the reaction rate of ^{15}O$(\alpha,\gamma)^{19}$Ne in X-ray bursts is now known with great precision.

In Sec.1.2 the rate of a reaction dominated by narrow resonances was discussed. The reaction rate at a temperature T can be evaluated if the strengths of the individual resonances are known. Following the prescription in Ref. [36], the thermally averaged reaction rate is

$$< \sigma v >= (\frac{2\pi}{\mu k_B T})^{3/2}\hbar^2 \sum_{i=1}^{N}(\omega\gamma)_i e^{-E_i/k_B T} \tag{6.2}$$

where

- μ is the reduced mass and is defined in terms of the mass of the projectile m$_p$ and the mass of the target M$_t$ as $\frac{m_p M_t}{m_p+M_t}$,
- k$_B$ is Boltzmann's constant,
- E$_i$ is the energy of the resonance in the center of mass frame,
- $\omega\gamma$ is the strength of the resonance and
- N is the total number of resonances that contribute to the reaction rate.

Using the values of the spins for ^{15}O and α, Eq. 6.1 can be simplified as

$$\omega\gamma = \frac{2J+1}{(2J_{^{15}O}+1)(2J_\alpha+1)}B_\alpha(1-B_\alpha)\frac{\hbar}{\tau} = \frac{2J+1}{2}B_\alpha(1-B_\alpha)\frac{\hbar}{\tau} \tag{6.3}$$

J refers to the angular momentum of the resonance.

$\omega\gamma$ can also be evaluated in terms of the radiative width Γ_γ and B$_\alpha$ by the following equation.

$$\omega\gamma = \frac{2J+1}{2}\Gamma_\gamma B_\alpha \tag{6.4}$$

We use either Eq. 6.4 or Eq. 6.3 to calculate the reaction rate by summing over the strengths of individual resonances at E$_i$= 506 keV, 849 keV, 1019 keV, 1073 keV, 1183 keV and 1563 keV. These resonances correspond to the ^{19}Ne levels at 4035 keV, 4378 keV, 4548 keV,4602 keV, 4712 keV and

5092 keV respectively. The resonances at E_i = 615 keV and 671 keV (corresponding to the 4144 keV and 4200 keV states in ^{19}Ne respectively) are not included in the rate calculation for two reasons - they are not expected to contribute significantly due to the high centrifugal barrier and there are no reliable B_α measurements for these resonances in ^{19}Ne.

The contribution from an individual resonance to the reaction rate for is

$$< \sigma v >_i = (\frac{2\pi}{\mu k_B T})^{3/2} \hbar^2 (\omega\gamma)_i e^{-E_i/k_B T} \tag{6.5}$$

where all the symbols are identical to those defined in Eq. 6.2. The strengths of the resonances are calculated individually. We need the distribution of the lifetimes, α decay branching ratios and radiative widths to calculate the contribution from each resonance.

From this experiment we have the central values for the lifetimes of the 4035 keV level, the 4348 keV level, the 4548 keV level and the 4602 keV level as well as 1σ errors. From these measurements (using Table 5.1) we get the distribution of the lifetimes of these four states.

The central values and errors associated with B_α for the ^{19}Ne states at 4548 keV, 4602 keV, 4712 keV and 5092 keV are tabulated in Table 1.1. The upper limits on B_α for the resonances at 4035 keV and 4378 keV are also shown in Table 1.1. The observed background and the total number of events recorded from the states at 4035 keV and 4378 keV were used to calculate the probability distribution for B_α for the two resonances. Using the numbers from Ref. [16], a Poisson distribution for the B_α values of the 4035 keV and 4378 keV states was constructed.

The lifetimes of the 4712 keV level and the 5092 keV level have not been measured so far. We adopt the central values and errors of the radiative widths and B_α values for the 4712 keV level and the 5092 keV from Ref. [15].

The relevant values for the 6 resonances are tabulated in Table 6.1. The first and second columns in the table represent the excitation energy E_x and the spin of the state J^π. The third column lists the B_α values (with errors), the fourth column lists the values of τ and associated errors and the fifth column contains the Γ_γ values and errors from analog states. The 90% CL upper limits on B_α for the 4035 keV and the 4378 keV states are indicated by the superscript ^{UL}. Using the values in Table 6.1, the Monte Carlo method was used to simulate the 90% CL upper limit contributions from each resonance as well as a 90% CL upper limit contribution from the sum of the 6 resonances.

E_x (MeV)	J^π	B_α	τ (fs)	Γ_γ (meV)
4.035	$3/2^+$	$4.3\times10^{-4\ UL}$	6.9±1.7	
4.378	$7/2^+$	$3.9\times10^{-3\ UL}$	2.9±1.7	
4.548	$(3/2)^-$	0.10±0.02	18.7±3.7	
4.602	$(5/2)^+$	0.30±0.02	7.6±2.3	
4.712	$(5/2)^-$	0.85±0.04		43±8
5.092	$5/2^+$	0.90±0.05		107±17

Table 6.1: The excitation energies, spins, α decay branching ratios, lifetimes and radiative widths of states in ^{19}Ne above the α threshold that were used to calculate the reaction rate. The superscripts ^{UL} on the 4035 keV and the 4378 keV levels refer to the 90% CL upper limits on the α decay branching ratios for these two resonances.

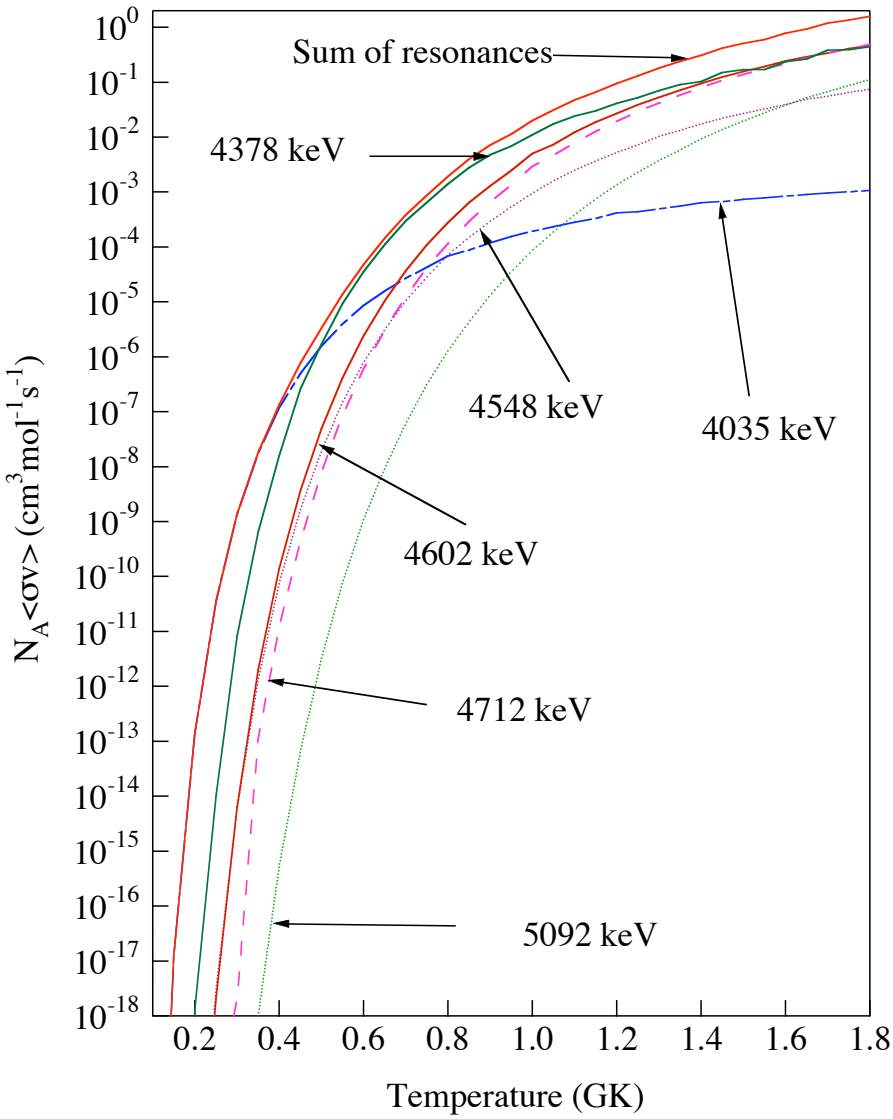

Figure 6.1: The product of Avogadro number (N_A) and the thermally averaged rate of the $^{15}O(\alpha,\gamma)^{19}Ne$ reaction per particle pair as a function of temperature. The 90% CL upper limits on the contributions from different resonances of ^{19}Ne are labeled along with the sum of the 90% CL upper limits.

Fig. 6.1 shows the product of the Avogadro number (6.022×10^{23} mol^{-1}) and the 90% CL upper limits of the contributions of individual resonances at 4035 keV, 4378 keV, 4548 keV, 4602 keV, 4712 keV and 5092 keV in ^{19}Ne to the thermally averaged ^{15}O$(\alpha,\gamma)^{19}$Ne reaction rate per particle pair as a function of the temperature. Also shown is the sum of the 90% CL upper limits on the contributions from the 6 resonances. The dominant contribution to the reaction rate for temperature (T) below 0.5 GK appears to be from the 4035 keV state in ^{19}Ne. The 4378 keV state and the 4602 keV states are expected to contribute significantly to the rate for T $>$ 0.8 GK. Although the 4548 keV state's contribution is shown in Fig. 6.1, the state's contribution is up to an order of magnitude lower than that of the 4602 keV state. The contribution from the 4712 keV state is marginally lower than that from the 4602 keV states for $T < 1$ GK; however the 4712 keV state contributes significantly beyond 1 GK. The state at 5092 keV plays no significant role for $T < 1$ GK.

The sum of the 90% CL upper limits on the contributions to the reaction rate from the six individual resonances shown in Fig. 6.1 is higher than the 90% CL upper limit on the total reaction rate simulated by the Monte Carlo calculations. This is seen in Fig. 6.2 where the sum of the 90% CL upper limit on the contributions of the 6 resonances as a function of temperature is shown by the dotted blue curve. Events for the 6 resonances were drawn from their respective distributions and then summed to get a 90% CL upper limit on the total rate. This is plotted as the solid red curve in Fig. 6.2. While the two curves agree at low temperatures, there is considerable disagreement at higher temperatures (T >0.7 GK). Since only the 4035 keV state contributes predominantly to the reaction rate at T <0.7 GK, the disagreement between the two curves is not seen at low temperatures. However beyond 0.7 GK, several resonances play a role in the reaction rate (as is evident from Fig. 6.1) and thus the 90% CL upper limit on the total rate is considerably smaller than the sum of the 90% CL upper limits on the contributions to the reaction rate from the 6 resonances.

As discussed in Sec.1.2, nova temperatures peak below 0.4 GK. At these temperatures only the 4035 keV state contributes appreciably to the rate of the ^{15}O$(\alpha,\gamma)^{19}$Ne reaction. The reaction rate calculated with the lifetimes measured in this work supports the conclusion of Refs. [14, 15, 61] that the ^{15}O$(\alpha,\gamma)^{19}$Ne reaction does not play an important role in nova explosions because at the hottest temperatures of the accreted envelope the β^+ decay of ^{15}O occurs at a much faster rate than the ^{15}O$(\alpha,\gamma)^{19}$Ne reaction. The ^{15}O nuclei β decay before they capture an α particle. The ^{15}O$(\alpha,\gamma)^{19}$Ne reaction does not lead to a HCNO breakout in novae. At higher tempera-

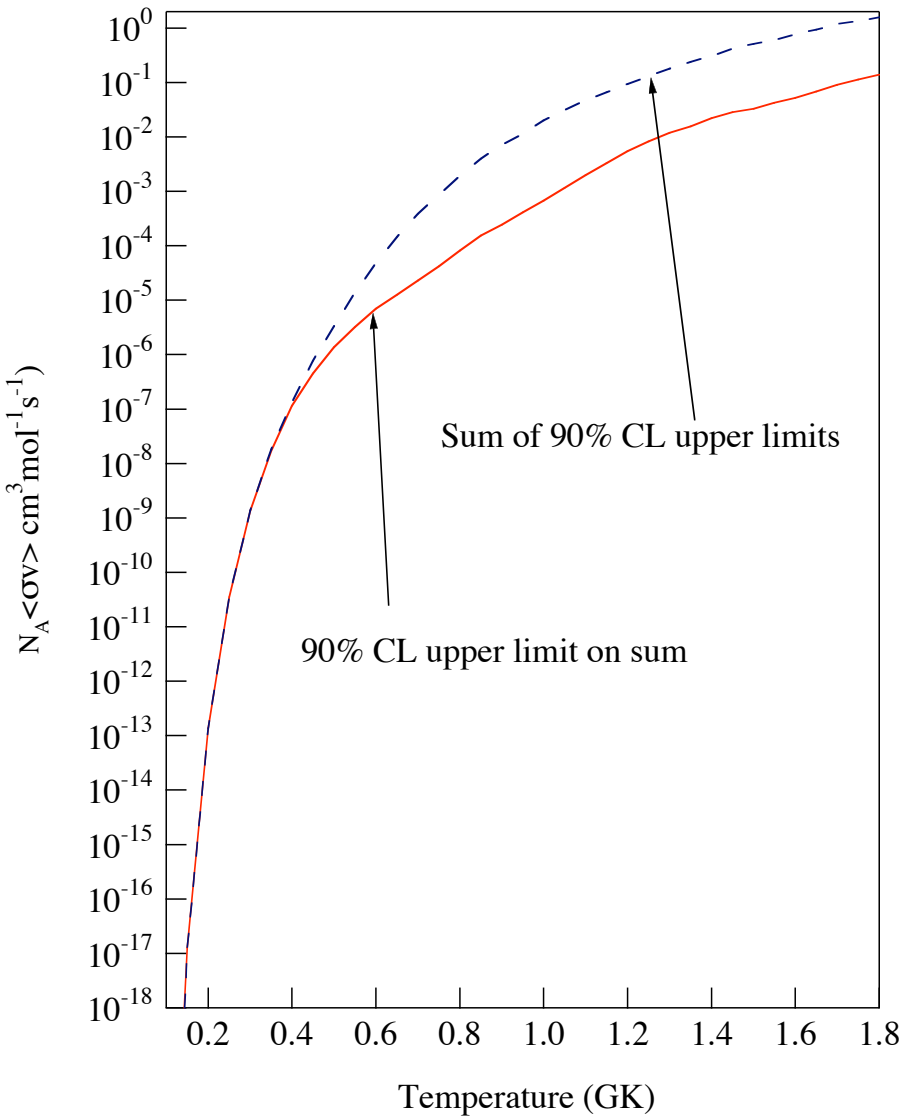

Figure 6.2: The product of Avogadro number (N_A) and the thermally averaged rate of the $^{15}O(\alpha,\gamma)^{19}Ne$ reaction per particle pair as a function of temperature. The sum of the 90% CL upper limits on the contributions of 6 resonances is shown along with the 90% CL upper limit on the total rate.

tures prevalent in X-ray binaries the $^{15}O(\alpha,\gamma)^{19}Ne$ reaction triggers the first breakout from HCNO cycles, with large contributions from the resonant α capture of ^{15}O leading to the 4035 keV state in ^{19}Ne. Currently the B_α for the 4035 keV state and the 4378 keV state are bound by upper limits. Reliable B_α measurements for the 4035 keV state and the 4378 keV state in ^{19}Ne are needed along with a higher precision measurement of the lifetime of the 4378 keV state to calculate a reliable central value for the rate of the $^{15}O(\alpha,\gamma)^{19}Ne$ reaction.

6.2 Spin Assignments

From Eq. 1.12 in Sec. 1.2, it can be seen that knowledge of the angular momentum is necessary for the determination of a resonance strength $\omega\gamma$. In the existing compilation [54], the spins for four of the seven levels studied here are not assigned definitively. The lifetimes of the isobaric analog states in ^{19}F with the lifetimes of those measured here were compared with an intention to understand the spin assignments in ^{19}Ne.

The measurements of the lifetimes of the states in ^{19}Ne done here are compared with the lifetimes of the isobaric analog states in ^{19}F in Table 6.2. This table lists the spins, excitation energies and lifetimes in the two isobars. The levels are arranged in ascending order of energy levels for ^{19}F. The spin assignments, energy levels and lifetimes of these states are taken from Ref. [54]. The levels in ^{19}Ne between excitation energy E_x = 3.9 to 4.7 MeV that have the same spin assignment as the levels in ^{19}F are compared in the table. The lifetimes of the levels in ^{19}Ne measured here are also included in the table. For the lifetimes of the levels at 4035 keV and 4548 keV in ^{19}Ne, the combined measurements of the two observed branches are listed in the table. The errors included in the table represent 1σ limits. All the levels in ^{19}F listed in Table 6.2 have definite spins assigned while four levels of ^{19}Ne in Table 6.2 are not assigned definite spins. The four levels of ^{19}Ne (in the order of their appearance in Table 6.2) are at 4200 keV which may be $(\frac{7}{2})^-$, at 4144 keV with a possible spin of $(\frac{9}{2})^-$, at 4602 keV with a spin assignment of $(\frac{5}{2}^+)$, and at 4548 keV with a spin assignment of $(\frac{1}{2},\frac{3}{2})^-$.

Of the six states compared in Table. 6.2, the lifetimes of four isobaric analog states in ^{19}F and ^{19}Ne agree within the 1σ limits. However the lifetimes of the 4200 keV and the 4144 keV states in ^{19}Ne do not match the lifetimes of the analog states in ^{19}F as well. Since the comparison in Table 6.2 has been made by matching the spins, it is suggested that perhaps the spins of these two states should be interchanged. A swapping of the possible

J^π	^{19}F Energy Level (keV)	Lifetime (fs)	J^π	^{19}Ne Energy Level (keV)	Lifetime This work(fs)
$\frac{3}{2}^+$	3908	9±4	$\frac{3}{2}^+$	4035	$6.9^{+1.5}_{-1.5}$ ±0.7
$\frac{7}{2}^-$	3999	19±7	$(\frac{7}{2})^-$	4200	38^{+20}_{-10} ±2
$\frac{9}{2}^-$	4033	67±14	$(\frac{9}{2})^-$	4144	$14.0^{+4.2}_{-4.0}$ ±1.2
$\frac{7}{2}^+$	4377	<11	$\frac{7}{2}^+$	4378	≤5.4 (95% C.L.)
$\frac{5}{2}^+$	4550	<50	$(\frac{5}{2}^+)$	4602	$7.6^{+2.1}_{-2.0}$ ±0.9
$\frac{3}{2}^-$	4556	17±9	$(\frac{1}{2},\frac{3}{2})^-$	4548	$18.7^{+3.0}_{-2.6}$ ±2.2

Table 6.2: Comparison of the energies and lifetimes of possible isobaric analog states in ^{19}F and ^{19}Ne. Only those states in ^{19}Ne whose lifetimes are measured here are included in this table. The properties of the mirror analog states in ^{19}F are taken from Ref. [54].

spins of the two states results in the agreement of the lifetimes with the isobar analog states in ^{19}F. Thus if the 4200 keV state were actually a $\frac{9}{2}^-$ state, its lifetime would agree well with the 4033 keV state in ^{19}F. Similarly the 4144 keV state in ^{19}Ne would have a comparable lifetime to its isobaric analog state, if it carried a spin of $\frac{7}{2}^-$. This was first proposed by Garrett *et al* [24] when they compared spins of the isobaric states in ^{19}F and ^{19}Ne. While the authors were certain of the distorted wave Born approximation fits to the ^{19}F data and the spins of several states in ^{19}F, they suggested that the spins of the 4144 keV and the 4200 keV states in ^{19}Ne could be interchanged.

It is known that most strong E2 transitions are dominated by their isoscalar components (where the neutron and proton contributions are identical) and the differences between the neutron and proton contributions (the isovector component) of the transition are small [9]. It is therefore expected that the reduced transition strength of the E2 transitions (B(E2) values) of isobaric analog states in ^{19}F and ^{19}Ne agree. Quasi Rule 5 in Ref. [60] states that *"Corresponding ΔT = 0 M1 transitions in conjugate nuclei are expected to be of approximately equal strength, within, say, a factor of two if the transitions are of average strength or stronger"*. From this Quasi Rule, one infers that the reduced width is approximately equal for moderately strong M1 transitions in mirror nuclei.The formulae used to calculate the reduced transition probabilities are outlined in App. G.

We now compare the reduced transition strengths of analog states in ^{19}F and ^{19}Ne. In particular we compare the reduced transition strengths of the 4200 keV state and the 4144 keV state in ^{19}Ne. The corresponding analog states in ^{19}F are the $\frac{7}{2}^-$ state at 3999 keV and the $\frac{9}{2}^-$ state at 4033 keV. Both the states in ^{19}F decay to the $\frac{5}{2}^-$ state at 1346 keV. The 3999 state has a branching ratio of 70±4% and its M1 transition has a B(M1) value of 0.062±0.024 Weisskopf units (WU)[54]. The state at 4033 keV in ^{19}F decays exclusively to the state at 1346 keV via an E2 transition with a B(E2) value of 28±6 WU.

To calculate the reduced transition strengths of the 4144 keV and 4200 keV states in ^{19}Ne, the excitation energies and the branching ratios for the 4144 keV and 4200 keV states in ^{19}Ne were taken from Ref. [53, 54]. The precise lifetimes for these two states in ^{19}Ne from Ref. [53] and the transition energies were used (with their tentative spins) to calculate the reduced transition strength. Table 6.3 lists the reduced transition strength for the two isobaric analog states in ^{19}F and ^{19}Ne. The 4200 keV state in ^{19}Ne is placed immediately below the 3999 keV state in ^{19}F since they are

Nuclei	J^π	Energy level (keV)	B(M1) (MeV fm^3)	B(E2) (MeV fm^5)
^{19}F	$\frac{7}{2}^-$	3999	0.0018±0.0007	
^{19}Ne	$(\frac{7}{2})^-$	4200	$0.0009^{+0.0003}_{-0.0002}$	
^{19}F	$\frac{9}{2}^-$	4033		120±30
^{19}Ne	$(\frac{9}{2})^-$	4144		510^{+100}_{-50}

Table 6.3: Reduced transition strength for two isobaric analog states in ^{19}F and ^{19}Ne.

listed as analog states. Similarly the 4144 keV state in ^{19}Ne is placed below the 4033 keV state in ^{19}F. Comparing the reduced transition probabilities of the isobaric analog states in Table 6.3, it is seen that while the B(M1) values agree within 1 σ limits, the B(E2) values of the isobaric analog states do not agree.

The reduced transition probabilities were recalculated after swapping the spins of the 4144 keV and the 4200 keV states in ^{19}Ne. The 4144 keV state is assigned $(\frac{7}{2})^-$ and the 4200 keV state is assigned a spin of $(\frac{9}{2})^-$. The swapping of the spins now affects the multipolariy of the transition. The 4144 keV transition to the 1508 keV level would be M1 and the 4200 keV transition to the 1508 keV state would be E2. The calculations for the reduced transition strengths after swapping the spins are summarized in Table 6.4.

Both the B(M1) and B(E2) reduced transition probabilities are in excellent agreement within 1σ limits, as seen in Table 6.4. The agreement of the B(E2) values is consistent with the expectation of the dominance of the isoscalar contribution to strong E2 transitions [9]. The lifetime measurements of the 4144 keV and the 4200 keV states in ^{19}Ne suggested a possible swapping of the spins. The calculation of the reduced transition probabilities supports this suggestion. This is mainly due to the fact that the relevant transition energies are very close and have little effect on the B(M1/E2) values. The lifetimes dominate the calculation of the reduced

Nuclei	J^π	Energy level (keV)	B(M1) (MeV fm^3)	B(E2) (MeV fm^5)
^{19}F	$\frac{7}{2}^-$	3999	0.0018±0.0007	
^{19}Ne	$(\frac{7}{2})^-$	4144	$0.0027^{+0.0005}_{-0.0003}$	
^{19}F	$\frac{9}{2}^-$	4033		120±30
^{19}Ne	$(\frac{9}{2})^-$	4200		150^{+50}_{-40}

Table 6.4: Reduced transition strength for two states in ^{19}F and two states in ^{19}Ne after a reassignment of the spins.

transition strengths.

However the trend of the branching ratios of the analog states is in agreement with the spins currently assigned in the compilation. The 4144 keV state in ^{19}Ne has a 100% branching to the 1508 keV state and the 4033 keV state in ^{19}F also has a 100% branching ratio to the 1459 keV state. This is consistent with the 4144 having a spin of $(9/2)^-$. Thus while the lifetimes and reduced transition strengths suggest a swapping of the spins of the 4144 keV state and 4200 keV state in ^{19}Ne, the branching ratios do not support the swapping. It is therefore very important to directly measure the spins of the 4144 keV and 4200 keV states in ^{19}Ne to settle the suggestion of interchanging the spins.

The above conjectures for the spins have been proposed by looking at the available data under the assumption that isospin symmetry is not violated. A direct spin measurement of the 4144 keV and 4200 keV levels in ^{19}Ne is necessary to test the conjectures proposed here.

Chapter 7

Summary

Seven states in ^{19}Ne above the α threshold were populated in the ^{3}He(^{20}Ne, α)^{19}Ne reaction at a beam energy of 34 MeV using a ^{3}He implanted Au foil. The lifetimes of these states are of astrophysical importance as inputs to the ^{15}O$(\alpha,\gamma)^{19}$Ne reaction rate calculation.

The Doppler shifted γ rays from the decays of states in ^{19}Ne were analyzed to determine their lifetimes. The data were fitted simultaneously with backgrounds and line shapes corresponding to different lifetimes. The line shapes were calculated after correcting for density variations due the ^{3}He implantation in the Au target foil and accounting for the response of the Ge detector used to detect the γ rays.

Two branches of the astrophysically important state at 4035 keV were observed in the experiment and the branches yielded consistent lifetimes. Two branches of the 4548 keV state in ^{19}Ne were also observed and yielded consistent lifetimes.

The lifetime for the 4035 keV state is the most precise measurement so far and agrees with the other two reported values. The lifetimes of two other states in ^{19}Ne above the α threshold are also the most precise values to date. The lifetimes for the two of the three states of primary astrophysical interest - the 4035 keV and the 4602 keV states are now known with great precision. The lifetime calculated by combining the two branches of the 4548 keV level is also the most precise measurement for this state.

Two states in ^{19}Ne, the 4144 keV state and the 4200 keV state had transitions in the 2500 - 3000 keV range. The lifetimes of these two states in ^{19}Ne had large errors due to high backgrounds. Our measurements agreed with the previous measurements of these levels.

The ^{15}O$(\alpha,\gamma)^{19}$Ne reaction triggers the first breakout from the HCNO cycle into the *rp* process. In particular the 4035 keV level in ^{19}Ne dominates the reaction rate at temperatures ranging between 0.2 to 0.6 GK, where the trigger ocurs. The calculation of the ^{15}O$(\alpha,\gamma)^{19}$Ne reaction rate needs a precise measurement of both the τ and the B_α values of all the states in ^{19}Ne that contribute to the reaction. The precise measurement done here for the τ of the 4.035 MeV state in ^{19}Ne, a state that contributes dominantly to the

ignition of X-ray bursts has significant implications on the rate calculations of the $^{15}O(\alpha,\gamma)^{19}Ne$ reaction in stellar environments. However since there are only upper limits available for the B_α of the 4035 keV state, the reaction rate can also be calculated only as an upper limit.

It was found that the 4378 keV state could play a large role in the rate of the $^{15}O(\alpha,\gamma)^{19}Ne$ reaction above 0.6 GK along with the 4602 keV state. Our knowledge of the reaction rate is severely limited by the lack of a B_α value for the 4378 keV state.

A 90% CL upper limit on the reaction rate was calculated by using the parameters (either τ and B_α or Γ_γ and B_α) of six resonances. The 4035 keV state contributes dominantly at low temperatures, i.e, for T <0.5 GK. The $^{15}O(\alpha,\gamma)^{19}Ne$ reaction does not have a significant rate at temperatures below 0.4 GK. Since novae peak at about 0.2 - 0.3 GK, the resonant α capture by ^{15}O does not contribute to the nova scenarios.

The aim of this experiment was to measure the lifetimes of the states in ^{19}Ne above the α threshold. The experiment was very successful since it has yielded the most precise values of the lifetimes of three states in ^{19}Ne, including the two states that contribute dominantly to the $^{15}O(\alpha,\gamma)^{19}Ne$ breakout reaction in X-ray binaries.

The lifetimes of states of astrophysical interest above the α threshold are now known with sufficient precision. Although the knowledge of the B_α of the 4035 keV and the 4378 keV levels would enable a precise calculation of the reaction rate, the Monte Carlo simulations done here for the 90% CL upper limit exhibit a very interesting result. At temperatures above 0.8 GK when several states in ^{19}Ne make significant contributions to the reaction rate, the 90% CL upper limit on the sum of the rates from the resonances is significantly lower than the sum of the 90% CL upper limits on the rates of the individual contributing resonances. This implies that the rate of the $^{15}O(\alpha,\gamma)^{19}Ne$ reaction is probably lower than is currently reported.

The 4378 keV state starts contributing beyond temperatures of 0.6 GK. The lifetime of the 4378 keV state can be measured in future experiments. At higher beam energies, the Doppler shift would be larger and may enable a more precise measurement of this lifetime if the beam intensities were also greater.

To sharpen the astrophysical focus, one should also study the decay properties of the states at 4712 keV and 5092 keV. Currently there is no experimental measurement of the γ transitions from these states and the reaction rate calculations rely on the properties of the analog states of ^{19}F. If the transitions from the 4712 keV and the 5092 keV states are known, one may be able to apply the DSAM to measure the lifetimes of these states.

Bibliography

[1] T. K. Alexander, G. C. Ball, W. G. Davies, J. S. Forster, I. V. Mitchell, and H.-B. Mak. Lifetime measurements of levels in ^{26}Si and the ratio of neutron to proton transition amplitudes for mirror nuclei. *Physics Letters B*, 113:132, 1982.

[2] T. K. Alexander, G. C. Ball, W. G. Davies, and I. V. Mitchell. A measurement of the local density of ^{3}He-implanted metal foils. *Journal of Nuclear Materials*, 96:51, 1981.

[3] G. Audi, A. H. Wapstra, and C. Thibault. The Ame2003 atomic mass evaluation (II). Tables, graphs and references. *Nuclear Physics A*, 729:337, 2003.

[4] J. Audouze, J. W. Truran, and B. A. Zimmerman. Hot CNO-Ne Cycle Hydrogen Burning. Thermonuclear Evolution at Constant Temperature and Density. *Astrophysics Journal*, 184:493, 1973.

[5] G. C. Ball, T. K. Alexander, W. G. Davies, J. S. Forster, I. V. Mitchell, J. Keinonen, and H. B. Mak. Lifetimes of low-lying levels in ^{18}F. *Nuclear Physics A*, 386:333, 1982.

[6] H. A. Bethe. Energy Production in Stars. *Physical Review*, 55:434, 1939.

[7] J. C. Blackmon, D. W. Bardayan, W. Bradfield-Smith, A. E. Champagne, A. A. Chen, T. Davinson, K. I. Hahn, R. L. Kozub, Z. Ma, P. D. Parker, G. Rajbaidya, R. C. Runkle, C. M. Rowland, A. C. Shotter, M. S. Smith, K. B. Swartz, D. W. Visser, and P. J. Woods. Determination of the $^{14}O(\alpha,p)^{17}F_{g.s.}$ reaction rate by measurement of the $^{1}H(^{17}F,\alpha)^{14}$O cross section. *Nuclear Physics A*, 688:142, 2001.

[8] E. Bohm-Vitense. *Stellar Astrophysics*, volume 3. Cambridge University Press, 1992.

[9] B. A. Brown, B. H. Wildenthal, W. Chung, S. E. Massen, M. Bernas, A. M. Bernstein, R. Miskimen, V. R. Brown, and V. A. Madsen. Isovector E2 matrix elements from electromagnetic transitions in the s-d shell: Experiment and shell-model calculations. *Physical Review C*, 26:2247, 1982.

[10] E. M. Burbidge, G. R. Burbidge, W. A. Fowler, and F. Hoyle. Synthesis of the Elements in Stars. *Reviews of Modern Physics*, 29:547, 1957.

[11] Caughlan and Fowler. Nuclear reaction-Lifetimes and equilibrium abundances in the fast CN cycle. *Nature*, 238:23, 1972.

[12] G. R. Caughlan and W. A. Fowler. The Mean Lifetimes of Carbon, Nitrogen, and Oxygen Nuclei in the CNO Bicycle. *Astrophysics Journal*, 136:453, 1962.

[13] A. E. Champagne and M. Wiescher. Explosive hydrogen burning. *Annual Review of Nuclear and Particle Science*, 42:39, 1992.

[14] B. Davids, A. M. van den Berg, P. Dendooven, F. Fleurot, M. Hunyadi, M. A. de Huu, K. E. Rehm, R. E. Segel, R. H. Siemssen, H. W. Wilschut, H. J. Wörtche, and A. H. Wuosmaa. α-decay branching ratios of near-threshold states in ^{19}Ne and the astrophysical rate of ^{15}O(α,γ)^{19}Ne. *Physical Review C*, 67(1):012801, 2003.

[15] B. Davids, A. M. van den Berg, P. Dendooven, F. Fleurot, M. Hunyadi, M. A. de Huu, R. H. Siemssen, H. W. Wilschut, H. J. Wörtche, M. Hernanz, J. José, K. E. Rehm, A. H. Wuosmaa, and R. E. Segel. Astrophysical rate of ^{15}O(α,γ)^{19}Ne via the (p,t) reaction in inverse kinematics. *Physical Review C*, 67(6):065808, 2003.

[16] Barry Davids. Private communication, 2008.

[17] J. M. Davidson and M. L. Roush. Gamma decay in ^{19}Ne. *Nuclear Physics A*, 213:332, 1973.

[18] J. L. Fisker, J. Görres, M. Wiescher, and B. Davids. The Importance of ^{15}O(α,γ)^{19}Ne to X-Ray Bursts and Superbursts. *Astrophysics Journal*, 650:332, 2006.

[19] J. S. Forster, T. K. Alexander, G. C. Ball, W. G. Davies, I. V. Mitchell, and K. B. Winterbon. Lifetime measurements in ^{22}Ne, ^{28}Si and ^{31}P relevant to the interpretation of the Z_2 variation in low velocity DSAM results. *Nuclear Physics A*, 313:397, 1979.

[20] J. S. Forster, H. K. Ward, D. andAndrews, G. C. Ball, G. J. Costa, W. G. Davies, and I. V. Mitchell. Stopping powers measurements for ^{19}F, ^{24}Mg,^{27}Al,^{32}S and ^{35}Cl at energies 0.2 to 3.5 MeV/nucleon in Ti,Fe,Ni,Cu,Ag,and Au. *Nuclear Instruments and Methods*, 136:349, 1976.

[21] D. B. Fossan and E. K. Warburton. Lifetime measurements. *Nuclear spectroscopy and reactions*, 40C:307, 1974.

[22] W. A. Fowler. The quest for the origin of the elements. *Science*, 226:922, 1984.

[23] W. A. Fowler, G. R. Caughlan, and B. A. Zimmerman. Thermonuclear Reaction Rates, II. *Annual Review of astronomy and Astrophysics*, 13:69, 1975.

[24] J. D. Garrett, H. G. Bingham, H. T. Fortune, and R. Middleton. Study of the Reactions ^{16}O(^{6}Li,^{3}He)^{19}F and ^{16}O(^{6}Li,t)^{19}Ne at E(^{6}Li) =24 MeV. *Physical Review C*, 5:682, 1972.

[25] Geant4 Collaboration, S. Agostinelli, J. Allison, K. Amako, J. Apostolakis, H. Araujo, P. Arce, M. Asai, D. Axen, S. Banerjee, G. Barrand, F. Behner, L. Bellagamba, J. Boudreau, L. Broglia, A. Brunengo, H. Burkhardt, S. Chauvie, J. Chuma, R. Chytracek, G. Cooperman, G. Cosmo, P. Degtyarenko, A. dell'Acqua, G. Depaola, D. Dietrich, R. Enami, A. Feliciello, C. Ferguson, H. Fesefeldt, G. Folger, F. Foppiano, A. Forti, S. Garelli, S. Giani, R. Giannitrapani, D. Gibin, J. J. Gómez Cadenas, I. González, G. Gracia Abril, G. Greeniaus, W. Greiner, V. Grichine, A. Grossheim, S. Guatelli, P. Gumplinger, R. Hamatsu, K. Hashimoto, H. Hasui, A. Heikkinen, A. Howard, V. Ivanchenko, A. Johnson, F. W. Jones, J. Kallenbach, N. Kanaya, M. Kawabata, Y. Kawabata, M. Kawaguti, S. Kelner, P. Kent, A. Kimura, T. Kodama, R. Kokoulin, M. Kossov, H. Kurashige, E. Lamanna, T. Lampén, V. Lara, V. Lefebure, F. Lei, M. Liendl, W. Lockman, F. Longo, S. Magni, M. Maire, E. Medernach, K. Minamimoto, P. Mora de Freitas, Y. Morita, K. Murakami, M. Nagamatu, R. Nartallo, P. Nieminen, T. Nishimura, K. Ohtsubo, M. Okamura, S. O'Neale, Y. Oohata, K. Paech, J. Perl, A. Pfeiffer, M. G. Pia, F. Ranjard, A. Rybin, S. Sadilov, E. di Salvo, G. Santin, T. Sasaki, N. Savvas, Y. Sawada, S. Scherer, S. Sei, V. Sirotenko, D. Smith, N. Starkov, H. Stoecker, J. Sulkimo, M. Takahata, S. Tanaka, E. Tcherniaev,

E. Safai Tehrani, M. Tropeano, P. Truscott, H. Uno, L. Urban, P. Urban, M. Verderi, A. Walkden, W. Wander, H. Weber, J. P. Wellisch, T. Wenaus, D. C. Williams, D. Wright, T. Yamada, H. Yoshida, and D. Zschiesche. Geant4-a simulation toolkit. *Nuclear Instruments and Methods in Physics Research A*, 506:250, 2003.

[26] G. Hackman, S. M. Austin, T. Glasmacher, T. Aumann, B. A. Brown, R. W. Ibbotson, K. Miller, B. Pritychenko, L. A. Riley, B. Roeder, and E. Spears. Intermediate-energy Coulomb excitation of ^{19}Ne. *Physical Review C*, 61(5):052801, 2000.

[27] K. I. Hahn, A. García, E. G. Adelberger, P. V. Magnus, A. D. Bacher, N. Bateman, G. P. Berg, J. C. Blackmon, A. E. Champagne, B. Davis, A. J. Howard, J. Liu, B. Lund, Z. Q. Mao, D. M. Markoff, P. D. Parker, M. S. Smith, E. J. Stephenson, K. B. Swartz, S. Utku, R. B. Vogelaar, and K. Yildiz. Structure of ^{18}Ne and the breakout from the hot CNO cycle. *Physical Review C*, 54:1999, 1996.

[28] B. Harss, J. P. Greene, D. Henderson, R. V. Janssens, C. L. Jiang, J. Nolen, R. C. Pardo, K. E. Rehm, J. P. Schiffer, R. H. Siemssen, A. A. Sonzogni, J. Uusitalo, I. Wiedenhöver, M. Paul, T. F. Wang, F. Borasi, R. E. Segel, J. C. Blackmon, M. S. Smith, A. Chen, and P. Parker. Stellar Reactions with Short-Lived Nuclei: ^{17}F(p,α)^{14}O. *Physical Review Letters*, 82:3964, 1999.

[29] B. Harss, C. L. Jiang, K. E. Rehm, J. P. Schiffer, J. Caggiano, P. Collon, J. P. Greene, D. Henderson, A. Heinz, R. V. Janssens, J. Nolen, R. C. Pardo, T. Pennington, R. H. Siemssen, A. A. Sonzogni, J. Uusitalo, I. Wiedenhöver, M. Paul, T. F. Wang, F. Borasi, R. E. Segel, J. C. Blackmon, M. Smith, A. Chen, and P. Parker. Widths of astrophysically important resonances in ^{18}Ne. *Physical Review C*, 65(3):035803, 2002.

[30] P. H. Hauschildt, S. Starrfield, S. N. Shore, F. Allard, and E. Baron. The Physics of Early Nova Spectra. *Astrophysics Journal*, 447:829, 1995.

[31] http://www.srim.org/SRIM/SRIMPICS/STOPHE/STOPHE79.gif, 2003.

[32] R. Kanungo, T. K. Alexander, A. N. Andreyev, G. C. Ball, R. S. Chakrawarthy, M. Chicoine, R. Churchman, B. Davids, J. S. Forster, S. Gujrathi, G. Hackman, D. Howell, J. R. Leslie, A. C. Morton,

S. Mythili, C. J. Pearson, J. J. Ressler, C. Ruiz, H. Savajols, M. A. Schumaker, I. Tanihata, P. Walden, and S. Yen. Lifetime of $^{19}Ne^{*}$(4.03 MeV). *Physical Review C*, 74(4):045803, 2006.

[33] J. Keinonen, H.-B. Mak, T. K. Alexander, G. C. Ball, W. G. Davies, J. S. Forster, and I. V. Mitchell. Lifetime of the 1.04 MeV state in ^{18}F, measured through the inverse reaction ^{3}He(^{16}O,p)^{18}F. *Physical Review C*, 23:2073, 1981.

[34] K.-L. Kratz, J.-P. Bitouzet, F.-K. Thielemann, P. Moeller, and B. Pfeiffer. Isotopic r-process abundances and nuclear structure far from stability - Implications for the r-process mechanism. *Astrophysics Journal*, 403:216, 1993.

[35] A. M. Laird, S. Cherubini, A. N. Ostrowski, M. Aliotta, T. Davinson, A. di Pietro, P. Figuera, W. Galster, J. S. Graulich, D. Groombridge, J. Hinnefeld, M. Lattuada, P. Leleux, L. Michel, A. Musumarra, A. Ninane, M. G. Pellegriti, A. C. Shotter, C. Spitaleri, A. Tumino, J. Vervier, and P. Woods. Indirect study of the astrophysically important ^{15}O(α,γ)^{19}Ne reaction through ^{2}H(^{18}Ne,^{19}Ne)^{1}H. *Physical Review C*, 66(4):048801, 2002.

[36] K. Langanke, M. Wiescher, W. A. Fowler, and J. Gorres. A new estimate of the Ne-19(p, gamma) Na-20 and O-15(alpha, gamma) Ne-19 reaction rates at stellar energies. *Astrophysics Journal*, 301:629, 1986.

[37] P. V. Magnus, M. S. Smith, A. J. Howard, P. D. Parker, and A. E. Champagne. *Nucl. Phys.*, A506:332, 1990.

[38] J. B. Marion and F. C. Young. *Nuclear Reaction Analysis- Graphs and Tables*. North Holland Publishing Company, Amsterdam, 1968.

[39] G. J. Mathews and F. S. Dietrich. The N-13(p, gamma)O-14 thermonuclear reaction rate and the hot CNO cycle. *Astrophysical Journal*, 287:969, 1984.

[40] R. Morlock, R. Kunz, A. Mayer, M. Jaeger, A. Müller, J. W. Hammer, P. Mohr, H. Oberhummer, G. Staudt, and V. Kölle. Halo Properties of the First $1/2^{+}$ State in ^{17}F from the ^{16}O(p,γ)^{17}F Reaction. *Physical Review Letters*, 79:3837, 1997.

[41] D. Prialnik and A. Kovetz. An extended grid of multicycle nova evolution models. *Astrophysics Journal*, 445:789, 1995.

[42] D. C. Radford. Background subtraction from in-beam HPGe coincidence data sets. *Nuclear Instruments and Methods in Physics Research A*, 361:306, 1995.

[43] D. C. Radford. ESCL8R and LEVIT8R: Software for interactive graphical analysis of HPGe coincidence data sets. *Nuclear Instruments and Methods in Physics Research A*, 361:297, 1995.

[44] T. Rauscher, F.-K. Thielemann, and K.-L. Kratz. Nuclear level density and the determination of thermonuclear rates for astrophysics. *Physical Review C*, 56:1613, 1997.

[45] K. E. Rehm, A. H. Wuosmaa, C. L. Jiang, J. Caggiano, J. P. Greene, A. Heinz, D. Henderson, R. V. Janssens, E. F. Moore, G. Mukherjee, R. C. Pardo, T. Pennington, J. P. Schiffer, R. H. Siemssen, M. Paul, L. Jisonna, and R. E. Segel. Branching ratio $\Gamma_\alpha/\Gamma_{total}$ of the 4.033 MeV $3/2^+$ state in ^{19}Ne. *Physical Review C*, 67(6):065809, 2003.

[46] C. E. Rolfs. *Nuclear Physics A*, 217:29, 1973.

[47] C. E. Rolfs and W. S Rodney. *Cauldrons in the Cosmos*. University of Chicago Press, 1988.

[48] R. P. Sharma. Inelastic scattering of deuterons from ^{197}Au. *Nuclear Physics A*, 154:312, 1970.

[49] M. S. Smith and K. E Rehm. Nuclear Astrophysics measurements with radioactive beams. *Annual Review of Nuclear and Particle Science*, 51:91, 2001.

[50] R. G. Stokstad, I. A. Fraser, J. S. Greenberg, S. H. Sie, and B. D. A. Doppler shift attenuation studies in heavy nuclei. *Nuclear Physics A*, 156:145, 1970.

[51] R. E. Taam. Nuclear processes at neutron star surfaces. *Annual Review of Nuclear and Particle Science*, 35:1, 1985.

[52] W. P. Tan, J. L. Fisker, J. Görres, M. Couder, and M. Wiescher. O15(α,γ)Ne19 Breakout Reaction and Impact on X-Ray Bursts. *Physical Review Letters*, 98(24):242503, 2007.

[53] W. P. Tan, J. Görres, J. Daly, M. Couder, A. Couture, H. Y. Lee, E. Stech, E. Strandberg, C. Ugalde, and M. Wiescher. Lifetime of the astrophysically important 4.03-MeV state in ^{19}Ne. *Physical Review C*, 72(4):041302, 2005.

[54] D. R. Tilley, H. R. Weller, C. M. Cheves, and R. M. Chasteler. Energy levels of light nuclei A = 18-19. *Nuclear Physics A*, 595:1, 1995.

[55] D. W. Visser, J. A. Caggiano, R. Lewis, W. B. Handler, A. Parikh, and P. D. Parker. Particle decay branching ratios for states of astrophysical importance in ^{19}Ne. *Physical Review C*, 69(4):048801, 2004.

[56] R. K. Wallace and S. E. Woosley. *Astrophys. J. Suppl. Ser.*, 45:389, 1981.

[57] G. Wallerstein, I. J. Iben, P. Parker, A. M. Boesgaard, G. M. Hale, A. E. Champagne, C. A. Barnes, F. Käppeler, V. V. Smith, R. D. Hoffman, F. X. Timmes, C. Sneden, R. N. Boyd, B. S. Meyer, and D. L. Lambert. Synthesis of the elements in stars: forty years of progress. *Reviews of Modern Physics*, 69:995, 1997.

[58] E. K. Warburton, J. W. Olness, and C. J. Lister. Lifetimes of the ^{21}Ne 2796-, 1747-, and 2867-keV levels. *Physical Review C*, 20:619, 1979.

[59] E. K. Warburton, J. W. Olness, and A. R. Poletti. Nuclear Structure of Na^{22}.I. Gamma-Ray Correlations and Lifetime Measurements for Levels of E_{ex}<3.1 MeV. *Physical Review*, 160:938, 1967.

[60] E.-K. Warburton and J. Weneser. *Isospin in Nuclear Physics*, 1969.

[61] M. Wiescher, J. Görres, and H. Schatz. *J. Phys. G*, 25:R133, 1999.

[62] M. Wiescher, J. Gorres, and F.-K. Thielemann. F-17(p, gamma)Ne-18 in explosive hydrogen burning. *Astrophysical Journal*, 326:384, 1988.

[63] M. Wiescher, V. Harms, J. Gorres, F.-K. Thielemann, and L. J. Rybarcyk. Alpha-burning of O-14. *Astrophysical Journalj*, 316:162, 1987.

[64] Samuel S. M. Wong. *Introductory Nuclear Physics*. Prentice-Hall, Englewood Cliffs, New Jersey, 1990.

[65] H. Xiaolong and Z. Chunmei. *Nuclear Data Sheets*, 104:283, 2005.

[66] J. F. Ziegler. SRIM-2003. *Nuclear Instruments and Methods in Physics Research B*, 219:1027, 2004.

Appendix A

Target Heating

A 12.5 μm thick Au foil implanted with ^{3}He ions was used in the experiment. The foil was 1cm×1cm. The foil was sandwiched between two target frames that had circular apertures of radii 0.5 cm. The foil thus presents a circular cross section to the beam, as shown In Fig. A.1. The beam spot was < 2 mm in diameter. When the beam hits the target, the temperature of the target rises; the bulk of the heat is conducted away radially. The 5 mm radius of the foil (OA) and the maximum radius of the beam spot, OB (1 mm) is shown in Fig. A.1. Let the beam spot radius be denoted by the symbol a, the radius of the implanted region of the foil by b and the thickness of the target by t.

Let the power deposited on the foil due to the beam be P. If the thermal conductivity of the foil is denoted as κ, the rise in temperature ΔT over an area A is

$$\Delta T = \frac{PL}{\kappa A} \tag{A.1}$$

Here L represents the length of the foil across which the heat gets dissipated. Since the heat is dissipated radially, and the area A across which the beam power is transferred is 2πrt, we can rewrite the above equation as

$$dT = \frac{Pdr}{\kappa 2\pi rt} \tag{A.2}$$

Integrating Eq. A.2 we get a measure of how much temperature rise occurs in the foil as the heat is dissipated radially.

$$\Delta T = \frac{P}{2\pi t\kappa}\int_{r_1}^{r_2}\frac{1}{r}\,dr \;= \frac{P}{2\pi t\kappa} ln\frac{r_2}{r_1} \tag{A.3}$$

Since the values of the limits r_1 and r_2 are well defined as a and b resp ectively, the temperature rise for a given beam power can be calculated for different foils of various thickness.

$$\Delta T = \frac{P}{2\pi t\kappa} ln\frac{b}{a} \tag{A.4}$$

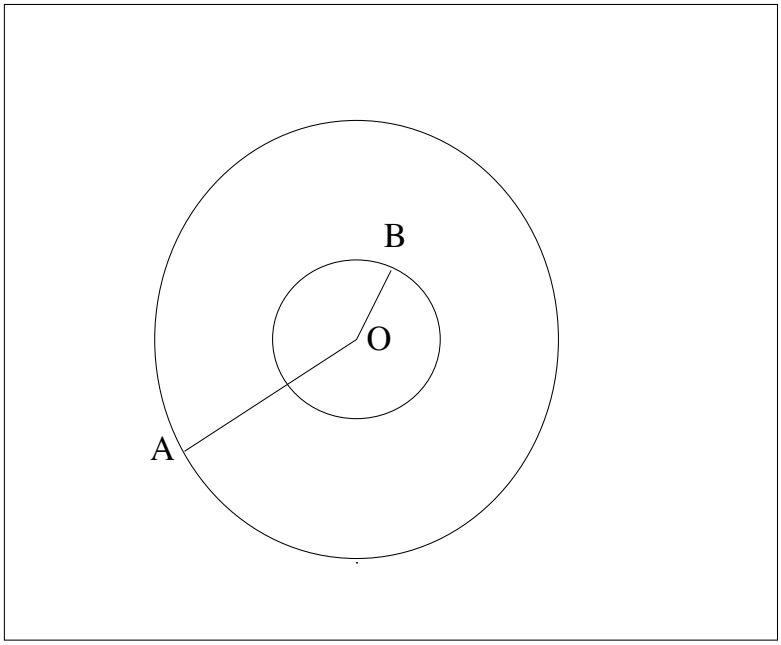

Figure A.1: The maximum beam spot radius OB and the radius of the implanted region OA are shown. The bulk of the heat is conducted radially across the foil. The figure is not to scale.

Beam Power Watt	Foil Material	Thermal conductivity $\frac{Watt}{meterKelvin}$	Temeperature rise ΔT (Kelvin)
0.5	Au	317	22.5
1.0	Au	317	45
1.5	Au	317	67.5
0.5	Al	237	30

Table A.1: Temperature rise in different foils for varying beam power. The foils are assumed to be 15 μm thick. The beam spot was assumed to be 2 mm and the radius of the foil was assumed to be 5 mm.

The rise in temperatures for different beam powers on different foils of 12.5 μm thickness is shown in Table A.1. From Table A.1 it is clear that for a given beam power, the rise in temperature is lower for the Au foil since it dissipates the incident heat more effectively than the Al foil. It is also clear that the target has to be cooled to at least below - 30°C if a beam power of 1 Watt is put on the Au target such that the temperature does not rise above the room temperature and the ^{3}He ions do not diffuse out of the Au foil.

Appendix B

Platinum Wire Calibration

.

A Resistance Temperature Detector (RTD) made of platinum was used to record the temperatures in the experiment. For this purpose a 36" long wire was mounted inside the scattering chamber. One end of the wire was attached to a pin on the bottom flange of the scattering chamber to facilitate the measurement of its resistance. The other end of the wire was in contact with the target ladder through small contact pins.

The temperature of the wire was calibrated against its resistance. The resistance of the wire was measured during the experiment with a multimeter. The multimeter provides a potential difference between the two ends of the wire, measures the resulting current and then calculates the resistance. The temperature of the wire was read off the calibration chart of temperature *vs.* resistance. Since the wire was in contact with the target ladder, the wire was at the same temperature as the target ladder. The RTD was thus used to monitor the temperature of the target ladder.

Appendix C

Target Cooling

It was essential to cool the target. The following calculations estimate the maximum cooling due to the additional Cu brackets.

The copper shroud in the new scattering chamber was attached to the liquid nitrogen dewar by a cold finger. The shroud was 27.5 cm long, had an inner diameter of 1.9 cm and an outer diameter of 2.7 cm. At the point where the shroud was in contact with the liquid nitrogen dewar, we assume the temperature was 77 K. Since the shroud was made of copper, the conductive transfer of heat would dominate over the radiative mechanism. The temperature of the shroud at the end farthest from the cold finger was measured to be 169 K. Assuming a 100% conductive transfer of energy, the rate of transfer of the heat energy $\frac{dW}{dt}$ can be written as

$$\frac{dW}{dt} = \kappa A \frac{\Delta T}{d} \tag{C.1}$$

Here A is the area across which the heat transfer occurs, κ is the thermal conductivity of copper (401 Watt/meter Kelvin), ΔT is the temperature difference between the ends and d is the material thickness. Since all the quantities on the right side of the equation are known, the transfer rate of the heat can be calculated. For our case, this was calculated to be $\sim$39 Watt.

The copper shroud has two copper brackets attached to the side which make contact with the copper target ladder to cool the target. The dimensions of each of the additional copper brackets was 3.8 cm$\times$1.4 cm$\times$0.2 cm. The cooling occurs from the end of the shroud via the copper brackets of area 3.8$\times$0.2 cm^2. The distance across which the heat transfer occurs is the width of the copper brackets - 1.4 cm. Assuming a 100% efficiency for conductive cooling, Eq. C.1 can be applied. Since the transfer rate of the heat is known, we can calculate the temperature difference between the target and the end of the shroud at 169 K.

$$\Delta T = \frac{dW/dt \times d}{A\kappa} \tag{C.2}$$

The temperature difference between the target and the end of the shroud is ∼17 K because of the additional area of contact with the copper brackets. This implies that the ambient temperature at the target ladder is ∼-87°C. The calculations are not corrected for radiation. The temperature of the target is expected to be above -87°C. Fortunately Cu is an excellent conductor of heat and the radiation losses are expected to be small. When the actual measurements were done, we observed a temperature of -70°C with no beam on the target.

Appendix D

Intrinsic Response

The intrinsic width of γ lines is much smaller than the resolution of a HPGe detector. However, in an experiment, the line shape is well described by a skewed Gaussian. The skewness of the line shape is due to the incomplete charge collection that is caused by impurities and minute damage in the crystal. The line shape of the γ ray is well described by a function

$$y \propto e^{\frac{x-c}{\beta}} \times erf(\frac{x-c}{\sqrt{2}\sigma} + \frac{\sigma}{\sqrt{2}\beta}) \tag{D.1}$$

where
x = E_γ, the energy of the γ ray,
y = the amplitude,
c = the centroid of the Gaussian,
β = the skewness of the Gaussian and
σ = the standard deviation of the Gaussian component.

Four lines of ^{56}Co were fit with the functional form given above using RADWARE [42, 43]. This nucleus has several strong lines above 2 MeV. The highest γ energy observed from ^{56}Co with sufficient statistics was 3.253 MeV. The best fit parameters β and σ were extracted and are tabulated in Table D.1.

In Fig. D.1, the values of β and σ for four γ rays from ^{56}Co are plotted. The top panel (a) shows the variation of the β parameter and the lower panel (b) shows the variation of the σ values. The RADWARE parameters are shown by blue circles. The energy dependence of the parameters was characterized by a line, as shown. The slopes and the intercepts for the fit are shown in Table D.2. The values of β and σ were extrapolated to the energies of interest using the empirical linear relation.

Table D.2 shows the central and 1σ values for the slope and intercept that fit β and σ in Fig. D.1. The β and σ values needed to calculate the intrinsic line shape for the γ energies of interest were extrapolated using the values tabulated in Table D.2.

E $_\gamma(keV)$	β	σ
1770	0.976	2.167
2036	1.22	2.46
2597	1.58	2.84
3253	2.33	3.47

Table D.1: The best fit parameters β and σ yielded by the χ^2 minimization of the RADWARE fits.

Radware Parameter	Slope	Intercept (keV)
β	0.0008915±0.00008	-0.62537±0.199
σ	0.0008539±0.000046	0.67312±0.116

Table D.2: The slope and intercept values for the energy dependence of β and σ.

Fig. D.2 shows the data from the ^{56}Co line at 3253 keV. A Gaussian fit to these data is shown by the red dashed line. Also shown is a RADWARE fit to the data - the solid green line. The general approach to use a Gaussian response for the detector would overestimate the lifetime and is vastly improved by using a measured response for the line shape, as can be seen from Fig. D.2.

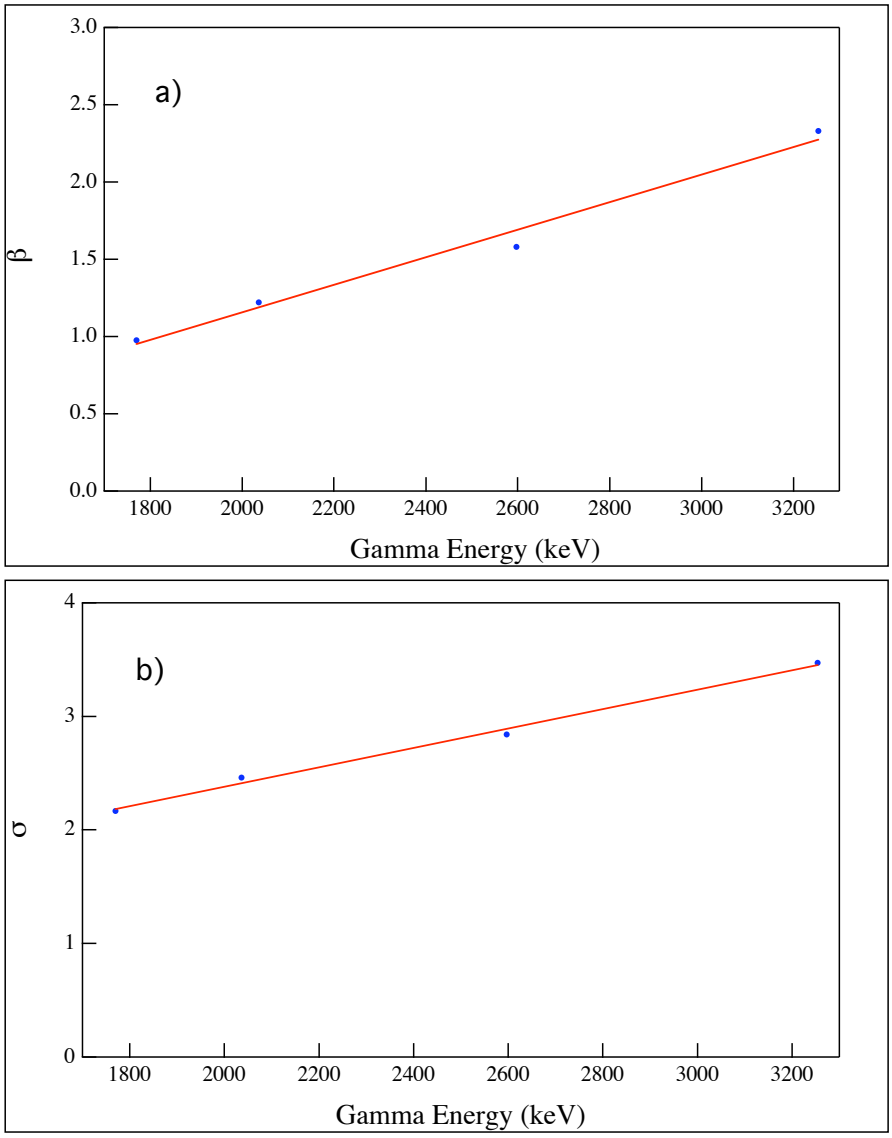

Figure D.1: The variation of the fit parameters β and σ with energy.

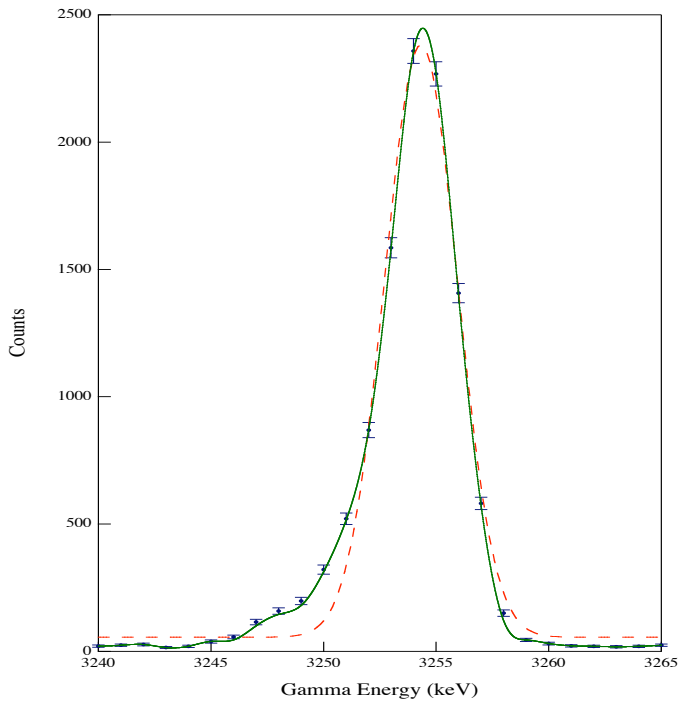

Figure D.2: The γ energy spectrum of the 3253 keV transition from the ^{56}Co source. Gaussian and skewed Gaussian fits are also shown by dashed red and solid green lines respectively.

Appendix E

Two Foil Approach

The implantation of the ^{3}He in a backing foil causes density variations in the foil. The implantation causes the backing foil to swell in the beam direction. The mass of the implanted region is also incremented by the amount of ^{3}He implanted.

Both these factors result in a larger thickness of the implanted region than is calculated from the dosage of 30 keV ^{3}He ions implanted in the backing foil. In our case the backing foil was 12.5 μm thick Au foil. The dosage of ^{3}He was 6×10^{17} cm^{-2}. The swelling in the Au foil due to this implant has been studied in an earlier experiment [2]. The prescription from this reference has been used to calculate the thickness of the first layer. The second layer is the Au foil alone.
There are three assumptions in the two foil approach.
1. The first layer is the ^{3}He implanted layer that swells after the ^{3}He ions have been implanted into the backing Au foil. The second layer is the pure Au foil.
2. The implanted layer is uniformly swollen and can be characterized in terms of a peak and a width for the ^{3}He distribution.[4]
3. All recoils originate at the peak of the ^{3}He distribution and pass through half the width before entering the pure Au foil region.[5]

From experimental measurements the peak atomic concentration of ^{3}He in the implanted Au foil (for a dosage of 6×10^{17} cm^{-2}) is 0.653. This implies for the ratio of the Au atoms to the ^{3}He atoms in the implanted layer is 1 : 0.653. From the same experiment, the factor A correlating the variation in volume to the concentration is 0.75 [2]. The factor A was one of the fitting parameters to explain the swelling effects in the Au foil due to the ^{3}He implantation of a given dosage. Thus in the implanted region, the density varies according to the stoichiometric ratio of ^{3}He and Au. To calculate the density variation, the mass increase due to the ^{3}He implantation has to be calculated. The mass of Au is 196.97 amu and for ^{3}He is 3.016 amu.

[4] The peak and width are discussed in Sec. 2.1.
[5] The errors associated with this assumption are included in the systematic errors.

Since the peak concentration of ^{3}He is 0.653, the mass added due to the implantation is 3.016 $\times$ 0.653 amu. The mass of the implanted layer is 198.94 amu.

The implantation increases the depth of the first layer by a factor of 0.49. Thus the density of the Au + ^{3}He layer is affected by the implantation in two ways.
1. It is decreased by a factor of 1.49 due to the swelling of the implanted layer.
2. It is increased by the extra mass of the ^{3}He in the implanted region.

Considering both effects, the density of the implanted layer changes from that of pure Au (19.28 g cm^{-3}) to

$$19.28 \times \frac{1}{(1 + 0.75 \times 0.653)} \frac{198.94}{196.97} = 13.07\ g\ cm^{-3} \tag{E.1}$$

The recoils originating at the peak of the ^{3}He distribution pass through half of the width of the distribution which is 0.072 μm. The swelling increases this by a factor of 0.49. The half width and the resulting thickness through which the recoils pass is 0.107 μm. Expressing the thickness of the swollen layer in mg cm^{-2} we get 0.139 mg cm^{-2}. The two foils due to the implantation are treated separately. The two layers are

- The swollen layer of thickness 0.107 μm and density 13.07 g cm^{-3}.
- The pure Au layer of thickness 12.4 μm and density 19.28 g cm^{-3}.

The energy losses of the recoils through two layers were calculated separately. The energy loss for the Au layer was taken from experimental measurements. Measurements of energy loss of ^{20}Ne through Au at several energies exist [19]. These results were interpolated using the prescription in Ref. [19] and the empirical energy loss of the recoiling ^{19}Ne in Au was used in the analysis of the line shape.

Appendix F

Monte Carlo Simulations

The geometry of the Ge detector strongly influences its detection efficiency as a function of angle. Besides the geometry, there are two other factors that influence the detector efficiency - its placement in the experiment and its photo peak efficiency for a given E_γ. The combination of these three factors gives rise to a detector efficiency function that has to be incorporated while analyzing line shapes and extracting lifetimes from the line shape. The calculations that follow were done to obtain physical insight and are for illustrative purposes. The results from the GEANT4 calculations [25] were input parameters for the line shape code.

The Ge crystal consists of a cylinder of length 5.91 cm (l) and diameter 8.16 cm (radius r = 4.08 cm). It also has a cylindrical core in the center for electrical outputs. The core is assumed to be 1 cm in diameter and 4.2 cm in length. The core is thus at a distance of 1.7 cm from the front of the detector.

The angular distribution for the emission of γ rays is an input for the simulation of the efficiency of the detector as function of angle. A Monte Carlo simulation was done by drawing several thousand γ rays of a fixed energy from a given distribution, tracing their path through the detector and calculating the efficiency of detecting the γ ray. In the preliminary calculations, an isotropic distribution was assumed. Since the angle of the γ rays was allowed to vary, they interact with differing volumes within the detector resulting in different path lengths x. The detection efficiency was calculated according to

$$\epsilon(\theta) = 1 - e^{-\mu_l x(\theta)} \tag{F.1}$$

where μ_l is the attenuation coefficient.

The experiment dealt with γ rays of $\sim$ 4 MeV and $\sim$ 2 MeV. μ_l for these γ rays were taken from Ref. [38]; μ_l of a 4 MeV and 2 MeV γ ray are $\sim$ 5×10^{-4} cm^{-1} and $\sim1\times10^{-3}$ cm^{-1} respectively.

To demonstrate the difference in the path lengths the detector volume is divided into three regions on the basis of the incident angle. Each region is symmetric about the detector axis. Only the positive angles will be discussed

since the negative angles can be treated in a similar fashion. The interaction (path) length of γ rays in the three regions is discussed below.

In Fig. F.1, the γ ray source is placed at O and the path of the gamma ray $\vec{OR}$ is shown by the solid arrow. The ray $\vec{OL}$ defines the beam axis. The distance of the source from the detector is denoted by d. The maximum allowed angle for the detector acceptance is shown as $\theta^{allowed}$ where

$$\theta^{allowed} = tan^{-1}\frac{r}{d} \tag{F.2}$$

However, due to the presence of the central core, the path length for the γ ray in the detector is largest at a critical angle θ_c, as can be seen in Fig. F.1.

Region 1: When the angle of incidence is between $\angle POB$ and $\angle POC$, the γ rays may interact with a large volume. This results in a large efficiency for detecting the photons that interact within this angular range. The path length of the gamma ray, emitted at an angle θ, is shown by QR in the figure. Here Q is the point at which the γ ray enters the detector.

Then

$$QR = OR - OQ \tag{F.3}$$

But

$$OR = \frac{OL}{cos\theta} \tag{F.4}$$

$$\Rightarrow OR = \frac{OP + Pl}{cos\theta} \tag{F.5}$$

$$\Rightarrow OR = \frac{(d + l)}{cos\theta} \tag{F.6}$$

Similarly,

$$OQ = \frac{d}{cos\theta} \tag{F.7}$$

and the path length is

$$QR = \frac{l}{cos\theta} \tag{F.8}$$

The critical value for θ is defined when the angle θ satisfies the equation

$$\theta = \theta_c = tan^{-1}(\frac{r}{d + l}) \tag{F.9}$$

Region 2 : The second region includes all angles of incidence between θ_c and the experimentally allowed maximum angle $\theta^{allowed}$. The path of the γ ray emitted from the target at an angle θ that is between θ_c and $\theta^{allowed}$ is denoted by $\vec{OF}$. The path length for the γ ray within the crystal is then EF

where E is the point at which the γ ray enters the crystal. Following the procedure above, the path length can be written as

$$EF = OF - OE \tag{F.10}$$

But

$$OF = \frac{r}{sin\theta} \tag{F.11}$$

and

$$OE = \frac{d}{cos\theta} \tag{F.12}$$

Thus the path length EF for a γ ray in the second region is

$$EF = \frac{r}{sin\theta} - \frac{d}{cos\theta} \tag{F.13}$$

Region 3: When the angle of incidence is between 0° and $\angle POB$: In this region, the γ ray interacts with a small volume of the detector.

This region includes the core and the curvature of the core has to be included in the calculations. Fig. F.2 is a zoomed in version of Fig. F.1. The effect of the core is discussed with reference to Fig. F.2. The target is placed at point O and ray $\vec{OB}$ traces the boundary between region 1 and 2, as discussed above. The face of the detector is not shown in full. The path length of the γ ray in region 3, RH, is needed to estimate the efficiency of detection of γ rays emitted close to the beam axis.

PS is the distance between the front of the detector (point P) and the beginning of the core (point S) and is called c. Point N defines the end point of the rounded core and M defines the intersection of the beam axis and the perpendicular dropped from point N on to the beam axis. Let SM be defined as c_r and the radius of the core NM be $r^{'}$.

Line segments HI and GK are parallel to NM. The line GK is a tangent to the core at point S. The path length of the γ ray, emitted at an angle θ, is RH where R is the point at which the γ ray enters the detector. This can be rewritten as

$$RH = OG - OR + GH \tag{F.14}$$

Each of the quantities on the right side of the equation can be related θ and other geometric constants.

$$OG = \frac{d + c}{cos\theta} \tag{F.15}$$

$$OR = \frac{d}{cos\theta} \tag{F.16}$$

and

$$GH = \frac{ST}{cos\theta} \tag{F.17}$$

The length ST depends on the geometry of the core as well as the angle of incidence. We parametrize the front boundary of the core with a parabolic function and apply the boundary conditions to express the path length in terms of the geometry of the detector, its placement and θ.

The parabolic function is

$$\frac{c_r(d+c+x)^2 tan^2\theta}{(r')^2} - x = 0 \tag{F.18}$$

The path length x is then defined for an angle of incidence θ by Eq. F.18.

The curvature at the edges of the detector and at the far end of the core were not considered in this simulation. The efficiency of the detectors for 4 MeV γ rays was calculated and is shown in Fig. F.3. The solid line shows the results of the simulation. A Gaussian with a centroid of 9.5°and a standard deviation of 5.6° can be used to describe the detector's response, as is shown by the dotted line in Fig. F.3. The centroid and standard deviation of the Gaussian were the input parameters to the DSAM code. Inclusion of the curvature of the detector and core edges would eliminate the discontinuities in Fig. F.3.

The simulation was also run assuming an anisotropic distribution for the γ rays. This was done by drawing the γ ray emission angle randomly from l=1 and l=2 distributions. There was no significant change with the inclusion of the l=1 and l=2 angular distributions.

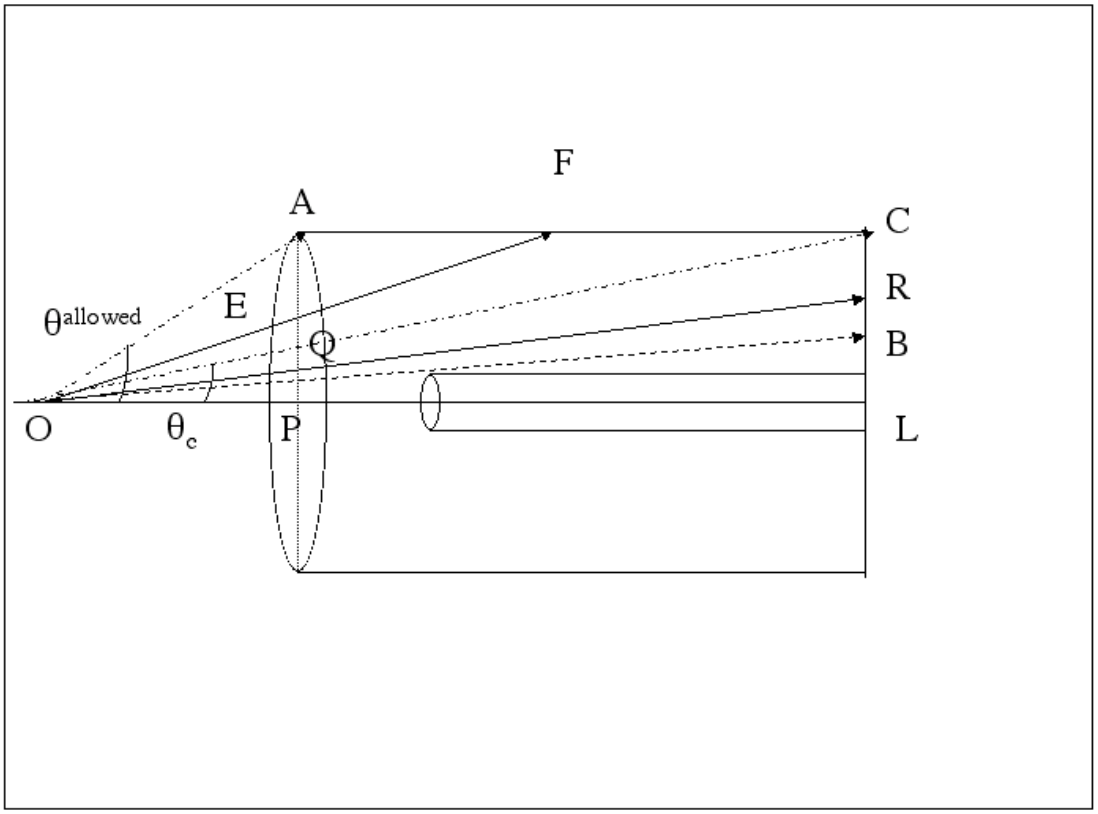

Figure F.1: The Ge detector and the various angles for the γ rays. The figure is not to scale.

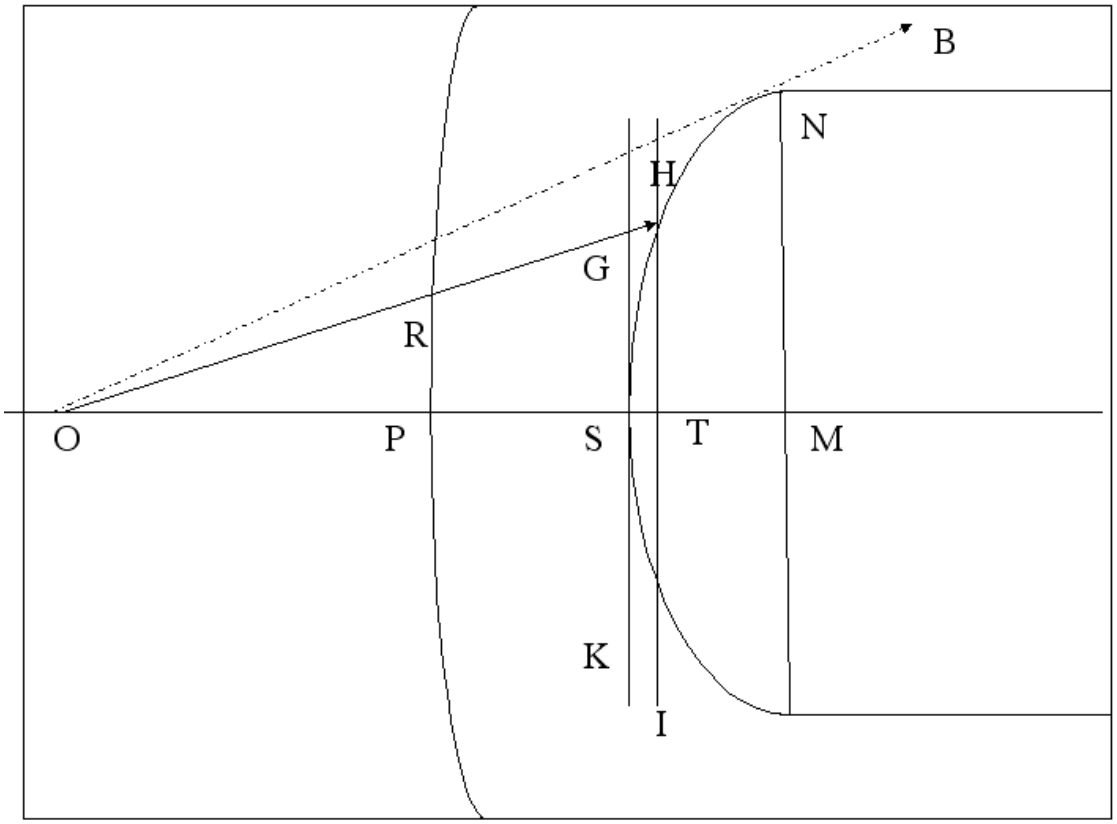

Figure F.2: The central core of the detector has been enlarged to illustrate the effect of the curvature and geometry on the detection of γ rays emitted close to the beam axis. The figure is not to scale.

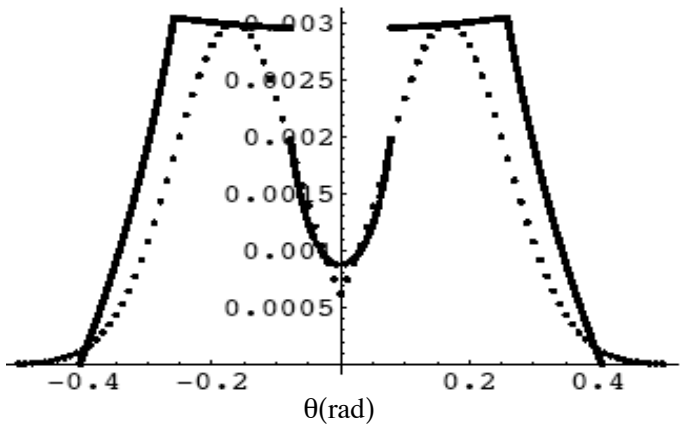

Figure F.3: The detection efficiency for a simplified detector geometry and an isotropic emission of γ rays of 4 MeV is shown by the solid line. The dotted line is a Gaussian fit with centroid and standard deviation of 9.5° and 5.6°.

Appendix G

Reduced Transition Strength

The partial width of a γ ray transition of energy E_γ is given by

$$\Gamma_\gamma = \frac{8\pi(\lambda+1)}{\lambda([2\lambda+1]!!)^2}(\frac{E_\gamma}{\hbar c})^{2\lambda+1}B(\lambda) \tag{G.1}$$

where λ is the multi polarity of the γ ray , $\hbar$ is Planck's constant h/2π, c is the speed of light and the reduced transition strength B(λ) is defined as [64]

$$B(\lambda) = \frac{1}{2I_i+1}| < I_f||O(\lambda)||I_i > |^2 \tag{G.2}$$

Here I_i stands for the angular momentum of the initial state and I_f that of the final state and $O(\lambda)$ stands for the electric/magnetic operator of multipolarity λ. For

$$\Gamma_\gamma \sim \Gamma = \frac{\hbar}{\tau} \tag{G.3}$$

the reduced transition strength varies inversely with the lifetime τ and the energy of the γ ray, i.e.,

$$B(\lambda) \propto \frac{1}{\tau E^{2\lambda+1}} \tag{G.4}$$

The constant of proportionality depends on the mass A of the nucleus, the type of the transitions (electric or magnetic) and on the multipolarity.

The B(λ)s are usually expressed in Weisskopf units B_W [64]. For an electric transition of multipolarity λ the Weisskopf unit is given by

$$B_W(E\lambda) = \frac{1}{4\pi}(\frac{3}{3+\lambda})^2(1.2A^{1/3})^{2\lambda}e^2 fm^{2\lambda} \tag{G.5}$$

where e is the charge of the proton.

Similarly for a magnetic transition of multi polarity λ the Weisskopf unit is given by

$$B_W(M\lambda) = \frac{10}{\pi}(\frac{3}{3+\lambda})^2(1.2A^{1/3})^{2\lambda-2}\mu_N^2 fm^{2\lambda-2} \tag{G.6}$$

where μ_N is the nuclear magneton.

Appendix H

My Contributions

Eight months before the experiment ran I performed the cooling tests after optimizing the geometry of the additional Cu plates and the distance between the shroud and the target ladder. The temperature of the target ladder cooled from a previous lowest temperature of -2°C to -70°C.

The beam line allotted to our experiment was used by another group two weeks before our experiment was scheduled to run. The earlier setup was dismounted so that we could mount the scattering chamber that was built for our experiment. We also had to ensure that the scattering chamber was aligned to the beam line. Since the new scattering chamber had several parts, the alignment was carried out in steps. Mr. Randy Churchman and I started with aligning the upstream chamber. This chamber couples to the spider. The differential pumping aperture of 1 cm, the collimators of diameter 3 and 4 mm were aligned to the beam line. The Al platform that held the Si detectors was finally aligned to the beam axis. We carefully aligned the Ge detector to the beam line. I also ensured that we had a vacuum pressure of 4×10^{-7} torr for the experiment.

Once the scattering chamber was aligned, I repeated the cooling tests to reproduce a lowest temperature of - 70°C. I discussed the logic for the electronics with Dr. Barry Davids and set up the different coincidences using a pulser. I then mounted the ΔE detector on the Al platform, placed the triple α source on the target ladder and calibrated the ADC channel that would register the events from the ΔE detector. I repeated this procedure by replacing the ΔE with the E detector and calibrating the E detector.

I cooled both the Ge detectors before calibrating the detectors. I used two sources for the calibration before the experiment - ^{60}Co and ^{88}Y. After the experiment was completed, I calibrated the Si and Ge detectors. In addition I calibrated the detector aligned at 0° with a ^{56}Co source as well.

I selected four lines from 1.7 MeV up to 3.25 MeV from the ^{56}Co spectrum and analyzed them using the RADWARE program. Details are in Appendix D.

Once the calibrations of the 2 Si detectors and the Ge detector were complete, I wrote a code in C++ to analyze the data. I worked closely with

Dr. Barry Davids and frequently discussed the results of my analysis and their implications with him.

When faced with the choice of the stopping power, I decided to use the experimental stopping power on the basis of Fig. 4.9 and the figure in Ref.[31]. The previous two publications that measured the lifetimes of the states in ^{19}Ne above the α threshold used the theoretical stopping powers from SRIM. However I found that the theoretical stopping powers for most heavy ions in the energy region of interest differed from the experimental numbers by 5-10% and so I chose the experimental numbers for the stopping power in my analysis.

The target foil was treated as two layers - the implanted region and then the pure Au foil layer. Although the implanted region was very thin, it affected the lifetimes considerably. I consulted Dr. Tom Alexander before working out the stopping powers for the two foil approach. The details of my calculations on the two foil approach can be found in Appendix E.

The detection efficiency of the Ge detector was worked out by GEANT4 calculations. I used a Monte Carlo method to understand the effect of the geometry of the Ge detector on the detection efficiency. I simulated the detection efficiency using a simple model of the geometry of the detector. I examined the influence of different solid angles subtended at the detector as well as the influence of anisotropic dipole and quadrupole angular distributions of the emitted γ ray. The details of the simulation are discussed in Appendix F.

I analyzed the several line shapes using the methods outlined in Chapter 4 and the results are presented in Chapter 5. Two branches of the 4035 keV and the 4548 keV levels were seen in this experiment. The second branches of the 4035 keV and the 4548 keV levels have not been recorded in the earlier experiments that measured the lifetimes of states in ^{19}Ne above 3.53 MeV. I located the second branch of the 4035 keV state and extracted its lifetime. The value for the lifetimes extracted from the second branches of the 4035 keV and the 4548 keV levels resulted in reducing the overall error on the lifetimes of these two states.

The second branch of the 4035 keV state decays to the 1536 keV state. This yields an unshifted γ ray of energy 2499 keV. In the γ spectrum, the region of 2500 - 3000 keV had a large background. Several transitions of interest were observed in this energy region - the second branch of the 4035 keV level decaying to the 1536 keV level, the 4144 keV level to the 1508 keV state, the 4200 keV state decaying to the 1508 keV state etc. The large background interfered with the extraction of precise lifetimes. To understand the origin of the large background, I worked out the kinematics of

the compound nucleus ^{23}Mg and calculated the Doppler shift due to the γ rays emitted from ^{23}Mg. Two transitions from ^{23}Mg were Doppler shifted to the 2500 - 3000 keV region and could cause the observed background. I identified the unshifted and the Doppler shifted transition of the 2795 keV level, as discussed in Sec. 5.3. I proved that the 4634 keV state in ^{19}Ne was populated in our experiment by comparing the two plots in Fig. 5.16 (Sec. 5.9).

I observed two γ rays at 547 keV and 583 keV that were of comparable strength to the 511 keV γ ray. The 547 keV and 583 keV γ rays were not seen in coincidence with α particles. I researched the possible sources that could lead to these two γ rays and found that the γ lines could be due to the Coulomb excitation of Au.

While considering the sources of systematic errors, I wanted to understand the dependence of the lifetimes on the beam energy. The effect of the beam energy on the lifetimes of states in ^{19}Ne above the α threshold has not been recorded earlier. The lifetimes are dependent on the kinematics of the reaction and hence on the beam energy. My studies showed that varying the beam energy within its errors leads to considerable changes in the lifetimes.

After extracting the lifetimes of several states in ^{19}Ne, I compared the lifetimes with the isobaric analog states in ^{19}F. I noticed an anomaly between the lifetimes of two states in ^{19} Ne (the 4144 keV and the 4200 keV states) and their isobaric analog states. Since the spins of the states in ^{19}Ne are not assigned definitively, I conjectured that the spins of the two ^{19}Ne states could be swapped. I calculated the reduced transition probabilities to check the discrepancy.

I performed the calculations in the Apps. A and C. I also did the fitting of the γ line shape with RADWARE and the linear extrapolation discussed in Appendix D.

Acting on Dr. Scott Oser's suggestion to simulate reaction rates with the Monte Carlo method, I worked out Poisson distributions for the 4035 keV and the 4378 keV states and simulated the reaction rates that are discussed in Sec. 6.1. The large difference at high temperatures between the sum of the 90% CL upper limit contributions from 6 resonances and the 90% CL upper limit of the sum of the 6 resonances was a surprising result of the simulations I performed.